Imaging the bone cell network with nanoscale synchrotron computed tomography

Alexandra Joita Pacureanu

To cite this version:

Alexandra Joita Pacureanu. Imaging the bone cell network with nanoscale synchrotron computed tomography. Other. INSA de Lyon, 2012. English. NNT : 2012ISAL0001 . tel-00778408

HAL Id: tel-00778408
https://theses.hal.science/tel-00778408

Submitted on 20 Jan 2013

N° d'ordre 2012ISAL0001 Année 2012

Thèse

Imaging the bone cell network with nanoscale synchrotron computed tomography

Présentée devant

L'Institut National des Sciences Appliquées de Lyon

Pour obtenir

Le grade de docteur

ÉCOLE DOCTORALE ELECTRONIQUE, ELECTROTECHNIQUE, AUTOMATIQUE

Par

Alexandra PACUREANU

Soutenue le 19 janvier 2012 devant la commission d'examen

Jury

P. Laugier	Directeur de recherche CNRS	UPMC Paris
M. Garreau	Professeur	Université de Rennes 1
J. Klein-Nulend	Professeur	Université d'Amsterdam
J.Y. Buffière	Professeur	INSA de Lyon
M. Ciuc	Maitre de Conférences	Université Politehnica Bucarest
C. Muller	Maitre de Conférences	INSA de Lyon
V. Buzuloiu	Professeur	Université Politehnica Bucarest
F. Peyrin	Directeur de recherche INSERM	INSA de Lyon

Laboratoire de recherche CREATIS

Imaging the bone cell network with nanoscale synchrotron computed tomography

Thesis manuscript

submitted to INSA de Lyon by Alexandra Pacureanu

Advisors

Françoise Peyrin

Vasile Buzuloiu

Chantal Muller

Research work conducted at CREATIS, Lyon & ESRF, Grenoble

Part A – Background

Part B – Contributions

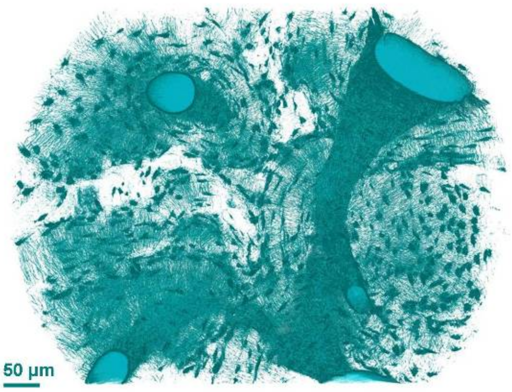

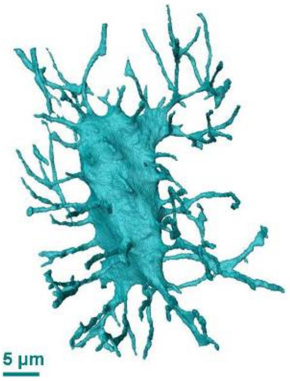

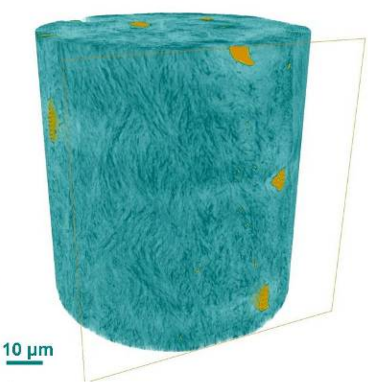

INSA Direction de la Recherche - Ecoles Doctorales – Quinquennal 2011-2015

SIGLE	ECOLE DOCTORALE	NOM ET COORDONNEES DU RESPONSABLE
CHIMIE	**CHIMIE DE LYON** **http://www.edchimie-lyon.fr** Insa : R. GOURDON	M. Jean Marc LANCELIN Université de Lyon – Collège Doctoral Bât ESCPE 43 bd du 11 novembre 1918 69622 VILLEURBANNE Cedex Tél : 04.72.43 13 95 directeur@edchimie-lyon.fr
E.E.A.	**ELECTRONIQUE, ELECTROTECHNIQUE, AUTOMATIQUE** **http://edeea.ec-lyon.fr** Secrétariat : M.C. HAVGOUDOUKIAN eea@ec-lyon.fr	M. Gérard SCORLETTI Ecole Centrale de Lyon 36 avenue Guy de Collongue 69134 ECULLY Tél : 04.72.18 60 97 Fax : 04 78 43 37 17 Gerard.scorletti@ec-lyon.fr
E2M2	**EVOLUTION, ECOSYSTEME, MICROBIOLOGIE, MODELISATION** **http://e2m2.universite-lyon.fr** Insa : H. CHARLES	Mme Gudrun BORNETTE CNRS UMR 5023 LEHNA Université Claude Bernard Lyon 1 Bât Forel 43 bd du 11 novembre 1918 69622 VILLEURBANNE Cédex Tél : 04.72.43.12.94 e2m2@biomserv.univ-lyon1.fr
EDISS	**INTERDISCIPLINAIRE SCIENCES-SANTE** **http://ww2.ibcp.fr/ediss** Sec : Safia AIT CHALAL Insa : M. LAGARDE	M. Didier REVEL Hôpital Louis Pradel Bâtiment Central 28 Avenue Doyen Lépine 69677 BRON Tél : 04.72.68 49 09 Fax :04 72 35 49 16 Didier.revel@creatis.uni-lyon1.fr
INFOMATHS	**INFORMATIQUE ET MATHEMATIQUES** http://infomaths.univ-lyon1.fr	M. Johannes KELLENDONK Université Claude Bernard Lyon 1 LIRIS - INFOMATHS Bâtiment Nautibus 43 bd du 11 novembre 1918 69622 VILLEURBANNE Cedex Tél : 04.72. 43.19.05 Fax 04 72 43 13 10 infomaths@bat710.univ-lyon1.fr
Matériaux	**MATERIAUX DE LYON**	M. Jean-Yves BUFFIERE Secrétaire : Mériem LABOUNE INSA de Lyon École Doctorale Matériaux Mériem LABOUNE Bâtiment Antoine de Saint-Exupéry 25bis Avenue Jean Capelle 69621 VILLEURBANNE Tel : 04 72 43 71 70 Fax : 04 72 43 72 37 ed.materiaux@insa-lyon.fr
MEGA	**MECANIQUE, ENERGETIQUE, GENIE CIVIL, ACOUSTIQUE (ED n°162)**	M. Philippe BOISSE Secrétaire : Mériem LABOUNE INSA de Lyon École Doctorale MEGA Mériem LABOUNE Bâtiment Antoine de Saint-Exupéry 25bis Avenue Jean Capelle 69621 VILLEURBANNE Tel : 04 72 43 71 70 Fax : 04 72 43 72 37 mega@insa-lyon.fr
ScSo	**ScSo*** M. OBADIA Lionel Sec : Viviane POLSINELLI Insa : J.Y. TOUSSAINT	M. OBADIA Lionel Université Lyon 2 86 rue Pasteur 69365 LYON Cedex 07 Tél : 04.78.69.72.76 Fax : 04.37.28.04.48 Lionel.Obadia@univ-lyon2.fr

*ScSo : Histoire, Geographie, Aménagement, Urbanisme, Archéologie, Science politique, Sociologie, Anthropologie

Abstract

Bone is a hierarchically organized, multiscale composite with remarkable abilities to repair, adapt and maintain itself. In the bone cortex, the basic structural and functional unit is the osteon, a cylindrical layered structure surrounding a vessel canal (diameter ≈ 200-300 μm, in human bone). The osteocytes are the most abundant and longest living bone cells, embedded in the mineralized bone matrix and regularly distributed within the osteons. They are interconnected with each other and with the vessel canals through dendrites, located in slender canals called canaliculi. The osteocyte lacunae, cavities in which the cells are located, together with the canaliculi form a communication network throughout the bone matrix, permitting transport of nutrients, waste and signals. These cells were considered passive for a long time, but in the last decades it has become increasingly clear their role as mechanosensory cells and orchestrators of bone remodeling, and hence their responsibility for bone quality. Today great interest is given to the osteocytes and the lacuno-canalicular network.

Despite recent advances in imaging techniques, none of the available methods can provide an adequate 3D assessment of the lacuno-canalicular network. This is due to its situation in the hard mineralized matrix, combined with its characteristic 3D complexity, the nanoscale size of canaliculi (~ 300-900 nm in diameter in human bone) and the necessity to assess it in a relatively large volume of tissue, in order to achieve a statistically significant evaluation. In this context, many questions about the 3D architecture of the osteocyte network, and its relation with age, disease or mechanical loading, are unanswered.

The aims of this thesis were to achieve three-dimensional (3D) imaging of the osteocyte lacuno-canalicular network with synchrotron radiation X-ray computed tomography (SR-CT) and to develop tools for 3D visualization and segmentation of this cell network, leading towards automatic quantification and analysis of this structure.

We propose to use parallel beam synchrotron X-ray computed tomography to image in 3D the lacuno-canalicular network in bone. This technique can provide 3D data on both the morphology of the cell network and the composition of the bone matrix. With a pixel size set at 280 nm and a 2D detector composed of 2048×2048 elements, the imaged volume corresponds to ~ 574^3 μm^3. Compared to the other 3D imaging methods with comparable spatial resolution, this enables imaging of tissue covering a number of cell lacunae three orders of magnitude greater in a single image, in a simpler and faster way. This makes possible the study of sets of specimens in order to reach biomedical conclusions. The main challenges to surpass in order to attain imaging of this structure with SR-CT are related to the very high spatial resolution required to resolve the canaliculi (minimum pixel size reachable is 280 nm), combined with difficulties

related to radiation exposure. We could establish valid imaging setups and protocols, based on two insertion devices.

Furthermore, we propose the use of a new synchrotron X-ray tomography technique, dubbed magnified holotomography, to image the ultrastructure of bone tissue. By using a divergent beam, this method can reach a higher resolution (nominal pixel size 60 nm, field of view ~ 120^3 μm^3). The tomographic reconstruction is no longer based on the angular X-ray attenuation maps, but on phase maps, obtained after the application of a suitable phase retrieval algorithm. The phase is retrieved from projections recorded at four different distances between the sample and the detector, for each rotation angle. The reconstructed image corresponds to the 3D distribution of the complex refractive index of the specimen, which is related to the 3D electron density. This technique permits assessment of the cell network with higher accuracy and it enables the three-dimensional organization of collagen fibres organization in the bone matrix to be visualized for the first time.

In order to obtain quantitative parameters on the geometry of the cell network, this has to be separated from the bone matrix. The segmentation needs to be automatic, given that each image contains about 3 000 cell lacunae with more than 100 000 canaliculi. Due to the limitations in spatial resolution, canaliculi appear as 3D tube-like structures measuring only one to three voxels in diameter. This, combined with the noise and the low contrast of the images, and the large size of each image (8 GB), makes the segmentation a difficult task.

We propose an image enhancement method, based on a 3D line filter combined with bilateral filtering, which reintroduces in the filter map the grey level information from the original image. This enables improvement in canaliculi detection, reduction of the background noise and cell lacunae preservation. For the image segmentation we developed a method based on variational region growing. We propose two expressions for energy functionals to minimize in order to detect the desired structure, based on the 3D line filter map and the original image. Future work will focus on improving the segmentation results and the development of automatic quantification techniques.

Preliminary quantitative results are extracted based on a connected components analysis and a few observations related to the bone cell network and its relation with the bone matrix are presented.

Contents

Part A

Part B

Part A

Background

Chapter 1

Introduction

Despite its apparent rigidity, bone is a dynamic tissue which throughout the life is continually remodeled in response to environmental stimuli. The old or damaged tissue is resorbed by specialized multinucleate cells and replaced with new bone through a process known as bone remodeling. This regulatory process enables the seemingly inert tissue to maintain itself. The mechanisms involved in triggering bone removal and formation at different hierarchical levels, are very complex and still unexplained.

Although bone is strong, tough and able to repair itself, it can become fragile and fail due to aging or disorders. Fragility fracture caused by osteoporosis has become a severe public health concern with the aging population. The International Osteoporosis Foundation reports that currently a third of the female and a fifth of the male world population with age over 50 is affected by osteoporosis. The incidence of hip fracture is expected to increase with about 270% in the next decades. The consequences of bone diseases on life quality and on the health care expenses are dramatic. Understanding the mechanisms determining bone strength and fragility is the prerequisite for advances in disease treatment and bone tissue engineering.

It has been observed that bone responds to applied strenuous loading with tissue renewal and conversely, to lack of mechanical stimuli with bone resorption. The translation and propagation of mechanical signals into biochemical signals interpreted by cells is called mechanotransduction. This process is not fully elucidated today but it has become increasingly evident that the osteocytes, the most abundant bone cells, are the key elements of mechanotransduction. They act as mechanosensors and orchestrators of bone remodeling. These cells are located all over the mineralized bone matrix and they are interconnected via cytoplasmic processes.

The lacuno-canalicular network (LCN) is the imprint of the osteocytes and their processes, enabling transport of fluids, nutrients, waste and signals through the hard matrix. Recent studies underlined the role of the lacuno-canalicular porosity as the structure mediating mechanosensing. Strain-derived flow of interstitial fluid through this porosity seems to mechanically activate the osteocytes (J Klein-Nulend et al., 1995) (Elisabeth H. Burger & Jenneke Klein-Nulend, 1999) (Elisabeth H. Burger et al., 2003).

The architecture of the LCN can vary as function of animal species, bone type and location, age and health condition. The influence of the LCN anatomy on solute transport, therefore on bone metabolism and mechanotransduction is not well understood yet (Zhou et al., 2009). The ability to visualize and assess in three-dimensions the lacuno-canalicular network is the precondition for deeper understanding of the mechanisms governing the bone remodeling. This has been limited by the lack of investigation techniques capable to cope with the requirements imposed by the intrinsic characteristics of this structure.

The objectives of this work were to propose imaging techniques adapted for the three-dimensional appraisal of the bone lacuno-canalicular network, and to develop tools for visualization and segmentation of this structure.

In chapter 2 we aim to familiarize the reader with the structure that we seek to image. Firstly we introduce the bone cell network in the context of the multiscale organization of the skeleton. Secondly we emphasize the role of this system in controlling bone quality, quantity and ultimately health. Concurrently we seek to give an idea on the depth of knowledge acquired so far about the osteocyte system. Additional results from the literature are referenced within the text of the chapters 8 and 9, which are paper manuscripts submitted for publication.

In chapter 3 we briefly review imaging techniques which have been used to investigate the osteocyte network, mentioning their advantages and drawbacks.

Chapter 4 describes the instrumental and theoretical aspects of the synchrotron X-ray tomography (SR-CT), the method we employed for imaging the lacuno-canalicular network.

Chapter 5 presents our work related to image acquisition with parallel beam SR-CT. An evaluation of the imaging performance with different setups is made, some acquisition protocols are suggested and the obtained results are demonstrated.

In chapter 6 we propose a method of image enhancement, based on 3D line filter and nonlinear bilateral filtering.

Chapter 7 presents an automatic segmentation method suited for the osteocyte network, based on variational region growing. Two adapted energy functionals are proposed, validated and compared with a few functionals from the literature.

Chapter 8 describes the results obtained with parallel beam SR-CT. This method enables imaging of the lacuno-canalicular network in a cylindrical tissue region measuring about $1.48 \cdot 10^8$ μm^3. This includes typically more than 3 000 cell lacunae. Some preliminary quantitative results are given.

Chapter 9 presents the results obtained with magnified holotomography. This technique achieves a higher spatial resolution which permits the visualization of collagen fibres in the bone matrix. The grey level in the reconstructed images is related to the electron density of the material which can be correlated with the degree of mineralization. Information which can be directly observed is reported. Some proof-of-concept measurements are performed and unique three dimensional images are presented.

Finally, in chapter 10, we conclude this thesis and suggest some future perspectives.

Annex I includes a paper published in the Proceedings of IEEE International Symposium on Biomedical Imaging (ISBI) - 2011, proposing a segmentation method based on geodesic level sets.

Chapter 2

Bone structure and function

2.1 The hierarchical structure of bone

Bone tissue is organized hierarchically, from the macroscale to the nanoscale. The structure and composition of bones have evolved to provide strong internal support for the body and protection of the vital organs, while assuring easy and free locomotion.

The ensemble of bones forms the skeleton, whose parts are classified at the largest scale as long (e.g. femur, humerus), short (e.g. ankle, wrist), flat (e.g. skull, pelvis), or irregular (e.g. vertebrae, jaw). All bones contain two distinctive architectural parts, the spongy or trabecular bone, located in the inner side and the compact or cortical bone, forming the outer shell (Figure 1). Since they are organs, bones are composed of multiple tissue types like osseous tissue, cartilage, fibrous connective tissue, vascular, lymphatic, nervous and adipose tissue.

The external surface of the bone is covered with a connective tissue called periosteum forming a double-layered membrane. The inner layer contains osteoblasts, which are bone forming cells, and cells that eventually differentiate into osteoblasts. Similarly, the internal surface of the bone is overlaid with the endosteum which covers the trabeculae of spongy bone in the marrow cavities and lines the canals passing through compact bone. This tissue contains osteoblasts and osteoclasts, responsible for bone resorption. In the medullary cavity of long bones and in larger Haversian canals there is bone marrow, a soft tissue producing blood cells and lymphocytes.

Initially a primitive form of spongy bone with an anarchic organization is developed. This immature tissue is known as “woven bone” and it is found temporarily in the embryo, in children and in cases of bone fracture repair.

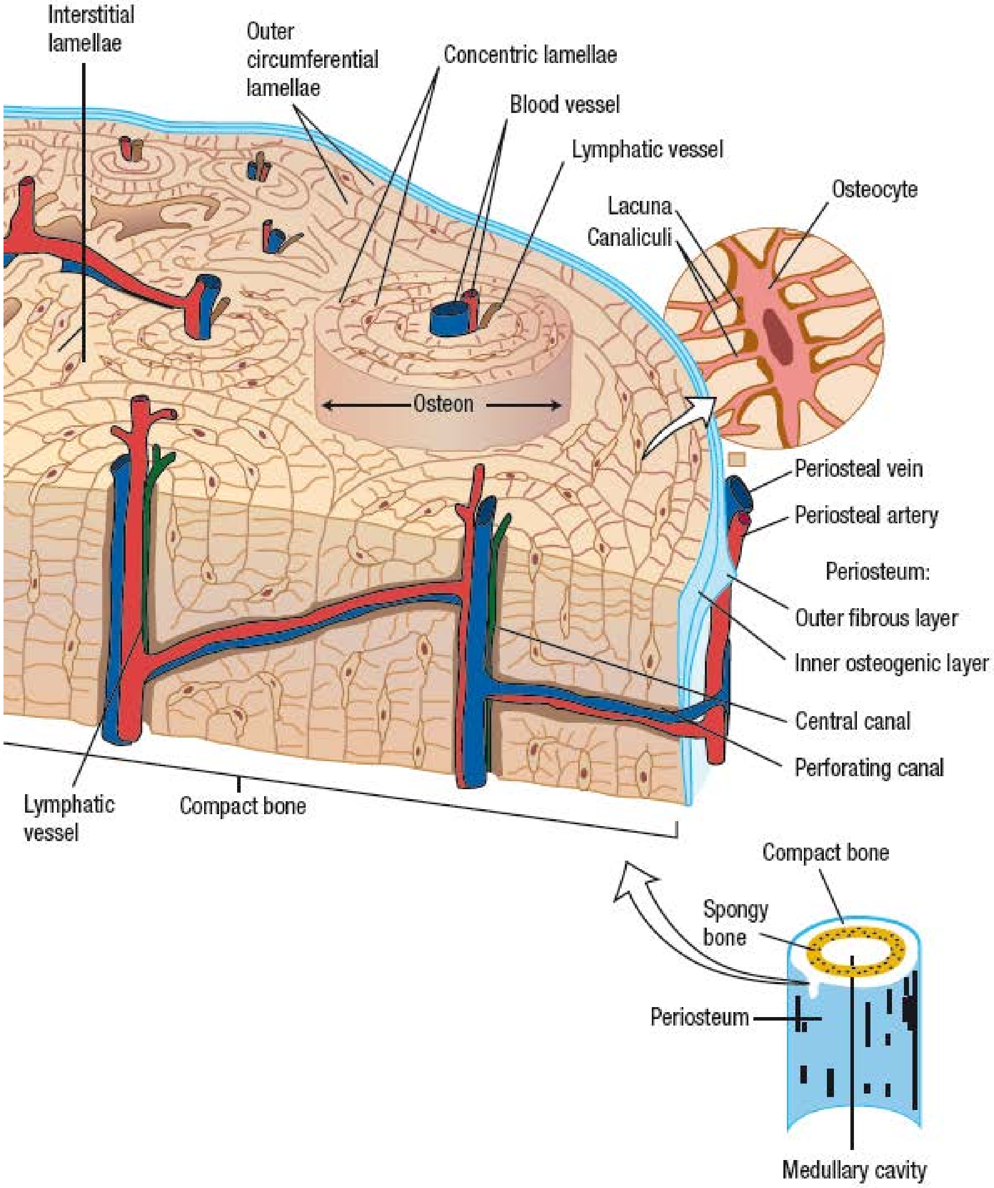

Figure 1 Anatomy of compact bone. The primary structural and functional unit of cortical bone is the osteon, composed of concentric lamellae interspersed with osteocytes, enclosing in the middle a canal containing blood and lymphatic vessels and nerves. Image from (Taylor et al., 2007).

The woven bone evolves into mature or lamellar bone in which the cells and the components of the bone matrix are regularly arranged.

The cortical tissue, on which we focused for this thesis work, is structured in three lamellar arrangements: the osteons, the interstitial tissue and the *circumferential systems*. The later ones are situated at peripheral areas, adjacent to periosteum and to endosteum, surrounding the bone in a continuous manner.

The o*steons* or Haversian Systems are the fundamental structural and functional units in cortical bone. The are formed of concentric cylindrical lamellae surrounding a central vascular canal called Haversian canal (Figure 2). Osteons have diameters of 150 to 300 μm in human bone, present 4 to 20 lamellae and they are interspersed with bone cells. These structures act as weight-bearing pillars orientated along the loading directions (Bilezikian et al., 2002). They can communicate with neighboring osteons through Volkmann's vessel canals, orientated mainly perpendicularly to Haversian canals. The ratio of osteons to interstitial systems is proportional with age, making it possible to age a piece of bone in this way (Frost, 1987).

The *interstitial lamellar tissue* is remnant from old osteons after remodeling and they fill the space between these cylindrical structures. The Haversian systems can be delimited from the interstitial tissue based on several elements. Firstly, they are delimited by a thin circumferential wall called *cement line* (Figure 3). This structure is probably stiffer and more mineralized than the rest of bone matrix (Skedros et al., 2005). However, the opinions are divergent because some imaging techniques show the contrary, that they are hypomineralyzed (Schaffler et al., 1987). Secondly, the osteons are generally less mineralized than the interstitial tissue, since they are results of bone renewal, hence younger tissue, which mineralizes progressively. Moreover, osteons can be identified based on the changes in organization of lamellae and cells.

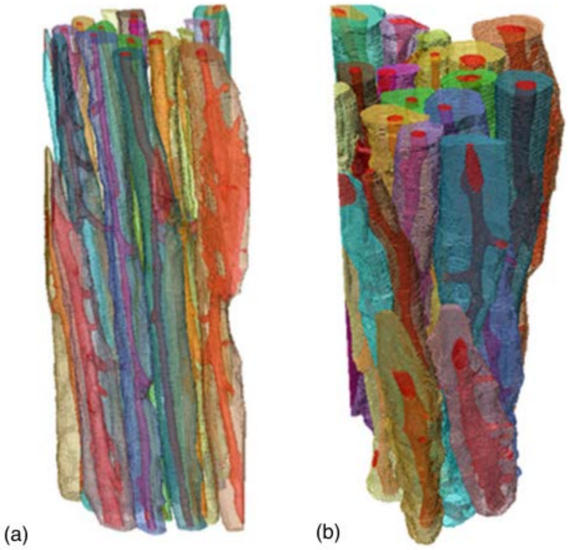

Figure 2 Osteons. Three-dimensional rendering of osteons in human femoral bone, segmented from images acquired with micro-CT (Arhatari et al., 2011)

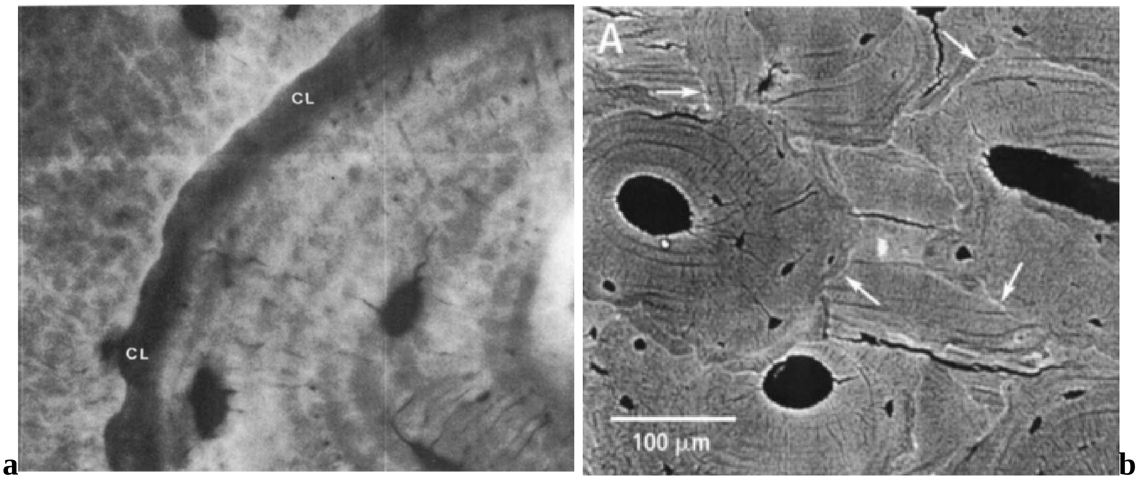

Figure 3 Cement lines. a) Backscattered electrons micrograph showing a hypomineralyzed cement line (CL) (Schaffler et al., 1987) b) Backscattered electron micrograph showing that cement lines are hypermineralized (Skedros et al., 2005).

The detailed anatomy of the lamellae is not fully elucidated. Different imaging techniques revealed an alternation of thick, “loose” and thin, “dense” lamellae in the osteon (Figure 4). This bimodal aspect is explained in two main different ways in the literature. On one side this is thought to be due to dissimilarities in density and on the other side it is associated to variations of the orientation of fibres. Marotti concluded from Scanning Electron Microscopy (SEM) and Transmission Electron Microscopy (TEM) observations that lamellar bone is made up of alternating collagen--rich (dense lamellae) and collagen-poor (loose lamellae) (Marotti, 1993).

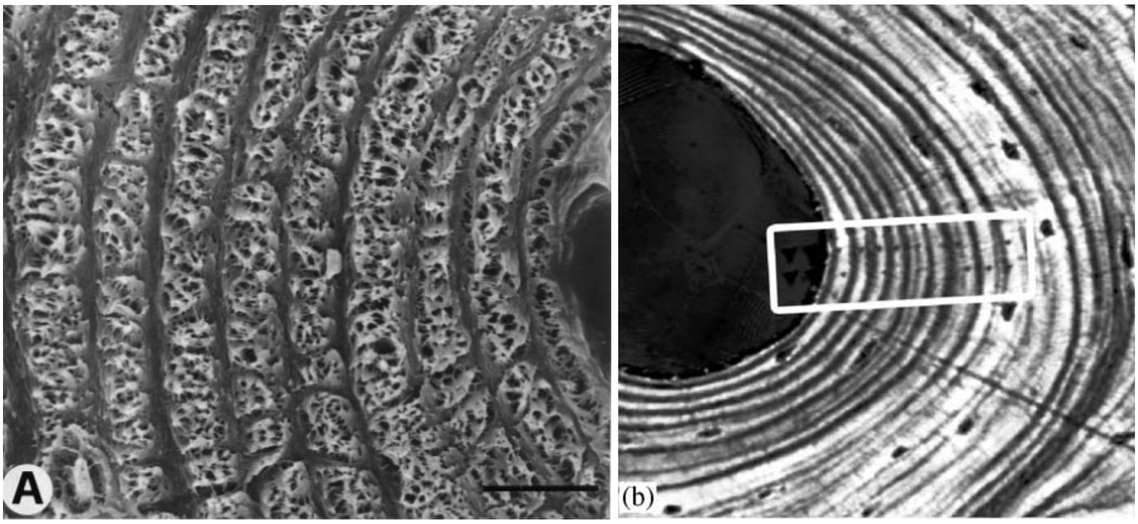

Figure 4 Lamellae in osteons. a) SEM – Lamellae in secondary osteons in human tibia. “Collagen-rich non-osteocytic layers (dense lamellae)” and “collagen-poor osteocytic layers (loose lamellae)”. Scale bar 10 µm (Ardizzoni, 2001). b) Seeing the elastic properties: the change of impedance of a lamella from high to low values on adjacent sides of the Haversian canal (Hofmann et al., 2006).

After examination with polarizing light microscopy, synchrotron X-ray diffraction and confocal microscopy, Ascenzi et al. explain differences between dark and bright lamellae through the orientations of collagen bundles and hydroxylapatite crystals (Maria Grazia Ascenzi et al., 2003). Hofmann et al. performed studies with acoustic microscopy and Raman microspectroscopy showing a pattern of alternating high and low impedance values related to variations of the lamellar orientation (Hofmann et al., 2006).

At the microscopic scale, the bone tissue is constituted of cells and bone matrix. Three types of bone cells can be distinguished: osteoblasts, osteocytes and osteoclasts (Figure 5). The osteoblasts are the bone forming cells, localized on the boundaries of the developing region. Osteoblasts synthesize and secrete the collagen fibers and initiate the process of calcification. The osteocytes are the most numerous and longest living bone cells (~25 years), spread throughout the bone matrix. They develop from osteoblasts trapped in the mineralizing bone matrix (Franz Odendaal et al., 2006). Osteocytes are hosted in fitted micro-porosities called lacunae and communicate with each other via a dense network of cytoplasmic processes located in slender channels called canaliculi.

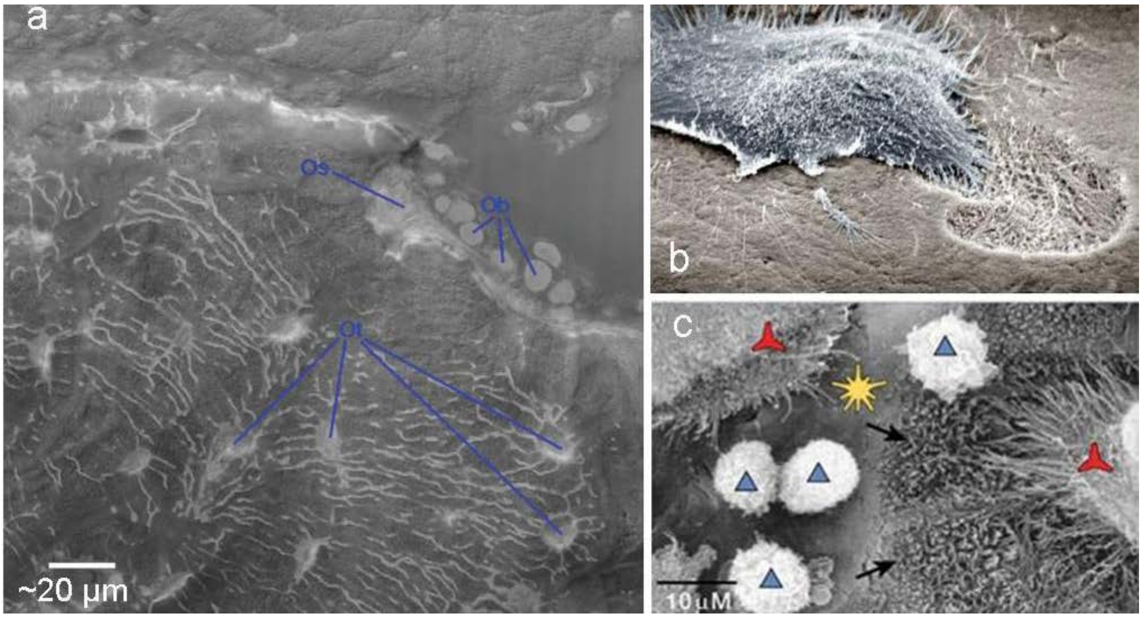

Figure 5 Bone cells. a) Confocal micrograph showing bone remodeling: osteoblasts (Ob) form the osteoid (Os) in which some of them remain enclosed, becoming osteocytes (Ot) (Melissa L. Knothe Tate, 2003)**. b) SEM image of an osteoclast and the resorption pit created on the bone surface (Image credits: Tim Arnett, UCL Research Department of Cell & Developmental Biology*)* c) SEM image of human osteoclasts on cortical bone slices. Red propellers mark osteoclasts, black arrows - a resorption pit where the normally smooth lamellar bone surface has been resorbed to expose collagen bundles; yellow star, non-resorbed bone surface; blue triangles, mononuclear cells (potential osteoclast precursors) (Boyle et al., 2003).**

Because the bone matrix is calcified there is little possibility of diffusion except via the network of canaliculi. Initially considered to be inactive, the osteocytes have been proven to have an essential role in bone remodeling. Osteoclasts are the largest of bone cells (20-100 µm in diameter) responsible for the bone resorption. Osteoclasts are multinuclear (up to 50 nuclei).

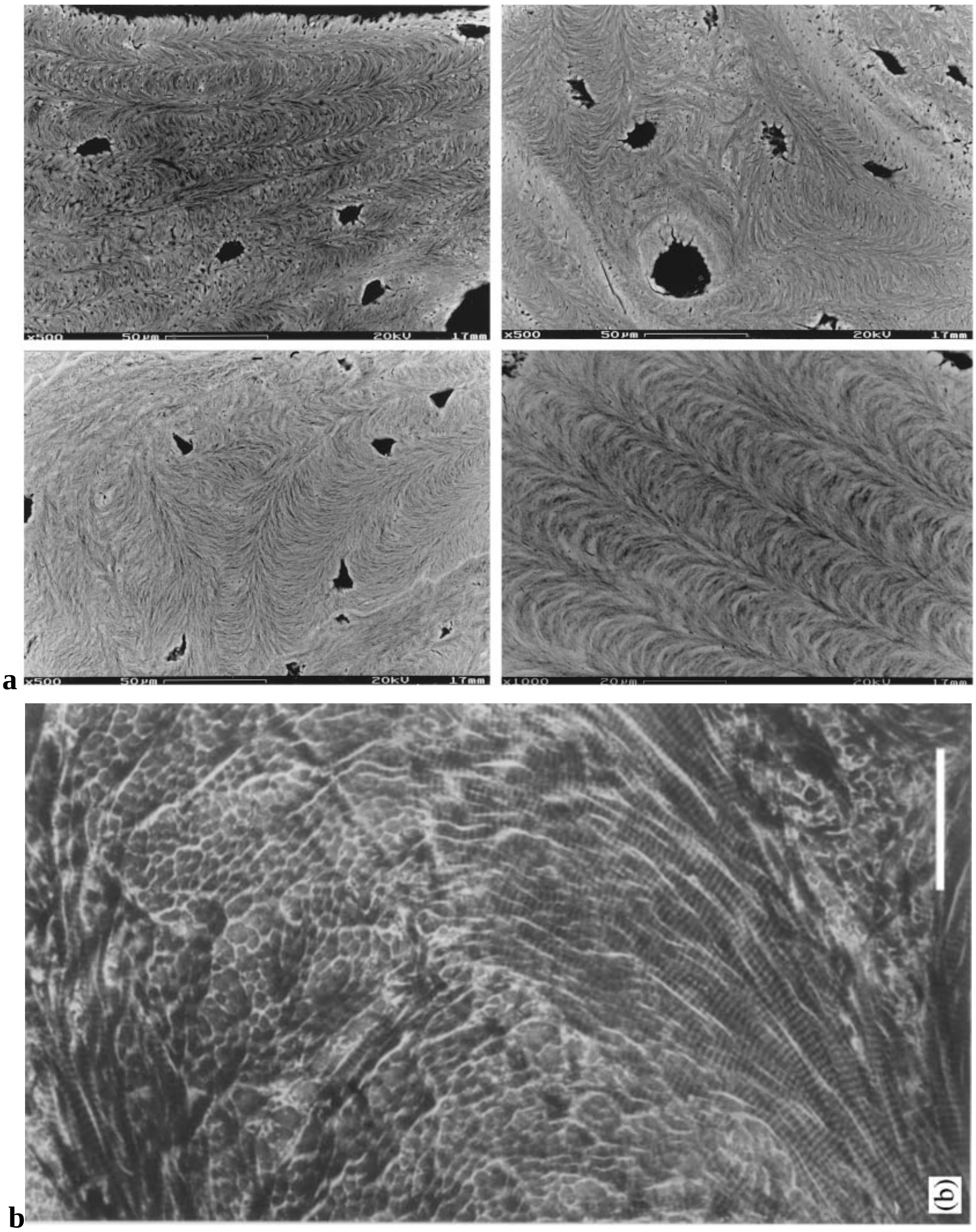

Figure 6 Ultrastructure. Pattern formed by collagen fibres interlaced with hydroxylapatite crystals. a) Quantitative backscattered electron images showing collagen orientation in human (60-90 years old) mandible cortex, on a 0.5-1 µm surface layer (Kingsmill & A. Boyde, 1998). b) Collagen fibrils orientation in osteon seen on ultra thin section from decalcified compact bone with TEM. Scale bar 100 nm (Giraud-Guille et al., 2003).

At a finer scale, the ultrastructure of bone is formed of collagen fibres and hydroxylapatite (HA) crystals (Figure 6). These components are interleaved, forming orientated patterns. The regular arrangement and orientation of collagen and HA crystals is believed to play an important role in bone strength and quality (Giraud-Guille et al., 2003). Investigations at this level have been limited to 2D sections so far.

2.2 Bone composition

The bone matrix contains a mixture of inorganic and organic components (Figure 7). The mineral part (~ 66% of the weight) consists mainly of two inorganic salts, calcium phosphate and calcium hydroxide, forming the hydroxylapatite compound. Bone also contains small amounts of magnesium, fluoride, and sodium. The organic part is made of proteins, of which about 95% is collagen.

The collagen provides bone with elasticity and the ability to resist stretching and twisting. The mineral part gives the hardness of the bone and the capability to resist compression. These two complementary components, combined with the hierarchical multiscale organization of the structure, provide bone with remarkable properties as a composite.

Figure 7 shows two pieces of a bone specimen which have been chemically treated to conserve only the mineral or only the organic part. One can observe that collagen undergoes shrinkage due to drying.

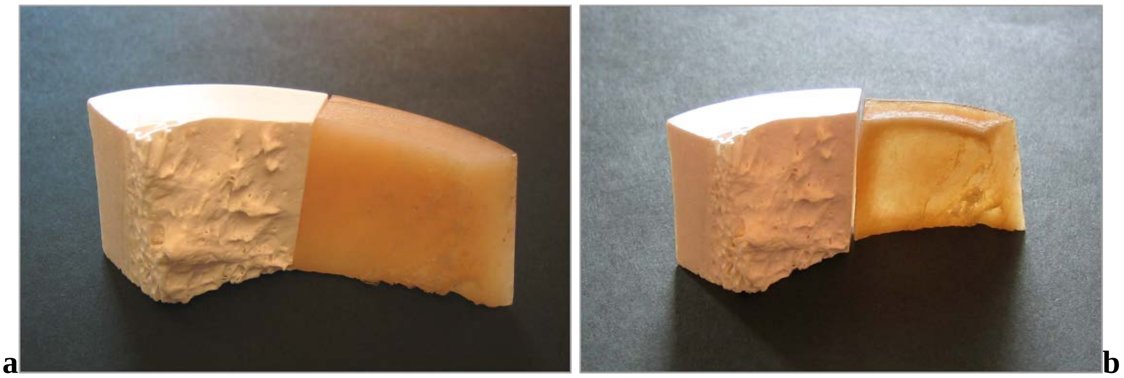

Figure 7 Bone tissue composition a) The left part of a bone specimen was treated with hypochlorite which removes the collagen but conserves the mineral. The right part was treated with hydrochloric acid to dissolve mineral, keeping the collagen intact. b) The same bone samples after collagen drying, leading to shrinkage. (Image credits: Tim Arnett, UCL Research Department of Cell & Developmental Biology*)*

2.3 Bone adaptation and mechanotransduction

Julius Wolff postulated in the 19th century that bone tissue can adapt its mass and architecture to mechanical usage, optimizing itself for the load bearing needs while pairing maximal strength to minimal weight (Wolff, 1892). Since then, numerous studies on the effects of mechanical stress on the bone organization and mass have been conducted (R. Huiskes, 2000), leading to acknowledgment of the Wolff's law. It has been shown that the 3D organization of both trabecular and compact bone changes in accordance with the direction of the main mechanical stresses.

Bone remodeling is a regulatory process governed by mechanical usage and probably orchestrated by osteocytes (Elisabeth H. Burger & Jenneke Klein-Nulend, 1999) (Bonewald, 2011). This is possibly due to mechanotransduction, the process by which mechanical energy is converted into electrical or biochemical signals. Many questions regarding how this process works and the mechanisms involved at the level of cells, osteons and trabeculae are unanswered.

Turner formulated three basic rules governing bone adaptation (Turner, 1998). These include that it is driven by dynamic, rather than static, loading and that the initiation of adaptive response requires only a short duration of mechanical loading. The third rule stated that bone cells adjust their response to mechanical environment, in the sense that they are less responsive to routine loading signals.

Bone adaptation to the external mechanical environment is generally a desirable phenomenon. However, in cases of long duration bed resting, or in microgravity, as occurring during spaceflight, this process has negative effects on the skeleton, leading to bone loss (Morey & Baylink, 1978) (J. Klein-Nulend et al., 2003).

2.4 The osteocyte

Osteocytes are formed by the embedding of osteoblasts into the bone matrix. From the cell bodies, slender cytoplasmic processes radiate in all directions, with the highest density perpendicular to the bone surface (P.J. Nijweide et al., 2002). With a spider-like morphology (Figure 8), the osteocyte lacunae and their radiating canaliculi form a network providing the site for information transmission and detection, underlying

Wolff's law of adaptive bone remodeling (J Klein-Nulend et al., 1995). This sensitive structure is somewhat analogous to the nerve system. It has been proposed that osteocytes can detect microcracks in their vicinity. This is explained by the microcracks severing the cell processes inducing cell apoptosis (i. e. programmed death), thereby activating bone remodeling (Hazenberg et al., 2006).

Besides the mechanical factors, osteocytes are influenced by hormonal balance. It has been shown that loss of estrogen (Tomkinson et al., 1998) and glucocorticoid treatment (Weinstein et al., 1998) induce osteocyte apoptosis. Apoptosis of osteocytes could have both positive and negative effects. Cell death provoked by treatment or disorders might disturb the bone regulation, leading to bone fragility and the diseases related to this (Busse et al., 2010).

Only a few quantitative studies giving 3D parameters on the osteocytes and their lacunae are available in the literature, usually inferred from 2D data. The number of lacunae per unit volume varies from 10 000 mm^{-3} (Marotti et al., 1995) to 90 000 mm^{-3} (Hannah et al., 2010). The size of osteocyte lacunae has been shown to decrease concentrically in osteons (Marotti, 1977) (Marotti, 1979). The shape of lacunae has been found to vary between different bones depending of the level of loading they are normally exposed to (ex. calf bone and skull), reinforcing their mechanosensing ability (Vatsa et al., 2008). Moreover, the morphology of osteocyte lacunae was reported to be influenced distinctively by diseases like osteoarthritis, osteopenia and osteopetrosis (van Hove et al., 2009).

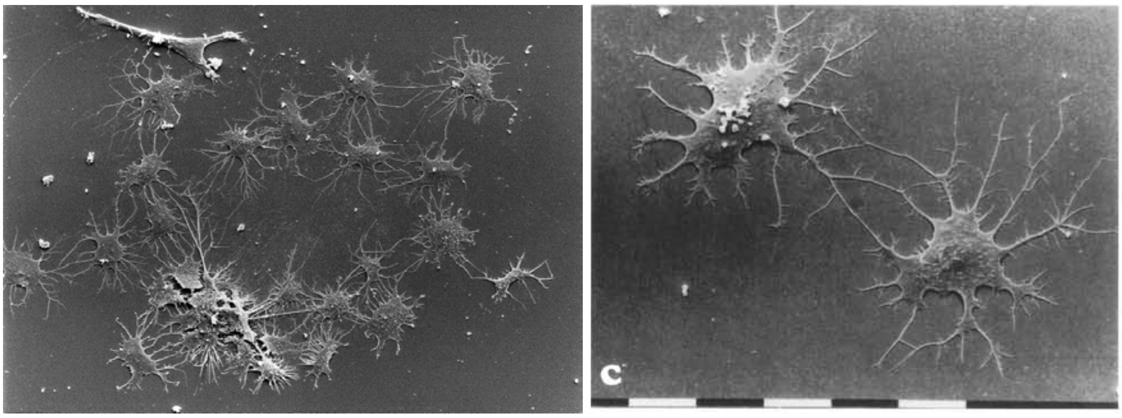

Figure 8 SEM of a group of osteocytes, isolated from embryonic chicken calvaria, after 3 days of culture as monolayer. The cells have re-established a cellular network by moving away from each other and making branching cell processes that connect with those of neighboring cells. (Elisabeth H. Burger & Jenneke Klein-Nulend, 1999) & (P.J. Nijweide et al., 2002)

While their location inside the entire bone matrix, regularly distributed in 3D, enables the osteocytes to locally supervise the quality of the tissue, this also makes them difficult to access and study.

2.5 The lacuno-canalicular network

The lacuno-canalicular network is the imprint of the osteocyte system, reflecting the shape, organization, integrity and connectivity of the osteocytes and their cytoplasmic processes. The canaliculi link osteocytes and blood vessels extensively. The connection points of canaliculi belonging to two different cells are known as gap junctions. The ability to investigate in 3D this structure is essential for biomechanical studies, for understanding fundamental aspects of bone remodeling and for development and testing of treatment strategies at a cellular level. Due to limitations of the imaging techniques, this network has been mostly assessed from 2D sections. The recent augmentation of interest in a deeper exploration of this structure motivated the research into 3D imaging of the network.

It is supposed that due to mechanical loading and deformation there is a flow of interstitial fluid through the canalicular network, which is directed away from regions of high strain (Elisabeth H. Burger et al., 2003). The possibility of studying this phenomenon can potentially offer answers to questions regarding bone regulation and adaptation. Estimating the local permeability coefficients of the lacuno–canalicular porosity based on the number, size and distribution of the canaliculi is a prerequisite for further understanding mechanotransduction (Beno et al., 2006).

Canaliculi have rarely been quantified. Their thickness in human bone is estimated to vary between ~ 300 and ~ 900 μm (Marotti et al., 1995) (Atkinson & Hallsworth, 1982). They seem to branch after emanating from lacunae. Beno at al. found that about 52 canaliculi leave from each lacuna and their number increased to around 116 after branching (Beno et al., 2006).

Presumably the lacuno-canalicular network plays a role in repairing tissue damage at the macroscale as well. The function and behavior of the osteocyte network in fracture repair has been little investigated. It appears that osteocytes are present during the first stages of ossification post-fracture, but their canaliculi are fewer, shorter and tortuous.

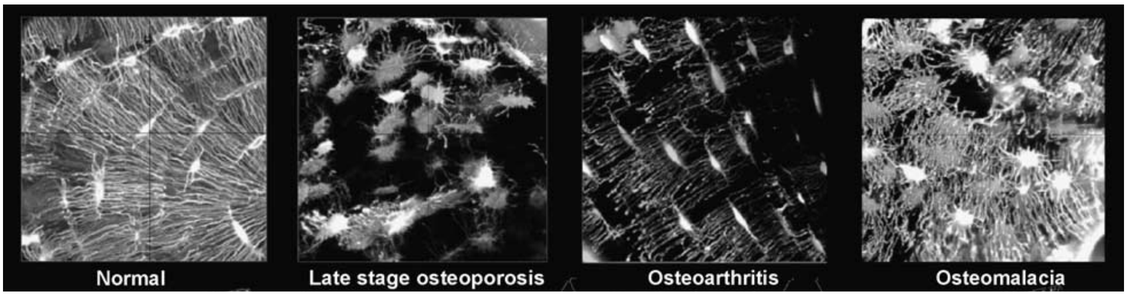

Figure 9 Influence of pathology. Confocal microscopy showing variations in the architecture of the LCN with respect to tissue pathological state, in human cortical femoral neck. In case of osteoporosis a decrease in connectivity as well as loss of orientation is observed; Osteoarthritic bone exhibits a decrease in osteocyte viability and connectivity, although the orientation of the processes remains intact; in osteomalacic bone cells appear viable with high connectivity, but cell processes are tortuous and the network is disorganized (Melissa L. Knothe Tate et al., 2004).

At a later stage, osteocyte lacunae are arranged regularly and the canaliculi are long and fairly straight (Shapiro, 1988), (Kusuzaki et al., 2000).

Although very little studies have been performed, it has been suggested that the architecture and organization of the lacuno-canalicular network is reflecting the pathological state of the tissue (Figure 9) (M. Knothe Tate et al., 2002), (van Hove et al., 2009).

We close this chapter with a quotation from (M. Knothe Tate et al., 2004) stating that “technology will broaden our perspective from an understanding of how bone tissue adapts to its dynamic environment to the degree to which pathological tissue is compromised in its ability to adapt”.

Chapter 3

Imaging the lacuno-canalicular network - state of the art

In this chapter we briefly review the methods reported in the literature for the investigation of the lacuno-canalicular network. The lacuno-canalicular network gained scientific interest since the 1950s. Most of the quantitative studies have been based on 2D techniques. Recently, a few 3D methods were suggested, but have not yet become feasible for comprehensive and extensive studies.

3.1 Light microscopy

The oldest, most accessible and still most widely employed microscopes use the visible light and a set of optical lenses to obtain a magnified image of the specimen under study. The basic optical microscopes consist essentially of a combination of two lenses, an objective and an eyepiece. The product of individual magnifications gives the enlargement of the final image.

The contrast is generally due to light absorption and scattering by the sample. Specific dyes are often employed to stain the components of interest. If the specimen has been marked with fluorescent molecules, the illumination is set to a matching wavelength and the targeted structures emit light which is focused in the image.

The theoretical spatial resolution in light microscopy is limited by the wavelength of visible light to about 200 nm, which is in practice further affected by imperfections of the instrument components. Usually the imaged specimens must be cut into thin slices, only a few microns thick, and stained or treated chemically to yield contrast.

Several illumination techniques have been developed over time, suited for different applications. Phase contrast microscopy is a technique proposed by Frits Zernike in the

1930s, awarded with Noble prize in 1953. The contrast in this case appears due to light being retarded differently when traversing the sample, as function of the optical density of different parts of the tissue. It has the advantage that no staining is necessary and it is suited for thin biological specimens which absorb and scatter relatively little. Figure 10b shows a living osteocyte in culture, imaged with phase contrast microscopy.

By immersing both the objective lens and the specimen in a transparent oil of high refractive index, the spatial resolution can be improved. The numerical aperture (NA), which determines the resolution of a lens, is proportional with the refractive index of the medium between the lens and the specimen. In a medium with refractive index higher than air (n≈1), the increased NA permits a higher resolution to be attained, due to the inversely proportional relation of the two measures.

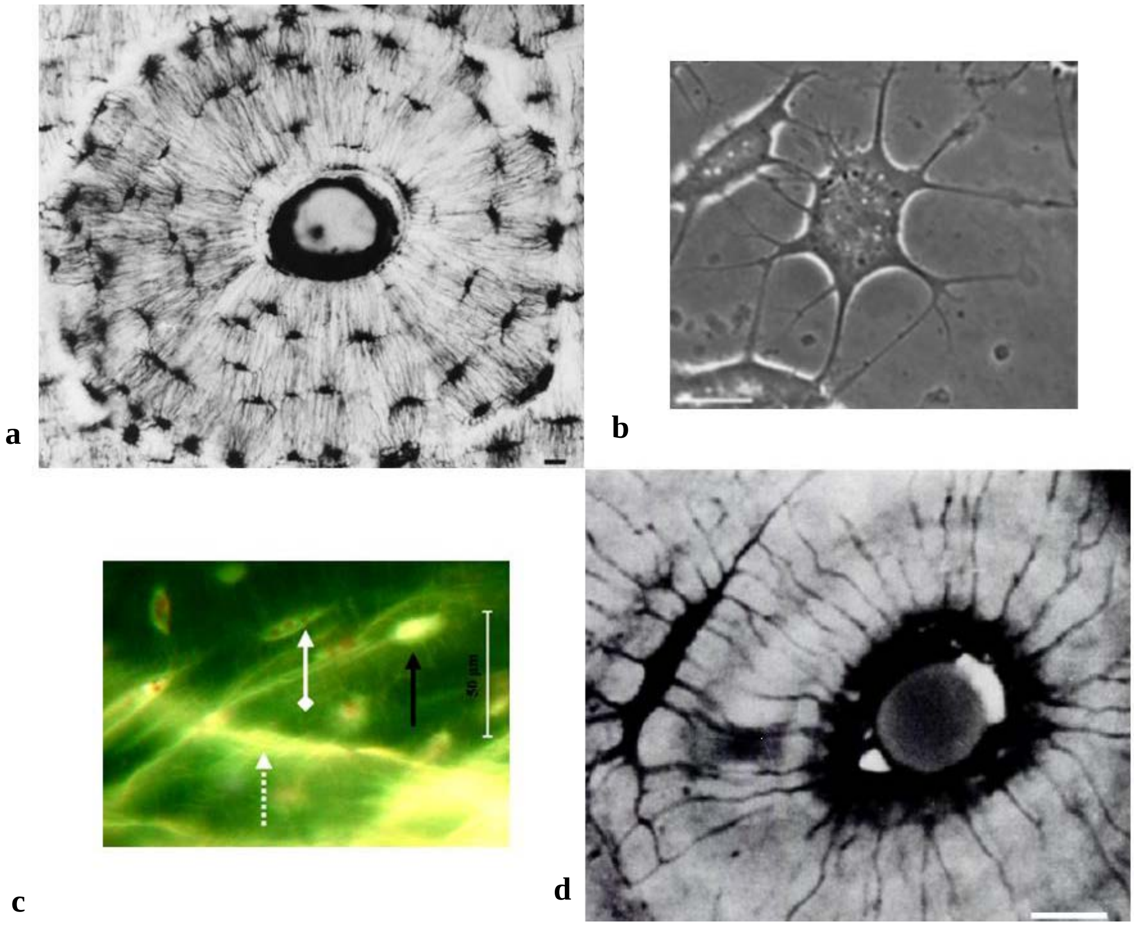

Figure 10 Light microscopy a) Osteon in undecalcified cortical bone from human tibia visualized with light microscopy. Bar is 10 µm. (Ardizzoni, 2001) b) Phase contrast micrograph showing cultured osteocytes (Tanaka-Kamioka et al., 1998) c) Fluorescence microscopy. White arrow – multiple nuclei like structures inside the osteocyte, black arrow – empty lacuna, dotted arrow – crack. (Liao, 2008, JBioMech) d) Oil immersion photomicrograph of femoral cortical bone, after decalcification, plastic-embedding, heavy staining with toluidine, and 3.5 µm thick sectioning (Shapiro, 1988).

Figure 10 shows images of osteocytes or lacuno-canalicular network obtained with four different light microcopy techniques.

Confocal microscopy

Confocal microscopes have been extensively used to image the osteocyte network.

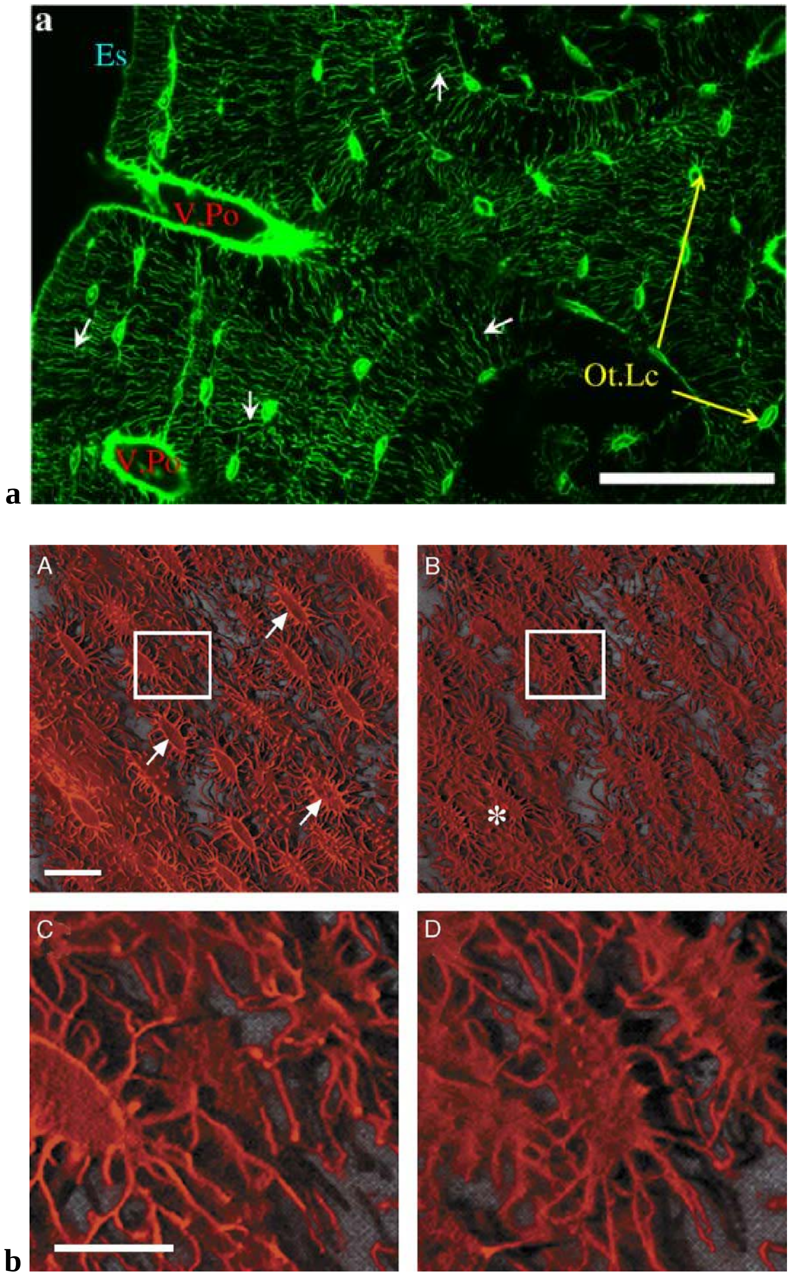

Figure 11 Confocal microscopy a) Cortical bone from rat tibia diaphysis; the staining marks vascular porosity (V.Po), the canalicular porosity (small arrows), and the interstitial space surrounding the osteocyte lacunae (Ot.Lc), (Ciani, Doty, et al., 2009) b) 3D reconstruction from confocal laser scanning microscopy (CLSM) (Sugawara et al., 2005). The specimen was chicken calvaria with 60-80 µm sample thickness, stained with phalloidin. Spatial resolution in plane (*xy*) was 0.263 µm while in depth (*z* axis) it was 0.604 µm. Volume of view covered 146.2×146.2×7.2 µm^3.

These microscopes use point illumination and a pinhole in front of the detector, to eliminate out-of-focus signal. This enables the acquisition of in-focus images from different selected depths. If a laser is used for illumination, the technique is called confocal laser scanning microscopy (CLSM). The duration of image acquisition is quite long due to the point-by-point imaging, combined with the longer exposure times, imposed by the pinhole blocking a significant part of the incoming light.

Since image information from multiple depths in the specimen is not superimposed, a 3D reconstruction of the imaged tissue can be performed. However, the spatial resolution in depth is lower than in plane, leading to distortion and inaccuracy of the 3D image. Confocal microscopy has limited optical penetration depth in bone, restricting the studies to a depth of 20–60 μm. Sugawara et al. reported remarkable results obtained with CLSM in 60 μm thick slices on a field of view of 146×146×7.2 μm (theoretical spatial resolution in plane 0.263 μm and 0.604 μm in depth) (Sugawara et al., 2005) (Figure 11b) .

3.2 Electron microscopy

By using a beam of accelerated electrons to illuminate the specimen instead of visible light, the spatial resolution can be greatly improved, reaching the level of atoms. The first electron microscopes were built in the 1930s and since then several types have been established. The two main families are Transmission Electron Microscopy (TEM) and Scanning Electron Microscopy (SEM). Comparing to optical microscopes, these are more sophisticated and expensive to build and maintain. Usually specimens have to be imaged in vacuum and complex sample preparation is required. The resolving power of electron microscopes gives access to valuable information with applications in biology and medicine.

Transmission Electron Microscopy

Similarly to its optical counterpart, in Transmission Electron Microscopy (TEM) the image is created from the beam transmitted through the sample. The contrast is due to absorption of electrons in the material, as function of composition and thickness of the sample. At very high magnifications, the contrast mechanisms become complex due to wave interactions, making image interpretation difficult. TEM provides the highest resolution images available, going down to sub-angstrom (Erni et al., 2009). This comes with the price of quite extreme specimen preparation requirements, such as sectioning into ultrathin slices (10 to 100 nm), which are difficult to produce and often too small to be representative of the specimen.

Multiple views of the sample mounted on a rotation stage can be acquired at different view angles. This enables the reconstruction of a 3D image, using the filtered backprojection algorithm. Using this method, (Hiroshi Kamioka et al., 2009) obtained images of 3 μm thick sections of bone containing parts of 2-3 osteocyte lacunae and their canaliculi, at a resolution of 35-50 nm. (Figure 12).

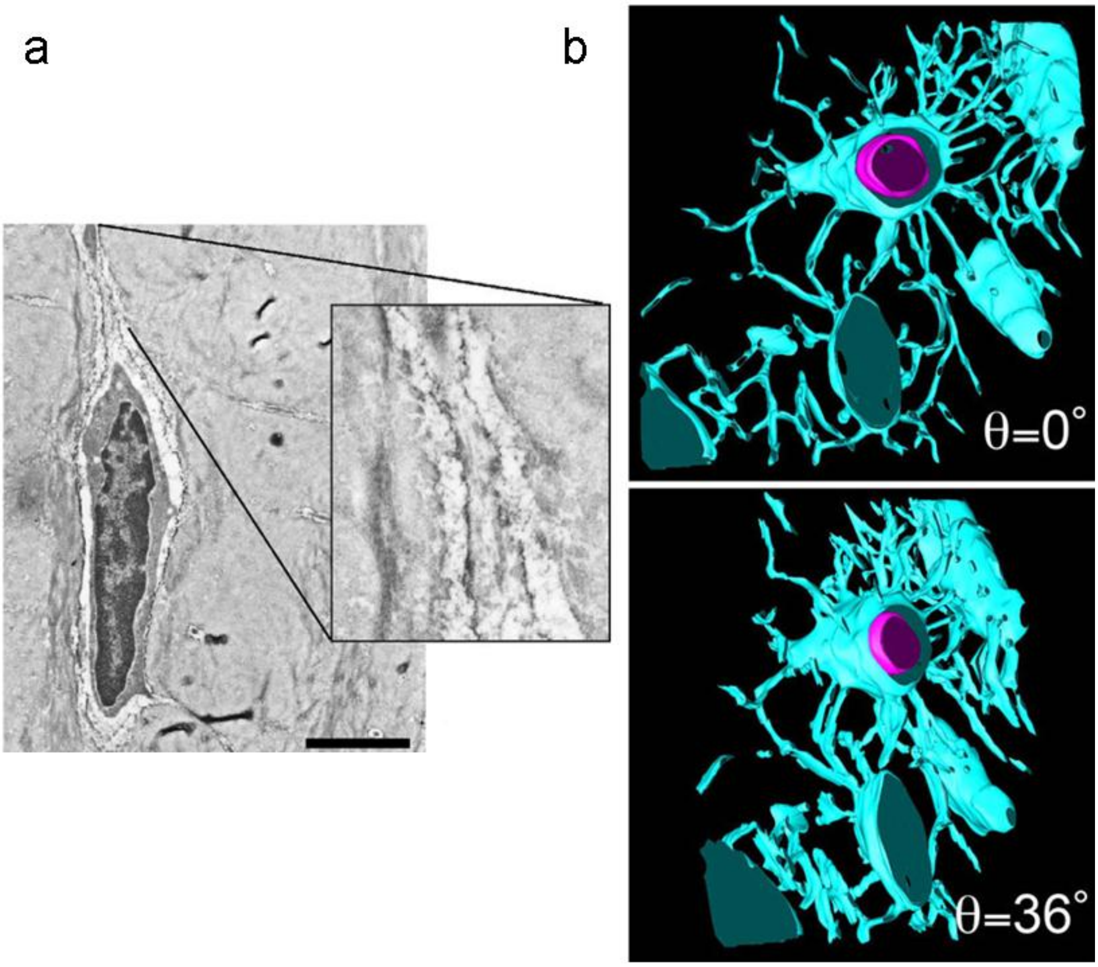

Figure 12 Transmission electron micrographs from 3μm thick sections of bone at a resolution 35 nm -50 nm (16 nm x 2 or 3 pixels). Image from (Hiroshi Kamioka et al., 2009).

Scanning Electron Microscopy

In Scanning Electron Microscopy (SEM) the sample is scanned with an electron beam in a raster pattern. The image is formed from the secondary electrons emitted by the sample, following inelastic scattering interactions (i.e. with substantial energy loss). The obtained information is related to the topography and composition of the sample surface, yielding an image of the surface morphology with a three dimensional appearance.

Comparing to the TEM, this instrument can be used to image comparatively bulky materials since it does not rely on transmitted electrons, thereby slicing down to a few nanometers thickness is no longer imposed. The samples still need to be imaged under vacuum, due to the undesired effects of a gas atmosphere on electron beams. Figure 13 shows several images of bone samples acquired with SEM at the cellular scale.

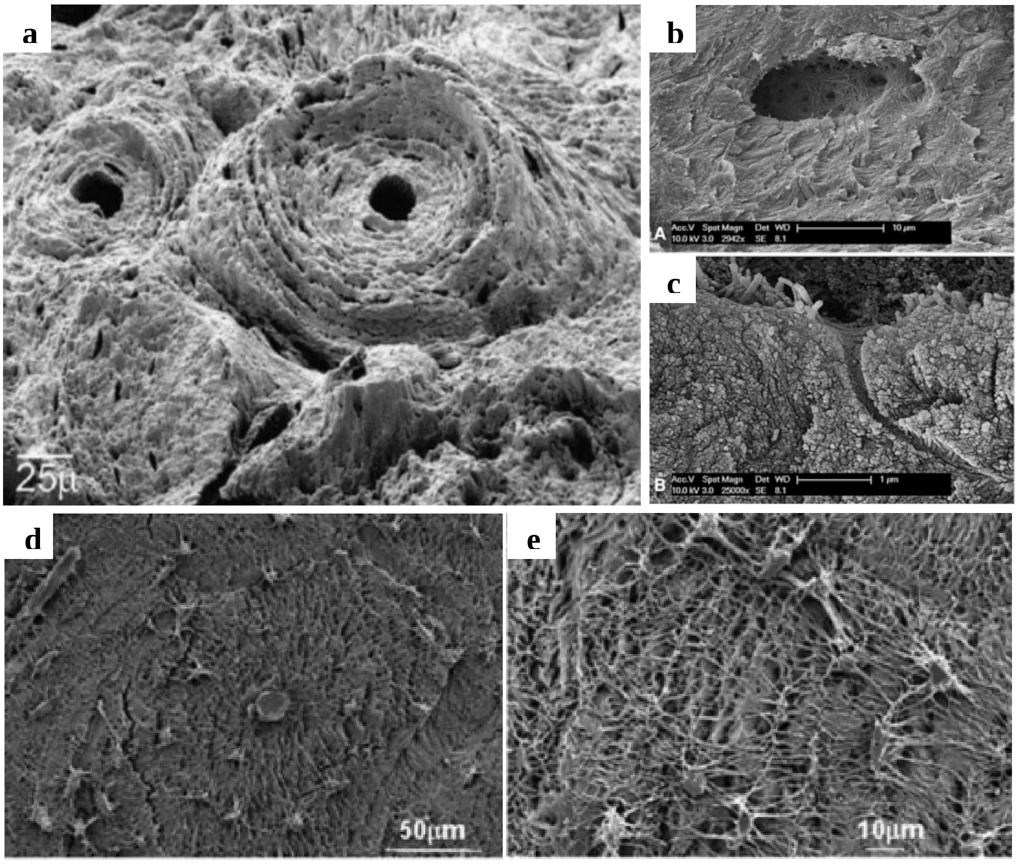

Figure 13 SEM a) Scanning electron micrograph of an osteon on the transverse fracture surface of a cyclically loaded dorsal specimen (Hiller et al., 2003). b) SEM micrograph showing an osteocyte lacuna exposed by fracture.c) A canaliculus spreading out from a lacuna visualized by SEM. Images from (Pazzaglia et al., 2009) d), e) Scanning electron micrographs of bone surface after acid-etching with 9% phosphoric acid for 40 s. Images from (Kubek et al., 2010).

Backscattered electron microscopy

Backscattered Electron Microscopy (BSE) is also a scanning technique. In this case, the electrons of the incident beam that are elastically (i.e. keeping their high energy) scattered backward from the sample, due to the interaction with atoms in the specimen, are used to create an image. The elements with higher atomic number ("heavy" elements) backscatter more electrons than "light" elements, yielding brighter points in the image. This creates contrast between regions with variations in the chemical composition. Dedicated detectors, usually based on scintillation screens, are required to collect the electrons emitted in the solid angle and to form an image.

This technique enables examination of the relative differences of the mineralization degree in bone, although it is not reliable for acquiring absolute values. The surface topography of the specimen is not as accurately resolved as in SEM. Figure 14 shows BSE sections in human bone revealing differences in the mineralization degree. This permits to study as well hypermineralized lacunae, canaliculi and Haversian canals (Kingsmill & A. Boyde, 1998).

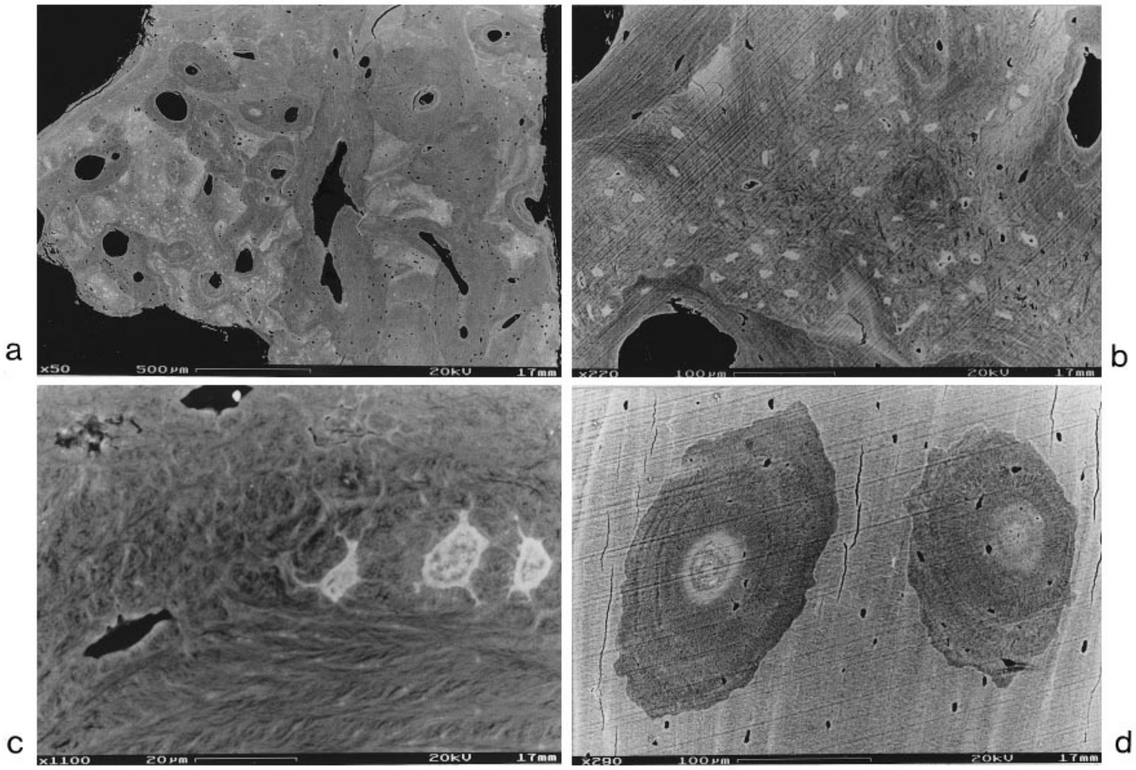

Figure 14 BSE-SEM showing mineralized lacunae, mineralized canaliculi and mineralized pearls in the lacunae in human mandible cortex. d) Mineralized Haversian canals (Kingsmill & A. Boyde, 1998).

3.3 Atomic force microscopy

Atomic force microscopy (AFM) is a scanning probe imaging technique developed in the 1980s. Based on the interaction between a physical probe and the surface of the specimen, AFM provides an image representing the 3D surface profile. This method can reach spatial resolutions down to a few nanometers and comparing to SEM, it doesn't require special coating of the specimen or a vacuum environment. However, the field of view is limited to about 150×150 μm2, the maximum variation in height on the surface is restricted to 10-20 μm and it remains a 2D technique (Lin & Xu, 2010).

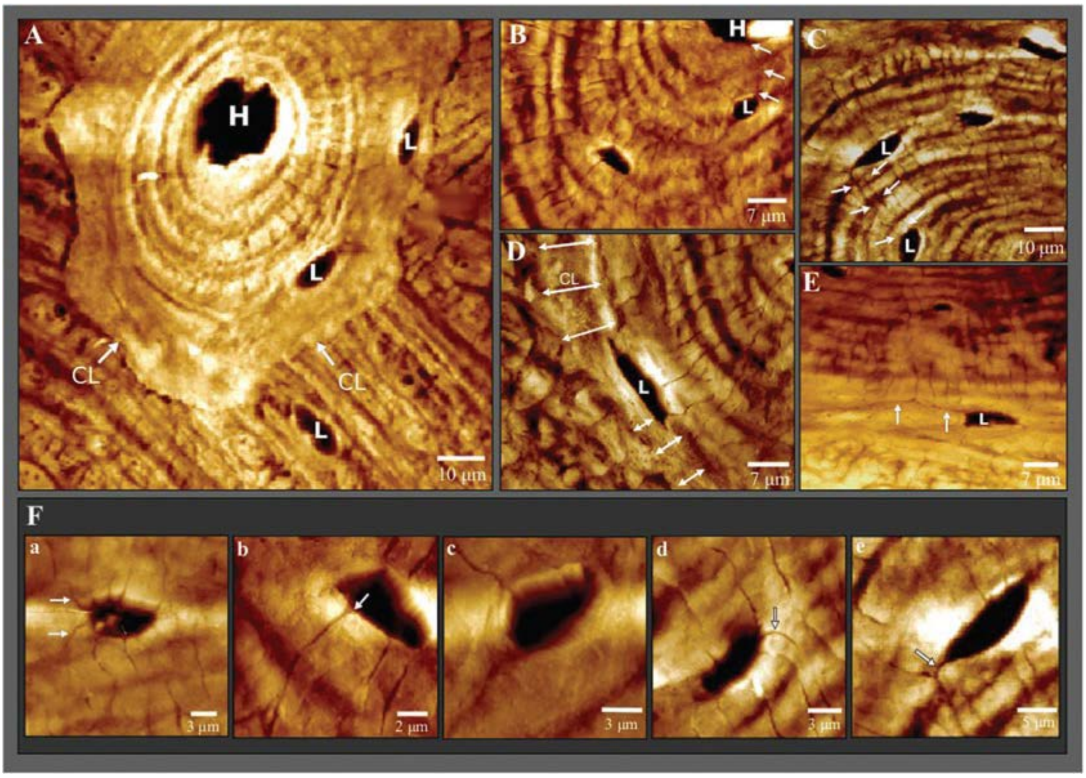

Figure 15 Atomic force microscopy shows the 3D surface profile exhibiting lacunae and canaliculi in mice cortical bone (Lin & Xu, 2010)

3.4 Focused Ion Beam - SEM

By using a high precision milling technique as focused ion beam combined with SEM, a cast coated sample of bone can be imaged in 3D. While it offers the possibility to obtain images in three dimensions, this method is destructive, tedious and the field of view is very restricted. The technique is characterized by anisotropic resolution which is higher in *xy* plane and lower in vertical plane. Stokes and Schneider used FIB-SEM to image the lacuno-canalicular network (Fig 16) (Stokes et al., 2005), (Schneider et al., 2011).

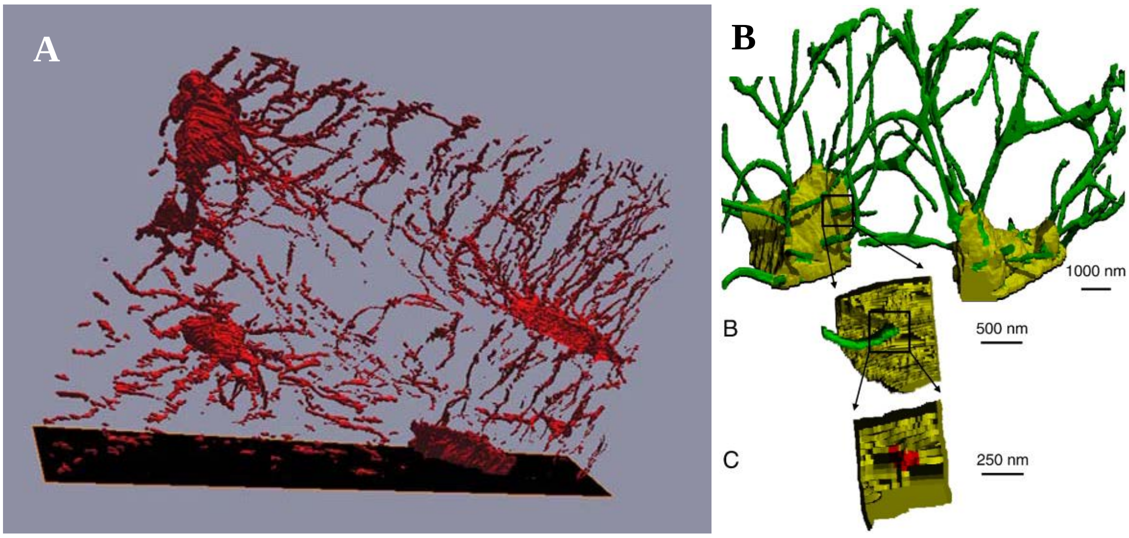

Figure 16 Three-dimensional images of the lacuno-canalicular network imaged with FIB-SEM. a) (Stokes et al., 2005), b) (Schneider et al., 2011)

3.5 X-ray based techniques

X-ray tomography is one of the most valuable techniques for investigations of the bone structure, especially at the microscale. Due to the high penetration power of X-rays, three dimensional images of considerably larger samples, comparing to alternative techniques, can be obtained.

X-ray microtomography

The advantages of the technique combined with the advances of the bone research toward finer scale, stimulated the demand for instruments. This motivated the development of commercial systems for X-ray tomography at the microscale. Several companies like SkyScan, XRadia and Scanco produce and continue developing desktop tomography instruments.

Recently, nominal spatial resolutions under one micron have been reached. This enabled the conduct of a small number of studies on osteocyte lacunae (Figure 17) (Vatsa et al., 2008) (van Hove et al., 2009). However, due to the insufficient photon flux, polychromatic beam, and limitations of the detectors, the image quality at high resolution is poor and imaging of canaliculi is not yet possible.

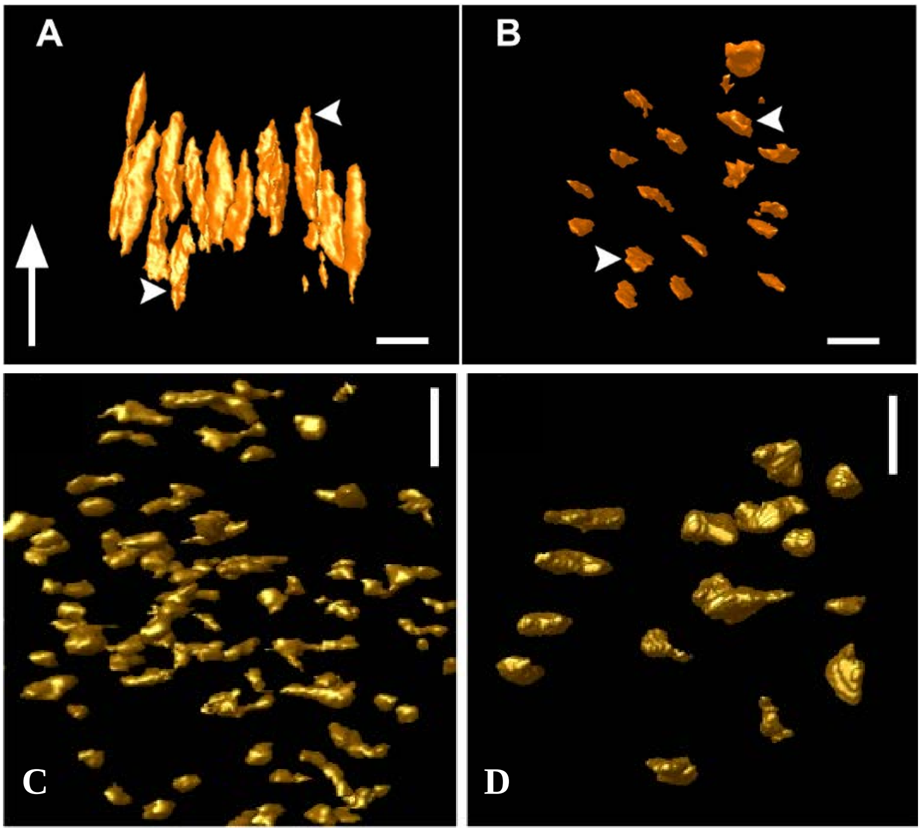

Figure 17 Desktop X-ray Computed Tomography a, b) 3D rendering of lacunae in mouse fibula imaged with SkyScan (Vatsa, Bone, 2008). Pixel size was 390 nm, energy 25 kV. c,d) Lacunae in osteoarthritic and osteopenic human bone, imaged with SkyScan 2011. Pixel size was 580 nm, X-ray voltage was 25 kV (van Hove, 2009). Scale bars are 15 µm.

Transmission X-ray microscopy

Transmission X-ray microscopes (TXM) make use of the different X-ray absorption of specific atoms, to create an image from the beam transmitted through the sample. Usually soft X-rays are used and the attainable spatial resolutions are in a range bridging the one of optical microscopy and the one of electron microscopy.

Andrews et al. used hard X-rays produced by a synchrotron source to image trabecular bone from mice, with TXM (Figure 18). The X-ray beam is focused onto the sample with a capillary condenser. The transmitted divergent beam is captured by a micro-zone plate lens and directed onto a transmission detector equipped with a scintillator and a Charge Coupled Device (CCD) camera. The beam energy was 5.4 keV, the spatial resolution was 40 nm and the FOV was 14×14 µm. The sample thickness was close to 50 µm (Andrews et al., 2010). The scan duration was about 24 hours.

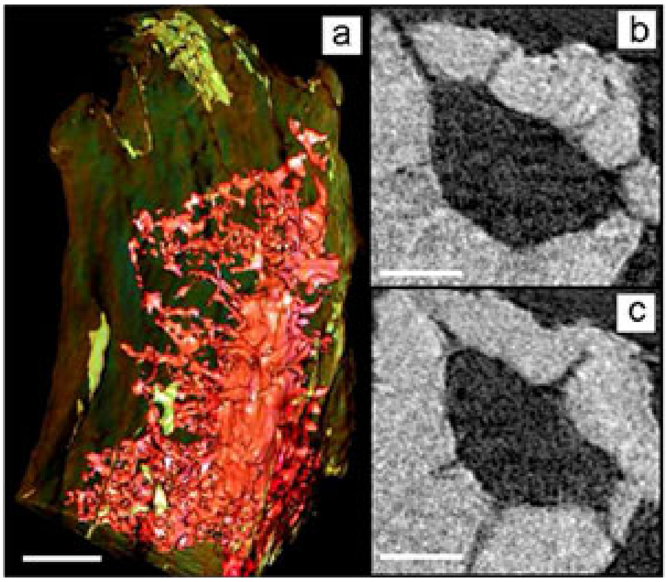

Figure 18 Transmission X-ray microscopy a) 3D rendering of a lacuna with canaliculi in a trabecula from mouse tibia. Scale bar is 5µm b,c) Slices from the image reconstructed with filtered backprojection. Scale bar is 2 µm. Sample thickness was 50 µm. (Andrews et al., 2010)

Ptychography

Ptychography is a scanning imaging technique using a pinhole. The principle was introduced in the 1970s for electron microscopy (Hoppe, 1974) (Hoppe, 1982) and further developed by Rodenburg (Plamann & Rodenburg, 1998) (Rodenburg, 2008). The technique makes use of redundant information from overlapping exposures to solve the diffraction-pattern phase problem. Hoppe also proposed to use the filtered backprojection method to obtain a 3D image of the sample from images recorded at multiple angles of rotation.

Dierolf et al. used ptychography with X-rays generated with a synchrotron source, to image cortical bone tissue (Figure 19) (Dierolf et al., 2010). The sample was illuminated through a small hole in a raster pattern with a narrow, coherent X-ray beam. For each point, a far field image of the diffraction pattern was recorded with a large area CCD detector. The method aims to solve the diffraction pattern phase problem by interfering adjacent Bragg reflections coherently and determining their relative phase.

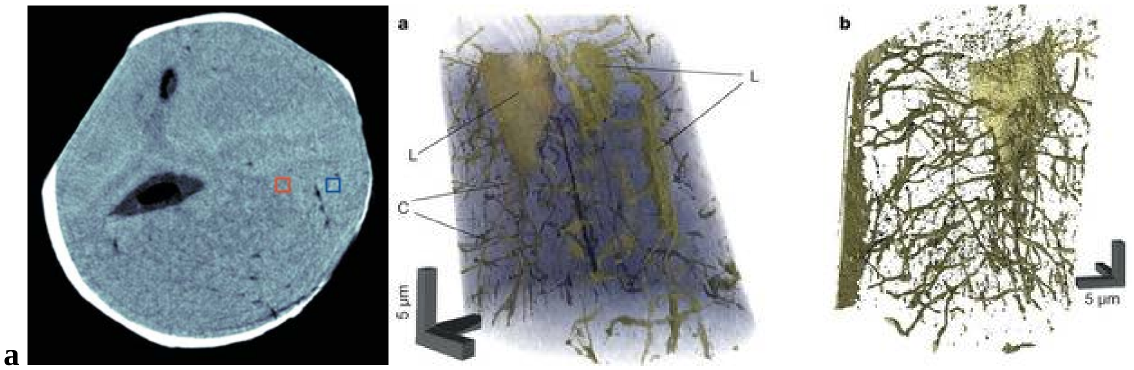

Figure 19 Ptychography a) Reconstructed slice of a cortical bone sample from mice femoral diaphysis. The spatial resolution was 65 nm and the volume of view was ~ 40×40×32 µm. b) Volume renderings of the scanned sample (Dierolf et al., 2010).

By reconstructing phase maps of the object at different rotation angles, a 3D image can be obtained using filtered backprojection computed tomography reconstruction. This image is a map of the real part of the refractive index δ (see section 4.3).

Depending on their thickness, samples usually shift the phase by more than 2π, generating a phenomenon called phase wrapping. This causes discontinuities when mapping the measurable quantity to a phase, which is limited to an interval spanning 2π. The spatial resolution is limited, among others, by radiation damage and imprecision in the relative positioning of pinhole and sample.

In (Dierolf et al., 2010) the sample was made vacuum compatible and a cylindrical specimen (~25 µm in diameter, ~35 µm in height) was prepared with focused ion beam milling. The 3D image of the sample was reconstructed with a spatial resolution of ~65 nm. The imaged volume contained 1-3 lacunae of which canaliculi were revealed. The beam energy was 6.2 keV, 181 projections were collected by recording 704 diffraction patterns per projection, with 1 s exposure time each. The total scan duration was about 40 hours.

Synchrotron X-ray microtomography

Due to the very high intensity of the produced beam, compared to a lab X-ray source, synchrotron radiation X-ray tomography gives access to superior image quality, permits higher resolutions to be attained, and a monochromatic beam can be selected in order to perform quantitative imaging. Additional information about the technique is presented in section 4.

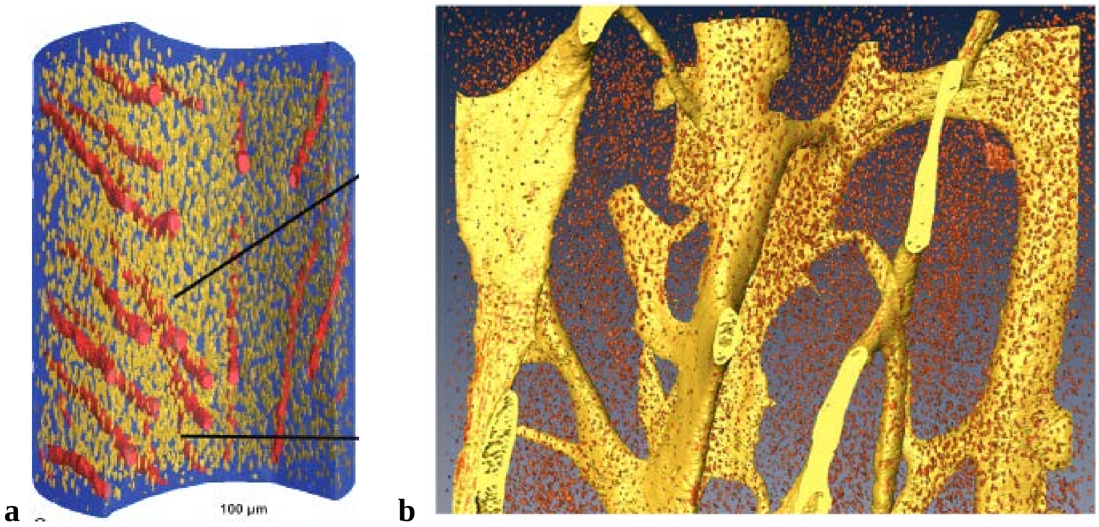

Figure 20 Synchrotron micro-CT a) Mice bone, 17.5 keV, 700 nm (Schneider, 2007, JBMR) b) Human cortical bone, spatial resolution 1.47 µm, energy 26.4 keV. (Hannah et al., 2010).

Synchrotron radiation X-ray tomography (SR-CT) has been extensively used to quantify simultaneously bone micro-architecture and mineralization at the micrometric scale (Nuzzo et al., 2002) (Bossy, et al., 2004) (Bousson et al., 2004) (Raum et al., 2006) (Granke et al., 2011).

A few studies have been reported on the osteocyte lacunae, at spatial resolutions of 0.7 µm in mice bone (Figure 20a) (Schneider et al., 2007) and 1.4 µm in human bone (Figure 20b) (Hannah et al., 2010) (Aymeric Larrue et al., 2011). However, imaging of canaliculi has not been achieved and imaging of the lacuno-canalicular network with SR X-ray CT was recently reported as been currently unattainable (Schneider et al., 2010).

3.6 Conclusions for this section

A rather wide variety of techniques have been used to image the osteocyte network. Most of these methods provide 2D images of thin slices or of the sample surface. Given the 3D nature of the LCN and its characteristic density and complexity, accurate measurements are difficult to obtain. Usually the in-depth information appears as overlapping in the image, making the separation of individual canaliculi unfeasible. Moreover, it is usually necessary to employ multiple techniques to obtain enough information on the tissue, in order to overcome the limitations of each one of them (Figure 21). Imaging the same region with different methods is not at all trivial, since specialized and modifying sample preparations are required for each technique.

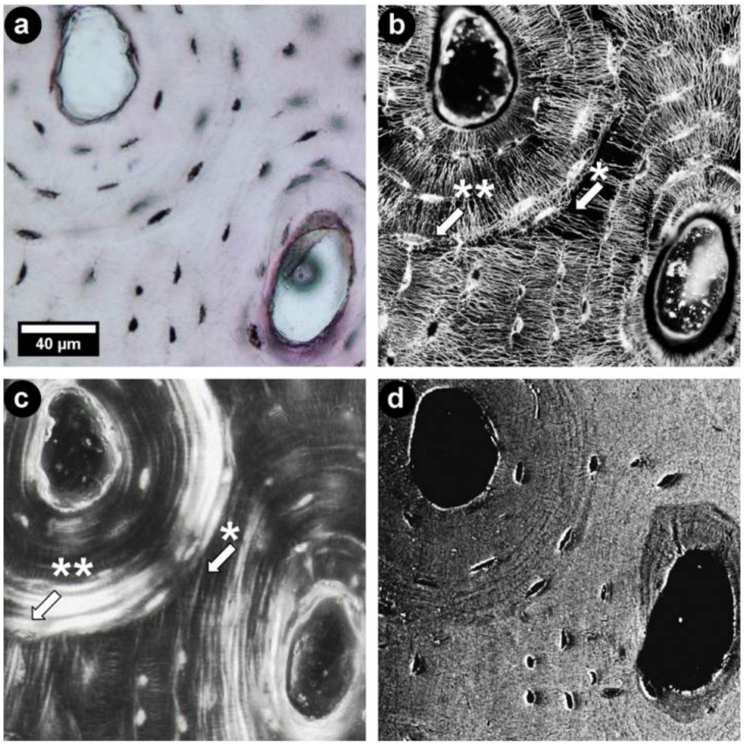

Figure 21 Figure Multiple imaging techniques are required to obtain complementary information a) Rhodamine stained sample under light microscope; (b) visualized with confocal microscopy c) polarized microscopy d) back- scattered electron microscopy image (Kerschnitzki et al., 2011)

The 3D parameters inferred from 2D measurements are biased and, obtaining quantitative results on representative samples from a specimen, usually implies a lot of manual tedious work. A few 3D imaging methods have been employed recently to assess the lacuno-canalicular network. While these methods provide direct access to 3D data, they can not yield sufficient information for biomedical studies. This is due mainly to limitations in terms of field of view (2-3 cells), added to tedious or destructive sample preparation and very long acquisition duration.

Synchrotron radiation computed tomography at micro and nano scale has the potential to yield information on both the morphology and the composition of the bone tissue, in 3D, with a relatively large volume of view.

Chapter 4

Synchrotron tomography at micro and nanoscale

X-ray microtomography was developed in the 1980s (Elliott & Dover, 1982) and, with the evolution of synchrotron sources, it extended to parallel beam three-dimensional imaging, reaching spatial resolutions down to a few micrometers (Flannery et al., 1987) (Bonse & Busch, 1996) (Salome et al., 1999). By using a two-dimensional detector in parallel beam geometry, an exact 3D reconstruction of the X-ray absorption coefficient within the object, can be obtained in a short time. These advances proved to have a great impact on the evolution of research in various domains such as biomedicine (Nuzzo et al., 2002) and materials science (Maire et al., 2001). The technique has been constantly improved, endeavoring nowadays to achieve imaging at the nanoscale.

4.1 Synchrotron radiation

Synchrotron light is electromagnetic radiation produced when charged particles are deviated from a circular trajectory, by magnetic fields. After being accelerated, the high energy electrons or positrons circulate in a storage ring with a constant speed, which is close to the speed of light. Compared to the conventional X-ray sources, synchrotrons can generate a beam up to 10^{12} times brighter (Figure 22).

Synchrotron radiation was first observed in the 1940s (Elder et al., 1947) and produced in the 1960s by the bending magnets of accelerators built for high energy nuclear physics research. At that time it was considered an undesired, secondary effect. In the 1970s it has been realized that synchrotron radiation can be used as a versatile and highly intense source of X-rays (Als-Nielsen & McMorrow, 2011). Dedicated storage rings and associated instrumentation with improved performance characteristics were then constructed all around the world.

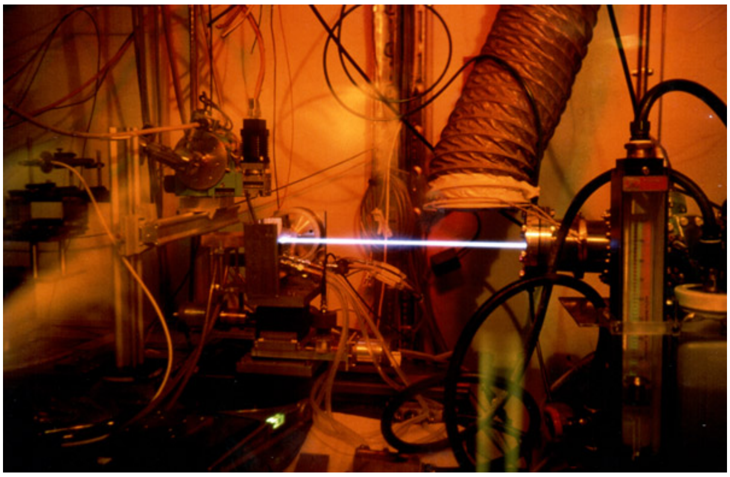

Figure 22 White X-ray beam extracted from a wiggler at ID11, ESRF. The intensity is sufficiently high to ionize the air. Note that this is just a demonstrative situation, during the experiments this phenomenon does not usually appear. Image credits: Åke Kvick, ESRF.

Nowadays, more than 50 synchrotron facilities are available in the world and they keep expanding (Bilderback et al., 2005). The largest synchrotron light sources today are the European Synchrotron Radiation Facility (ESRF) in France (6 GeV), the Advanced Photon Source (APS), in the USA (7 GeV) and Spring-8 in Japan (8 GeV).

ESRF is a third generation synchrotron radiation source producing an electron beam of 6 GeV, with a current of 200 mA (Bilderback et al., 2005). At ESRF, electrons are emitted by an electron gun, packed in "bunches" and first accelerated to nearly the speed of light by a pulsed electric field inside a vacuum, in a linear accelerator called Linac. To reach the final energy of 6 GeV, the electrons pass through a 300 meter long booster accelerator (Figure 23). The booster synchrotron contains accelerating radio frequency cavities and bending magnets, which force the electrons to deviate from a linear trajectory. The strength of the magnetic field must be increased and synchronized to the increasing energy of the electrons, which is why the accelerator is called a synchrotron.

Subsequently electrons are sent to the storage ring (844 m circumference), where they circulate with a constant speed. The beam harvested by the beamlines located tangentially to the storage ring, is generated by bending magnets or by multipole insertion devices such as undulators and wigglers. These are periodic magnetic structures which create a sinusoidal magnetic field, perpendicular to the direction of propagation of the electron.

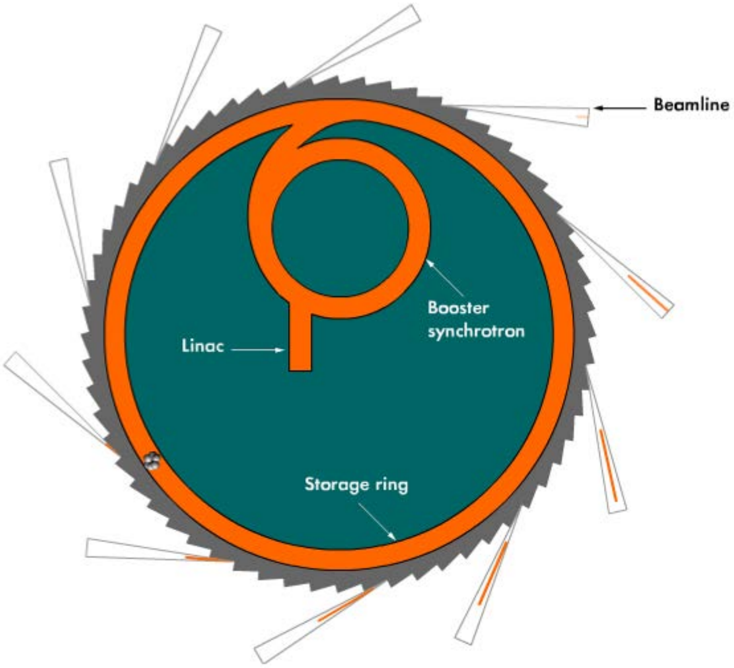

Figure 23 At ESRF electrons are first accelerated in a linear accelerator (Linac) , followed by acceleration in a booster synchrotron. Subsequently they circulate with a constant speed in a storage ring from where the synchrotron light is generated through insertion devices. Image credits: ESRF.

4.2 Imaging system at the ID19 beamline

At the ID19 experimental station, the hutch is located at ~ 145 m from the source permitting to obtain a parallel beam tomographic setup. The beam is delivered by an wiggler and two undulators. A single wavelength beam can be selected with one of the two monochromators. The detector is mounted on a translation stage permitting to vary the distance between the sample and the detector. Very high precision motors are used to align the sample with the beam and for the sample rotation during tomographic scans. The entire pipeline of instruments is controlled remotely, permitting to set various image acquisition setups. The commands are unified under a single software package called SPEC (UNIX-based program from Certified Scientific Software).

Figure 24 illustrates the design of a typical imaging beamline at a synchrotron. The beam conditioning optics hutch is separated from the experimental hutch, where the sample stage and the detector are located. Note that ID19 has the particularity of being a long beamline, the actual distances with respect to the source are described in Figure 25.

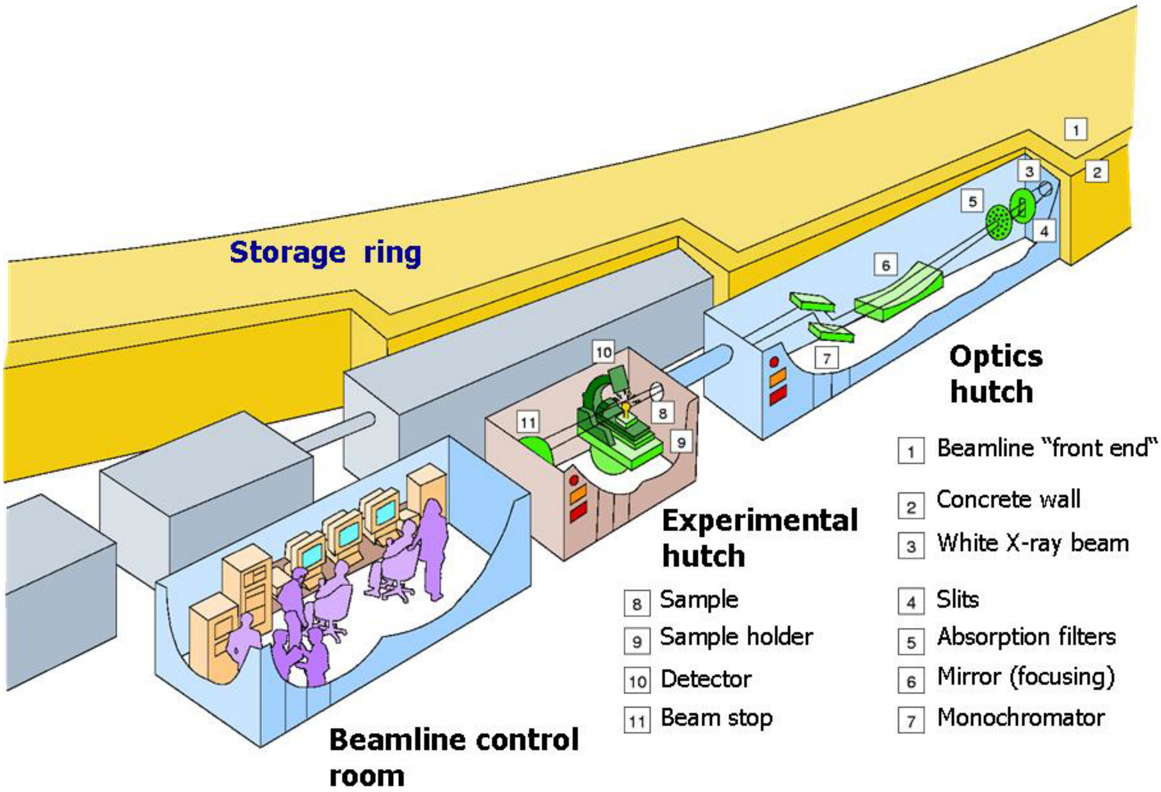

Figure 24 Design of a typical beamline at a synchrotron facility. Dedicated hutches are built for the instruments preparing the beam and for the sample and detector stages. The beamline is controlled remotely from the control room. Image credits: Timm Weitkamp, Soleil.

Insertion devices

At ID19 the beam is generated with multipole insertion devices. By imposing to the electrons a trajectory different from a circular arc, the flux and brilliance of the beam can be greatly increased. This is obtained with a spatially periodic magnetic field given by permanent magnets. Each wiggle of an oscillating charged particle determines radiation emission. The contributions of the different wiggles add up incoherently in the case of a wiggler and coherently in the case of an undulator.

Wigglers give higher photon energies, more photon flux and a continuous spectrum. The undulators yield brighter beam, with a smaller spot size, which is partially coherent. The spectrum of the undulator is constituted of multiple narrow band peaks. The spectral bandwidth ($\Delta\lambda/\lambda$) corresponding to a harmonic m, can be estimated as function of the number of periods N_{os} of the undulator (P. Cloetens, 1999):

$$\Delta\lambda / \lambda = 1 / m N_{os} \qquad (1)$$

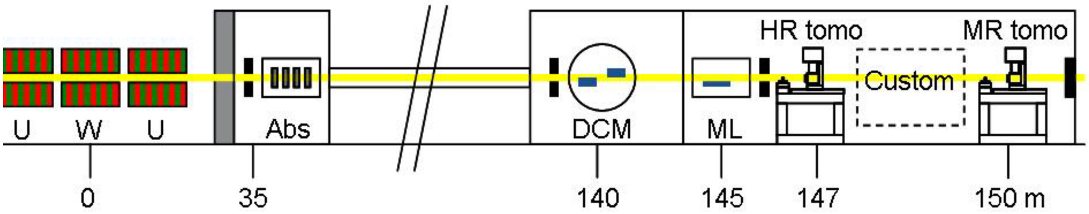

Figure 25 Main elements of ID19 with distances from the source. U: undulator; W: wiggler; OH1: Optics Hutch 1; Abs: attenuators; OH2: Optics Hutch 2; DCM: double-crystal monochromator; EH: Experimental Hutch; ML: multilayer; HR tomo: high-resolution tomograph; MR tomo: medium- resolution tomograph. Image from (Weitkamp et al., 2010).

The magnetic field is tuned by changing the gap between the upper and lower arrays of magnets through a high resolution, high strength mechanical structure. Two undulators are currently installed at ID19. One of them yields a particular spectrum, with a single narrow peak, which permits to use a quasi-monochromatic beam without introducing a monochromator. More information about the undulators is presented in Chapter 5.

The beamline is separated from the vacuum of the storage ring through a beryllium window which has low absorption for hard X-rays, but not in the soft part of the spectrum. The window is protected by a diamond filter which prevents overheating. Various attenuators can be introduced in the beam before being monochromatized, with the aim to absorb low energies which can not be handled by the monochromator.

Monochromators

Two monochromators installed on the beamline permit the selection of a single energy from the white beam: a water-cooled double-crystal monochromator (DCM) with two silicon-111 crystals in Bragg geometry ($\Delta E/E \approx 1.4\cdot10^{-4}$), and a single-bounce, upward-reflecting multilayer (ML) monochromator ($\Delta E/E \approx 2\cdot10^{-2}$). The ML has three strips with different material composition and multilayer period (10 mm wide W/B4C, period d=2.46 nm; 15 mm wide Ru/B4C, period d=2.46 nm and 10 mm wide Ru/B4C, period d=3.91 nm), deposited for different ranges of photon energy. For the high spatial resolution experiments, we used the multilayer monochromator because it permits a gain of two orders of magnitude in beam intensity. This is in the detriment of the beam width and height (reduced to ~ 10 mm×4 mm), but this is not a limiting factor at high resolution, given the size of the field of view (~ 0.6 mm×0.6 mm with a 280 nm pixel size).

Detector

The detector is composed of a scintillation screen, a reflecting mirror, a magnifying optic system and a Charge Coupled Device (CCD) camera (Figure 34, Supp Figure 70).

The scintillator is an important element of the detector. It has the property to absorb the energy of an incident ionizing radiation and reemit this energy in the form of light situated in the visible range. The desirable properties of a scintillator are a high efficiency for converting the energy of incident radiation into scintillation photons, transparency to its own scintillation light, resistance to radiation damage and high temperature tolerance. The light output is the most important, as it affects both the efficiency and the resolution of the detector. The efficiency is the ratio of detected particles to the total number of particles impinging upon the detector. The energy resolution is the full width of distribution, measured at half of its maximum (FWHM), divided by the number of peak channel. The emission spectrum is the relative number of photons emitted by scintillator as a function of wavelength (Martin & Koch, 2006) (Martin et al., 2009) (Douissard et al., 2010). Figure 26 shows the absorption curves as function of the energy, for two scintillators used during the experiments.

The linearity of the response of the detector with the incident intensity is a prerequisite for quantitative imaging. Correction for non-linearities (off-set, non-uniformity) is made in the flat-field correction. The spatial resolution of the detector is described by the optical transfer function. It is measured through the edge spread function which can be obtained with an absorbing edge. The detective quantum efficiency (DQE) describes how well the detector preserves the signal to noise ratio (SNR) present in the incident photons. A large DQE reduces the necessary dose and exposure time to achieve a given SNR and resolution in the recorded images.

CCD cameras are normally linear before saturation when the full well capacity is reached. The linearity errors are smaller than ± 0.3 % for the cameras used (Labiche et al., 2007). The gain is not necessarily identical for every pixel. This fixed sensitivity pattern gives a multiplicative contribution to the image. It is exactly corrected for by dividing the image signal with an image I^{flat} obtained under uniform illumination of the detector. An output signal is present without incoming photons, corresponding to the time dependent dark current of the CCD and an electronic off-set. This is an additive contribution. A dark image I^{dark}, recorded without incoming beam, is subtracted from every image. Both contributions are corrected for with the flat field procedure:

$$I_d^{corr}(x) = \frac{I_d^{rec}(x) - I^{dark}(x)}{I^{flat}(x) - I^{dark}(x)} \qquad (2)$$

In order not to increase the noise with this correction, a number of dark images, about 20, are averaged.

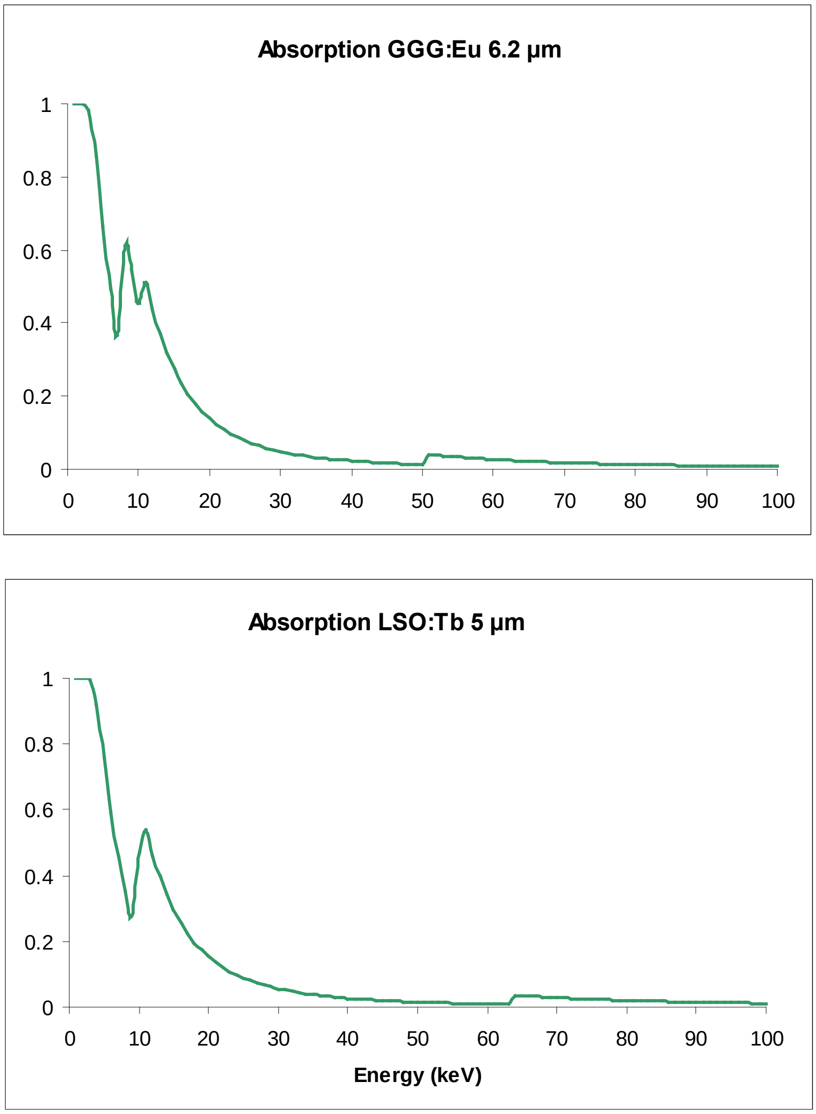

Figure 26 The absorption curves of two of the employed scintillators as function of beam energy.

The noise is function of the number of photons (photonic noise) (Flannery et al., 1987):

$$N_{Phot} \propto \left(\frac{D}{\Delta x}\right)^4 \frac{\exp(\mu D)}{[\mu D(\sigma/\mu)]^2} \qquad \text{where} \quad \frac{\sigma}{\mu} = \frac{1}{SNR} \qquad (3)$$

where N_{Phot} is the number of photons, Δx is the spatial resolution, D is the sample diameter, μ is the X-ray attenuation coefficient and SNR is the signal to noise ratio. Therefore, for a given sample $S(\mu,D)$ and constant SNR, an increase in spatial resolution by a factor two requires an increase in number of photons by a factor 2^4. Consequently, images with high spatial resolution and good SNR can be obtained by long integration time or high photon flux.

4.3 Interaction X-ray and matter

X-rays are electromagnetic radiation with wavelengths in the range 10^{-2} to 10 nm, firstly produced and detected by Röntgen in 1895. An X-ray beam traversing an object can be affected in two ways. It can be attenuated, hence its amplitude changes, or it can be retarded by the object, resulting in a phase shift. These effects can be described by the complex refractive index n:

$$n = 1 - \delta_n + i\beta \qquad (4)$$

where the real part δ_n is the refractive index decrement, related to the phase shift and the imaginary part β is the absorption index.

X-ray attenuation

In the range of hard X-rays there are three main processes contributing to the attenuation of the beam. These are the photoelectric effect and Rayleigh (elastic) and Compton (inelastic) scattering.

The photoelectric effect is responsible for the absorption of X rays and it is the dominant process for energies in the range we are concerned with (8 keV – 100 keV). This describes the interaction between an incoming photon, with a characteristic energy E, and a bound atomic electron, resulting in the complete absorption of the photon.

Rayleigh scattering refers to the deviation of photons from their trajectory due to collision with the electrons in the object. In this case the scattering is elastic that is, the photons keep their initial energy. The contribution of this process to the X-ray beam attenuation is minor.

The Compton effects describes the inelastic scattering of photons. Here the interaction between a photon and an electron results in scattering of the photon with a modified energy, while the electron recoils determining the ionization of the atom.

The attenuation projections through the object, recorded during imaging, correspond to the total contribution of these processes, given by the *linear attenuation coefficient* μ. This can be evaluated as:

$$\mu = \frac{N_A \rho \sigma_{tot}}{A} \qquad (5)$$

Where N_A is Avogadro's number, ρ is the density of the material, A is the atomic mass number and σ_{tot} is the total cross section of the interaction mechanisms described above. The total cross section is the sum of the individual cross sections, which are measures of the likelihood of occurrence of each process. The attenuation coefficient is related to the absorption index of the complex refractive index β and to the wavelength λ as follows:

$$\mu = \frac{4\pi}{\lambda}\beta \qquad (6)$$

The attenuation coefficient is proportional with the tissue degree of mineralization (Nuzzo et al., 2002).

The Beer-Lambert law

The relation between the intensity of the incident beam, the linear attenuation coefficient and the intensity of the beam leaving the object, is established by the Beer-Lambert law. This states that the number of photons traversing an object diminishes exponentially, as function of the material's attenuation coefficient and of the path length. The intensity I of a monochromatic beam traversing a homogenous object characterized by μ, decreases exponentially with the sample thickness d:

$$I = I_0 \exp(-\mu d) \qquad (7)$$

where I_0 stands for the intensity of the incident beam and μ is the linear attenuation coefficient at a given energy E.

The expression can be extended for heterogeneous objects by considering infinitesimal homogeneous sections of the object:

$$I = I_0 \exp\left(- \int_D \mu(x,y) ds \right) \qquad (8)$$

where D is a straight line modeling the X-ray path.

Propagation-based phase contrast

A wave traversing an object is retarded in accord with the electron density of the material, introducing a phase modification. The phase shift of the X-rays is described by the refractive index decrement δ_n. The dependence of β and δ_n on energy E and atomic number Z can be approximated as (Wang, 2007):

$$\beta \propto \frac{Z^5}{E^{4.5}}, \qquad \delta_n \propto \frac{Z}{E^2} \qquad (9)$$

At energies above 10 keV, the refractive index decrement is much bigger than the absorption index. Figure 27 shows the ratio between these two indexes depending on the energy for the element aluminum, which has an attenuation coefficient similar to the one of compact bone tissue. One can observe that in the range of hard X-rays, the beam is up to three orders of magnitude more sensitive to phase shifts than to attenuation. For this reason, using phase contrast for imaging is very attractive.

The refractive index decrement is also proportional with the square of the wavelength λ^2, and with the mass density of the material ρ (Guinier, 1994):

$$\delta_n \approx 1.3 \times 10^{-6} \rho \lambda^2 \qquad (10)$$

with ρ in g/cm^3 and λ in Å.

This relation shows that the quantity reconstructed in phase imaging corresponds to the electron density, which is approximately the mass density of the material.

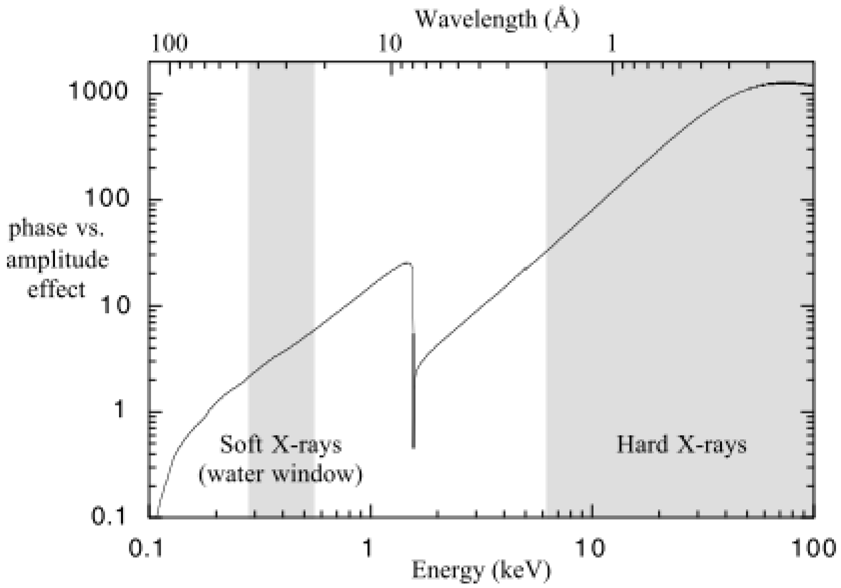

Figure 27 Ratio of the effect on the phase and the amplitude of a transmitted wave as a function of the X-ray energy, for the element aluminium. (Cloetens, 1999)

There are several methods developed for visualization of the phase with hard X-rays, such as grating interferometry (Bonse & Hart, 1965), (C. David et al., 2002), (Momose, 2003), (Weitkamp et al., 2005), (Pfeiffer et al., 2006), analyzer based methods (Ingal & Beliaevskaya, 1995) (Chapman et al., 1997) and methods based on free-space propagation (Snigirev et al., 1995), (S. W. Wilkins et al., 1996), (Cloetens et al., 1999), (Jean Pierre Guigay et al., 2007), (M. Langer et al., 2010). The simplest technique in terms of experimental setup is based on *free space propagation*, or Fresnel diffraction. As opposed to the methods relying on gratings or on analyzer, this method permits to achieve very high spatial resolution.

In the case of free space propagation, the contrast appears due to interference between parts of the wavefront that have been slightly deviated angularly, creating phase gradients. The overlap of parts of the wavefront occurs after propagation over a certain distance. In order to detect contrast, the second derivative of the phase needs to be different from zero, as while the phase gradient is constant, the overall beam is deflected. When the beam is tangent to the interface between two mediums in the object, a variation of the phase gradient takes place, generating contrast.

The amplitude and phase modulations introduced on the incident wave by the object can be described by a transmittance function $T(\mathbf{x})$:

$$u_0(\mathbf{x}) = T(\mathbf{x})u_{inc}(\mathbf{x}) \qquad (11)$$

where $u_{inc}(\mathbf{x})$ is the incident wave field, $u_0(\mathbf{x})$ the wave field at the exit plane of the object (*D=0*), **x**=*(x,y)* are the spatial coordinates in the plane perpendicular to the propagation direction z, and

$$T(\mathbf{x}) = A(\mathbf{x})\exp[i\varphi(\mathbf{x})] = \exp[-B(\mathbf{x})]\exp[i\varphi(\mathbf{x})] \qquad (12)$$

Both the attenuation and the phase shift induced by the object can be described as projections through the absorption and refractive index distributions respectively, with

$$B(\mathbf{x}) = \left(\frac{2\pi}{\lambda}\right)\int \beta(x,y,z)dz \qquad (13)$$

and

$$\varphi(\mathbf{x}) = -\left(\frac{2\pi}{\lambda}\right)\int \delta_n(x,y,z)dz \qquad (14)$$

Therefore, both the real and the complex part of the refractive index can be reconstructed by tomographic reconstruction if amplitude and phase can be measured for different angular positions of the sample.

The detected intensity $I_D(\mathbf{x})$ at a distance *D* downstream of the sample as function of the wave field is:

$$I_D(\mathbf{x}) = |u_D(\mathbf{x})|^2 \qquad (15)$$

and for the case of weak defocusing conditions it can be approximated as (Cloetens et al., 1997):

$$I_D(\mathbf{x}) = I_0(\mathbf{x})\exp\left[\frac{-\lambda D}{2\pi}\nabla^2\varphi(\mathbf{x})\right] \qquad (16)$$

The image acquisition, in the case of free propagation phase imaging, consists in recording angular projections of the object at several distances between the detector and the sample. From each set of projections corresponding to the same rotation angle, a phase map is calculated based on a phase retrieval algorithm.

These 2D phase projections are then used to generate a 3D image through computed tomography algorithms. The reconstructed image represents the sample's 3D refractive index distribution. If the tomographic reconstruction is performed directly on radiographs acquired at a longer distance from the sample, an edge-enhancement effect is obtained, which is proportional to the Laplacian of the refractive index.

The reconstructed 3D distribution in phase contrast tomography *g(x,y,z)* can be approximated as (P. Cloetens et al., 1997):

$$g(x,y,z) \approx \mu(x,y,z) + D\left(\frac{\partial^2}{\partial x^2}+\frac{\partial^2}{\partial y^2}+\frac{\partial^2}{\partial z^2}\right)\delta_n(x,y,z) \qquad (17)$$

where *D* is the distance downstream the sample, μ is the linear attenuation coefficient and δ_n is the 3D refractive index decrement distribution in the object.

The second term, containing the 3D Laplacian of the real part of the refractive index distribution, contributes to *g(x, y, z)* in regions of the object where there are strong variations in the refractive index, such as boundaries between different phases. The edge enhancement effect increases with the propagation distance. Phase contrast is always present in the images acquired at very high spatial resolution due to the relatively large propagation distance between the sample and the detector. This effect can permit to detect structures slightly smaller than the actual spatial resolution.

4.4 Image reconstruction

The three-dimensional images are obtained from a set of 2D angular radiographs recorded during sample rotation over 180º (Figure 28). For the case of parallel beam geometry setup, equipped with a two dimensional detector, the tomographic reconstruction is direct and exact.

The radiographs are preprocessed before being used to obtain transverse slices. The preprocessing consists in corrections for dark currents, for inhomogeneities in the beam and eventually for sample motion during the scan or ring artefacts. Figure 28 illustrates the process of tomographic acquisition for the case of parallel beam geometry.

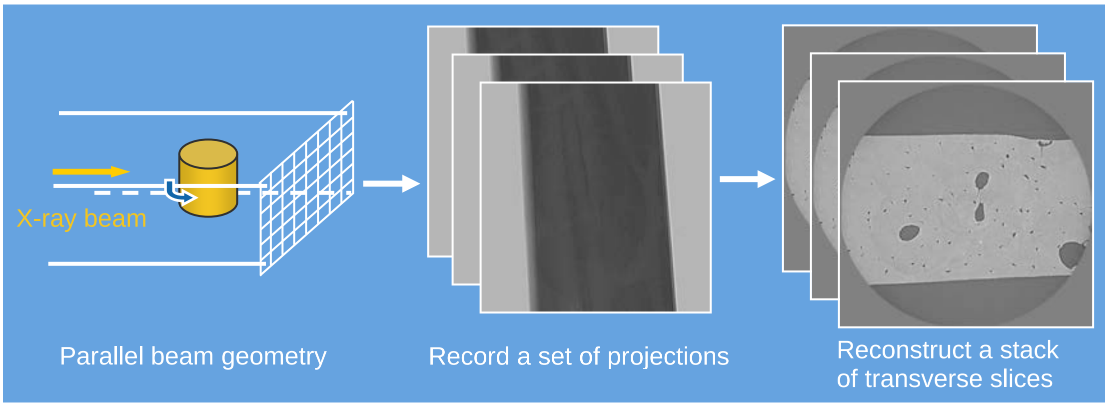

Figure 28 Tomographic reconstruction with a parallel geometry setup.

Tomography

The theoretical and experimental fundamentals of tomography (from Greek *tomos*-"slice" and *graphein*-"to write") have been established by Cormack and Hounsfield in the 1970s (Hounsfield, 1973) (Cormack, 1964). They were awarded the Nobel Prize for Physiology and Medicine in 1979. The mathematical support for the image reconstruction is attributed to the Radon transform which is the integral of a function over straight lines (Radon, 1917). By finding the inverse of the transform, a function can be retrieved from its line integrals.

It has been shown (Bracewell, R. N., 1956) (De Rosier & Klug, 1968) (Kak & Slaney, 1988) that the 1D Fourier transform of the line integral projection of a slice, at an angle theta, represents the line at the same angle theta, of the 2D Fourier transform of that slice (Figure 29). This means that by acquiring projections of the object at a set of angles covering 180º (symmetry), one can obtain the 2D Fourier transform of a slice. From this, the section can be reconstructed by inverse Fourier transform. However, this method relies on the conversion from the Fourier polar grid to Cartesian grid which is not trivial. The necessary interpolation step is susceptible to introduce artefacts.

A simplified method of reconstruction has been derived by (Ramachandran & Lakshminarayanan, 1971), based on deconvolution in the space domain. It can be demonstrated the image can be retrieved by back-projecting the set of angular projections, convolved with a filter *k(u)*.

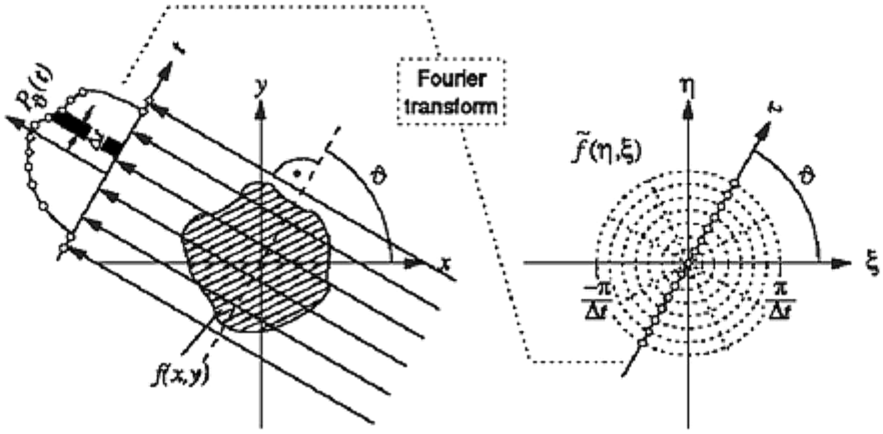

Figure 29 The Fourier slice theorem

Therefore, the 2D transverse image *f(x,y)* can be reconstructed by integrating the filtered projections $\tilde{p}_\theta(u)$ over the rotation angles:

$$f(x,y) = \frac{1}{2}\int_0^\pi \tilde{p}_\theta(x\cos\theta + y\sin\theta)d\theta \qquad (18)$$

where

$$\tilde{p}_\theta(u) = (p_\theta * k)(u) \qquad (19)$$

This algorithm is commonly known as the filtered backprojection (FBP) and it is widely used in various imaging domains.

Conversely to the cone beam geometry, in the case of parallel beam the transition from 2D to 3D is direct. This is due to the path of X-rays straight through the sample and perpendicular to the detector. Each raw of the detector yields an individual 2D reconstruction which can be used to create a 3D stack. For the standard case of cone beam geometry, the extension of the FBP is known as the Feldkamp algorithm. This is exact only in the central plane, the error introduced by the divergent path of the X-rays increasing with the distance from the center. In the case of parallel beam, this error does not exist, hence the reconstruction is exact.

Part B

Contributions

Chapter 5

Image acquisition

In this chapter we present our work related to the experimental part. Different strategies, parameters and instrumentation combinations, have been explored for data acquisition. The main results associated to this aspect of the thesis have been synthesized in a paper manuscript which is included in this chapter, following an introductive section.

Initially we introduce the specimens used for imaging the lacuno-canalicular network. Samples from one specimen have been cut in thin slices and imaged with synchrotron X-ray holography (Figure 30) and with confocal microscopy (Figure 31). Detailed information about the sample preparation is provided in the Materials and Methods section of the paper included in this chapter.

Subsequently we illustrate some of the main difficulties encountered in imaging the lacuno-canalicular network with synchrotron computed tomography (Figure 32). We tried to overcome one of these challenges, the damage induced by the radiation dose, by freezing the sample during the scan with cryogenic methods. Representative images for the results of these tests are shown in Figure 33.

In Figure 30 we show images of transverse sections in a sample, obtained with in-line holography (Gabor, 1949) (Cloetens et al., 1999), at ID19. The samples were thin slices (250 µm thick) cut transverse to the osteons, extracted from the specimen presented in Chapters 8 and 9. The pixel size was 300 nm giving a field of view of about 615×615 µm. In these images the Haversian systems can be distinguished and the lamellar aspect of the osteons can be observed. The reconstructed phase map Figure 30b (M. Langer et al., 2010) (Jean Pierre Guigay et al., 2007) yields the variations in mineral content with higher accuracy. By applying a high pass filter in the Fourier domain, the lamellar structure of the osteons becomes visible.

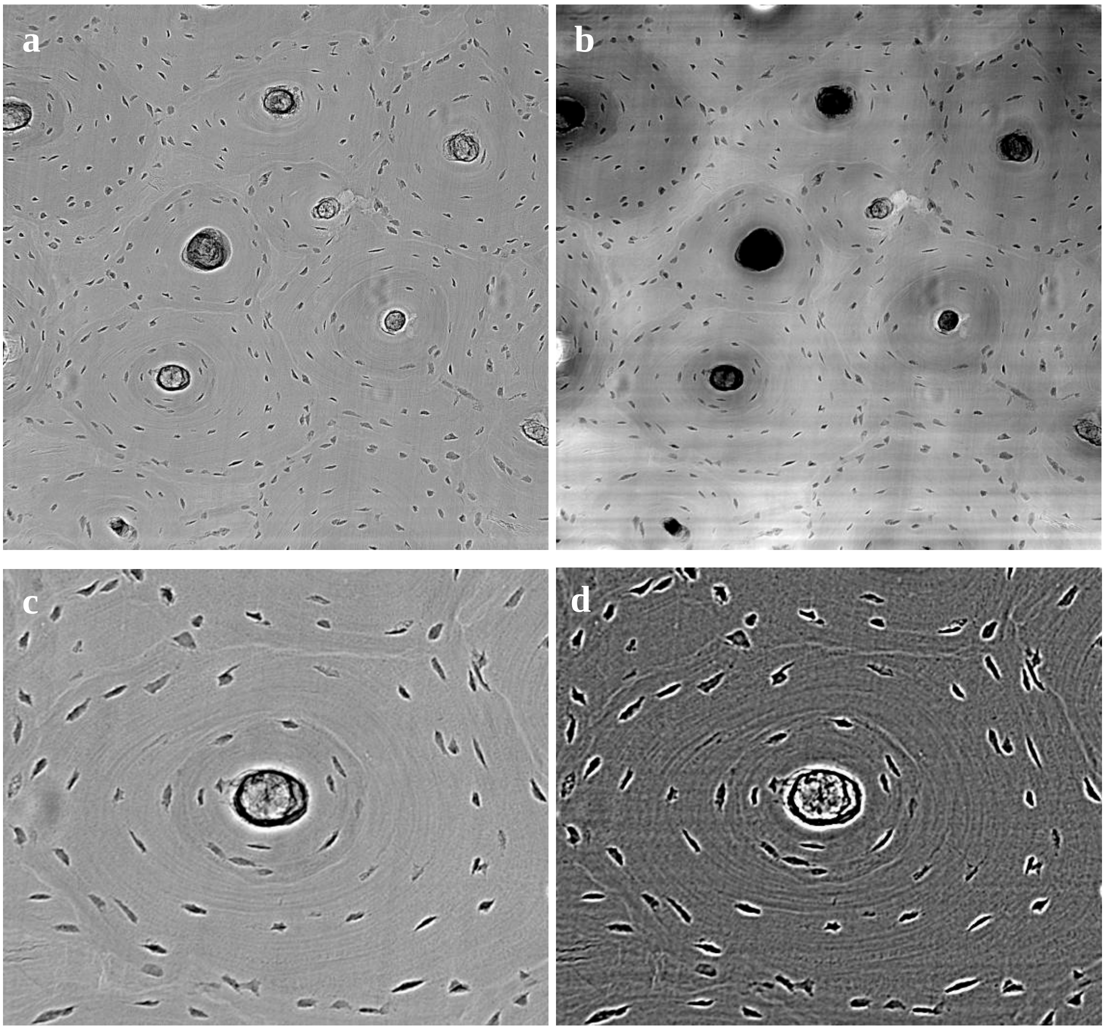

Figure 30 Transverse slices in a specimen acquired with in-line holography. a) Flat field corrected radiograph of a thin slice (250 µm thick) from extracted from the specimen presented in Chapters 8 and 9 (300 nm pixel size, energy ~ 18 keV). b) Phase retrieved from radiographs recorded at multiple distances between the sample and the detector. c) Magnified region form (a). d) Magnified region from (b), after high pass filtering.

Figure 31 shows images of a sample from the same specimen, obtained with confocal microscopy after staining with fluorescein isothiocyanate (FITC). The images were acquired at the Institute Albert Bonniot, Grenoble, with the kind permission and help of Alexei Grichine. The spatial resolution was 220×220 nm in plane and 500 nm in depth for the images in Figure 31 a,b, and 140×140 nm in plane and 300 nm in depth for the images in Figure 31 c,d. The in plane field of view covers 225×225 µm^2 and 71×71 µm^2 respectively in Figure 31 a,b and Figure 31 c,d. One can observe that the stain reveals the lamellae in the osteon.

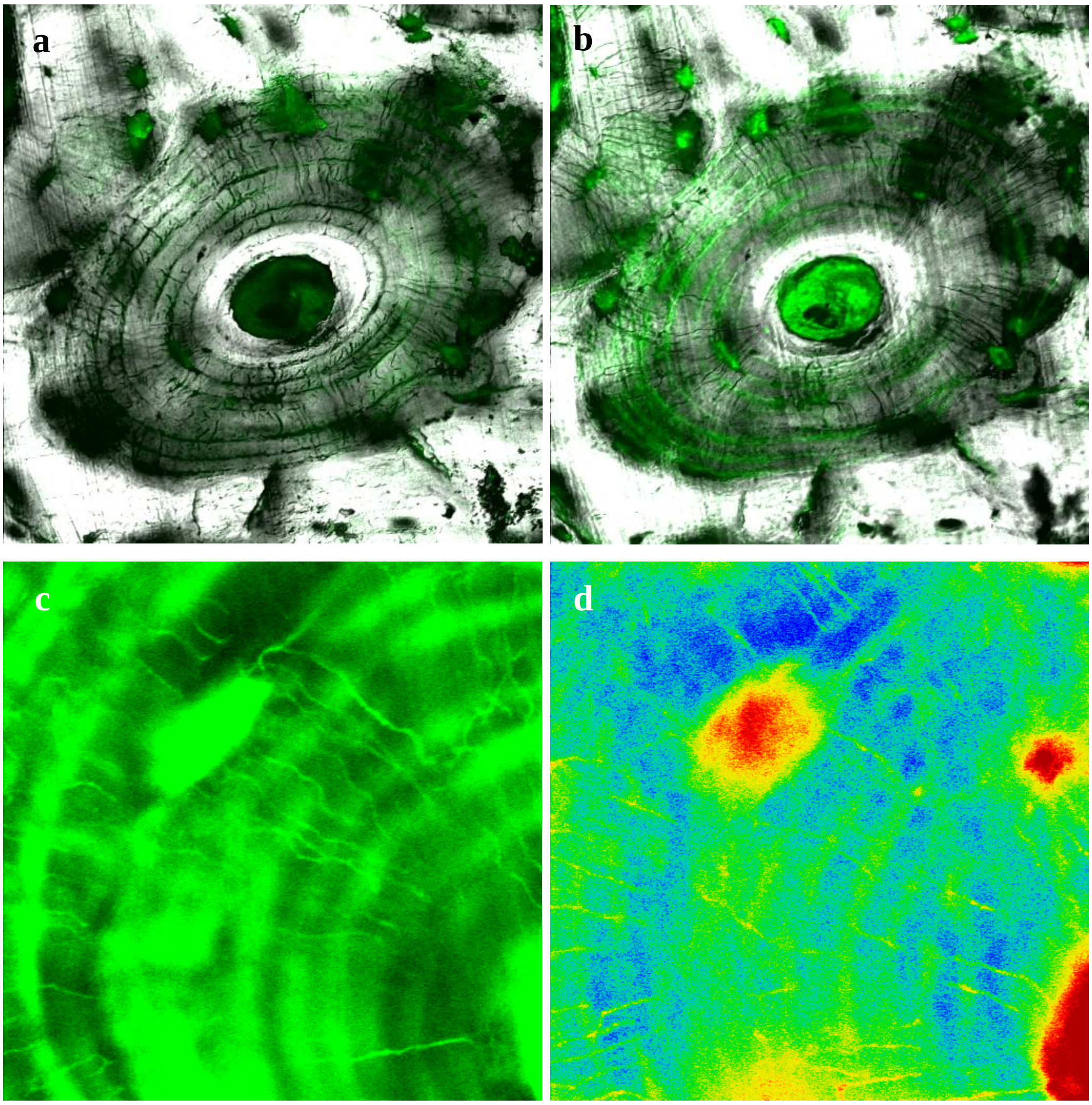

Figure 31 Images of the specimen from confocal microscopy a), b) felip218D_x20_z, (a) z = 0 µm (b) z = 3.5 µm; FOV 225µm x 225µm x 7.5µm (spatial resolution: 0.22µm x 0.22µm x 0.50µm) Stain is visible «between» lamellae. c), d) felip218D_x63_6, 71µm x 71µm x 17µm (0.14µm x 0.14µm x 0.30µm) (d) same as (c), with a different color map.

Figure 32 illustrates the problems we encountered during the exploratory experiments with SR-CT, aiming to achieve imaging of the lacuno-canalicular network in compact bone. The high level of radiation dose induces formation of micro-cracks in the specimen during the scan. This creates motion artefacts which, added to limitations in terms of spatial resolution, signal to noise ratio and level of contrast, make the detection of osteocyte canaliculi impossible.

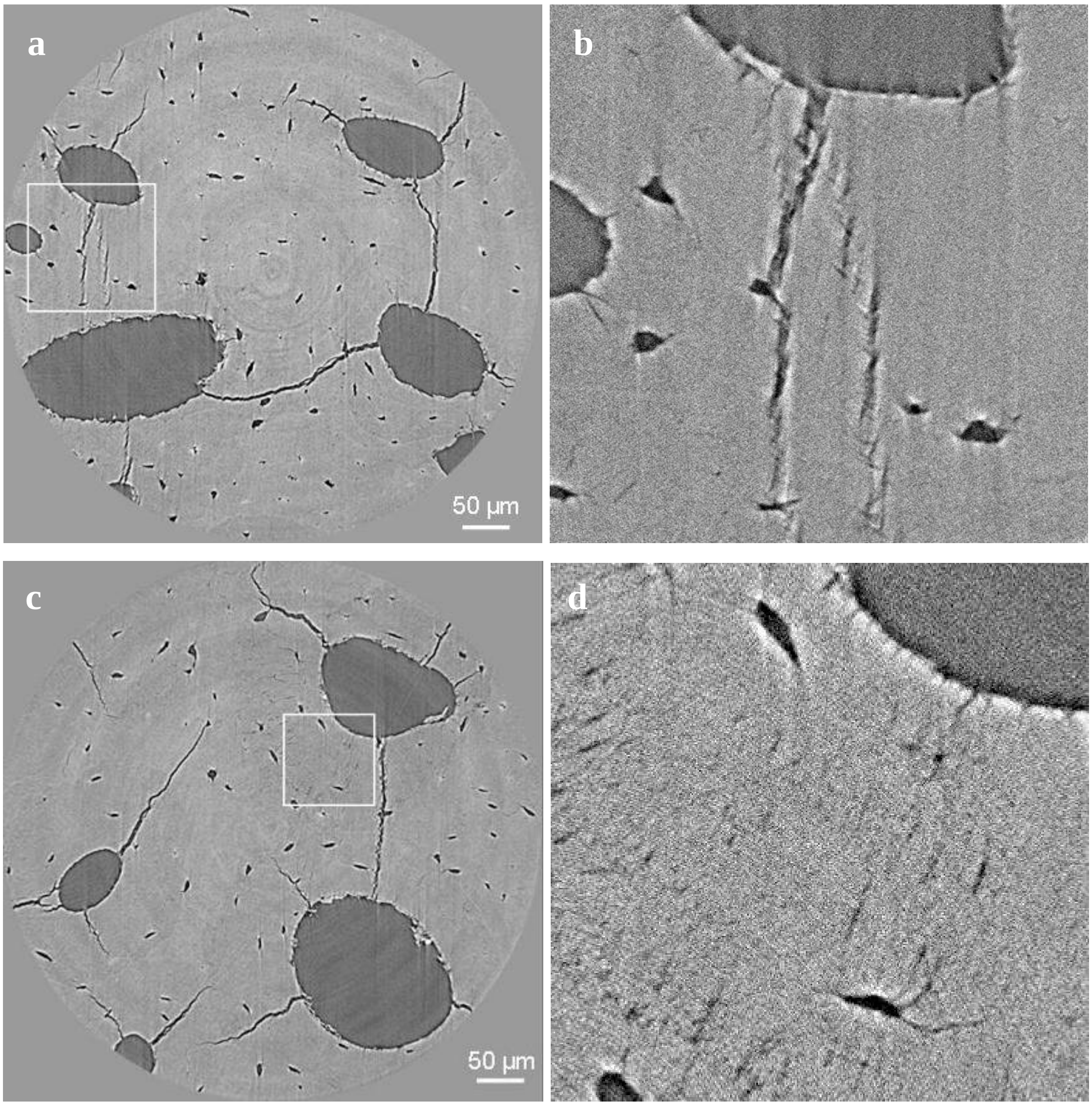

Figure 32 Slices in the reconstructed images showing micro-cracks (a) (b) (c) generated due to high radiation dose. These induced damages are the source of motion artefacts in the reconstructed images. Additionaly, images are affected by noise, limited spatial resolution, low contrast and partial volume effect (d).

Sample cracking during the scan is probably related to the high temperature determined by the radiation dose. We attempted to avoid this undesired effect by keeping the specimen at a low temperature during imaging, by means of cryogenics. We tested two instruments, Cryostat (Cosier & Glazer, 1986) and Coldgun. The first one is based on liquid nitrogen and the second one blows cold air on the sample. Both systems induce slight sample motion on the rotation stage, which at this spatial resolution becomes considerable. Since we work at a spatial resolution close to the diameter of the targeted features, the motion artefacts created by these cryogenic instruments make our objective unreachable.

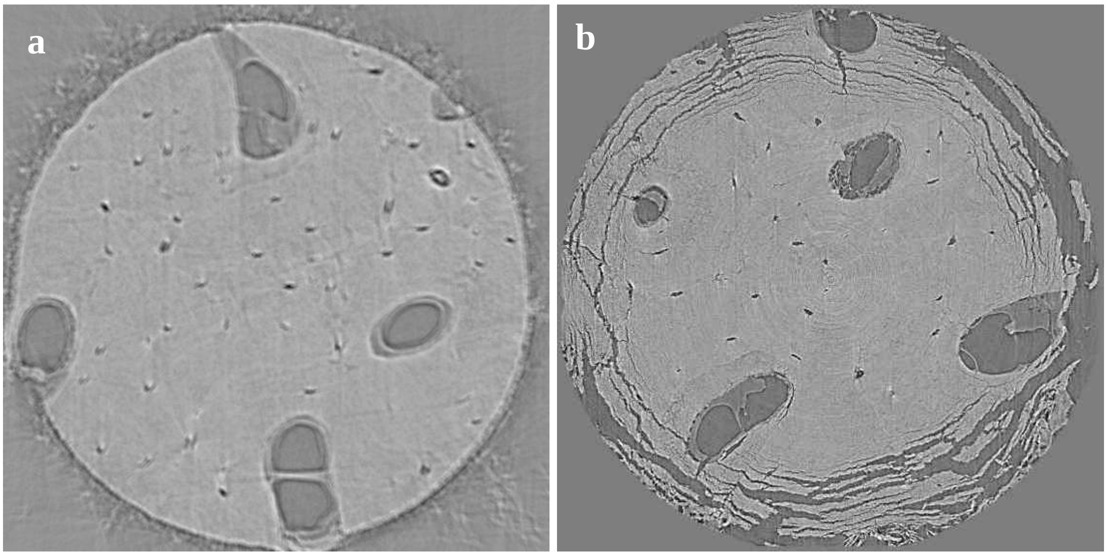

Figure 33 Slices from reconstructed images after scanning the sample under cryogenic conditions. a) The mounted system for Cryostat determines slight sample motion during the rotation for imaging, due to the tubes necessary to be attached to the sample stage. In addition, condensation can occur. b) When scanning the sample at room temperature subsequent to freezing, the damage due to high gradients of temperature is important.

Figure 33 shows slices in the images obtained during experiments with a liquid nitrogen Cryostat. Figure 33 illustrates the effects of freezing and mounting of the Cryostat on the sample rotation stage. The attachment of the Cryostat tubes circulating cold air under a bell which covers the specimen, induces slight motion during the scan, which blurs the image. The relatively rapid and important changes in temperature applied to the specimen, induced sample cracking (Figure 33b). One can observe that the orientation and localization of the micro-cracks in this case is distinctive from the ones occurring usually due to radiation dose.

The following section includes a paper submitted for publication, in which we evaluate the imaging system with respect to the instrumentation and the acquisition conditions, for imaging the lacuno-canalicular network in bone. Optimal setups and protocols are suggested and the results are demonstrated.

Nanoscale imaging of the bone cell network with synchrotron X-ray tomography: optimization of acquisition setup

Alexandra Pacureanu, Max Langer, Elodie Boller, Paul Tafforeau, Françoise Peyrin

Manuscript submitted to Medical Physics

Abstract

Purpose The fundamental role of the osteocyte cell network in regulating the bone remodeling has become evident in the last years. This has raised the necessity to explore this complex three-dimensional (3D) interconnected structure but the existing investigation methods can not provide an adequate assessment. We propose to use parallel beam synchrotron CT at the nanoscale (SR-CT) to image in 3D the osteocyte lacuno-canalicular network. To this aim, we study the feasibility of this technique and we present an optimized imaging protocol suited for the bone cell network. Moreover, we demonstrate the polyvalent information provided by this method.

Methods The high brilliance of synchrotron radiation combined with state of art detectors permits reaching nanoscale spatial resolution. With a nominal pixel size of 280 nm, the parallel beam CT set-up at the ID19 experimental station (ESRF) is capable of imaging the bone lacuno-canalicular network, considering that the reported diameter of canaliculi is in the range 300 – 900 nm. However, the actual resolution is limited by the detector and by the radiation dose causing sample damage during the scan. We sought to overcome these limitations by optimizing the imaging set-up and the acquisition parameters in order to minimize the necessary radiation dose to create the images and to improve the spatial resolution of the detector.

Results We achieved imaging of the osteocyte cell network in human bone. Due to the optimization of the imaging set-up and acquisition parameters, we obtained simultaneously a radiation dose reduction and an increase of the signal to noise ratio in the images. This permitted us to generate the first 3D images of the lacuno-canalicular network in an area covering several osteons, the fundamental functional units in the bone cortex. The method enables assessment of both architectural parameters of the micro-porosity and of mineralization degree in the bone matrix. We found that the cell network is dense and connected inside osteonal tissue. Conversely, the cell lacunae are sparse, unorganized and disconnected in interstitial tissue.

Conclusions We show that SR-CT is a feasible technique to assess the LCN in 3D. This is possible due to an optimal imaging setup in which the detector plays an important role. We could establish two valid setups, based on two different insertion devices. These results give access to new information on the bone cell network architecture, covering a number of cells two orders of magnitude greater than existing techniques. This enables biomedical studies on series of samples, paving the way to better understanding of bone fragility and to new treatments for bone diseases.

5.1 Introduction

Lacuno-canalicular network in bone

Our bones are designed to offer us a strong body support while being light to ease movement. This is possible thanks to an optimized multiscale hierarchical organization, together with a balanced composition of mineral crystals and collagen proteins, combining stiffness and elasticity. Throughout the adult life, bone tissue undergoes remodeling as response to external mechanical environment or in order to repair microdamage and renew old tissue(Rik Huiskes et al., 2000) (Taylor et al., 2007). If the equilibrium between tissue resorption and formation is lost, or the mechanisms controlling the remodeling process are faulty, bone becomes brittle, fragile and exposed to sudden failure. This leads to bone disease such as osteoporosis, which affects one in three women and one in twelve men over the age of 50 worldwide.

It is well known that bone tissue is resorbed by multinucleated osteoclasts and formed by osteoblasts, which subsequently get trapped in the mineralizing matrix and become osteocytes. But it is still not entirely elucidated how, where and when these cells are activated. During the last decades attention has been brought to the osteocytes, the most abundant bone cells, earlier considered generally passive. These cells, distributed throughout the bone matrix and interconnected via dendritic processes, have proved to be the regulators of bone remodeling (Bonewald, 2011). Osteocytes can sense the mechanical stimuli via mechanotransduction, they can detect microdamages severing their dendritic processes and as consequence activate locally bone resorption and formation (Adachi et al., 2009).

In the hard bone matrix, osteocytes occupy small spaces fitted to their size and shape named lacunae and their dendritic processes extend in slender channels called canaliculi. This microscopic porosity, known as the lacuno-canalicular network (LCN), forms a connected communication network in bone, enabling transport of nutrients, waste and signals. The architecture and degree of connectivity of the LCN reflects the viability of osteocytes and the local tissue quality (Elisabeth H. Burger & Jenneke Klein-Nulend, 1999) (Mishra & Knothe Tate, 2003). It has been suggested that there is a strong relationship between the architecture of the LCN and the pathological state of the bone (Melissa L. Knothe Tate et al., 2004).

Existing imaging methods

As a consequence of these findings, the assessment of the LCN has become necessary. However, a combination of factors specific to the LCN makes the exploration of this structure difficult. Being embedded in the solid mineralized matrix makes it difficult to be reached by light, the nanoscale size of canaliculi (300-900 nm) requires a high spatial resolution technique, while its three dimensional (3D) complexity and expansion over ~ 200 µm in width and up to several thousands µm in length, in a single osteon, requires a large field of view.

The most common investigation techniques are based on optical microscopy (transmission, polarized light, oil immersion, confocal microscopy) (Shapiro, 1988) (Ciani, Doty, et al., 2009) (Sugawara et al., 2005) (H. Kamioka et al., 2001), electron microscopy (transmission, scanning) (Hiroshi Kamioka et al., 2009), or atomic force microscopy(Reilly et al., 2001) (Lin & Xu, 2010). These methods provide 2D measurements of the LCN from which 3D parameters can be inferred. However, due to their limitations in field of view and penetration depth only a limited region of the LCN can be observed. Moreover, the quantitative assessment relies on idealized models, hence it is not accurate. Recent works reported methods to image quantitatively in truly 3D the LCN, such as ptychography (Dierolf et al., 2010) or focused ion beam combined with scanning electron microscopy (FIB-SEM) (Stokes et al., 2005) (Schneider et al., 2011). While these methods permit precise 3D evaluation of one up to three lacunae and their canaliculi, they restrict exploration of the LCN in a statistically significant volume, considering that in each osteon there are hundreds or thousands of osteocyte lacunae. In addition, these methods require complex sample preparation and the imaging duration for one sample is rather long (more than 24 hours for the methods presented in (Dierolf et al., 2010). Therefore, the limitations of the existing imaging methods makes the assessment of the LCN on series of samples unfeasible, which is necessary for biomedical conclusions.

Potential and challenges in using SR-CT at the nanoscale

The aim of this work is to achieve imaging of the LCN with parallel beam, synchrotron X-ray nano computed tomography (SR-CT). This technique benefits from several attributes recommending it as suitable for 3D quantitative exploration of the LCN. The high penetration power of X-rays, combined with high brilliance of the synchrotron radiation and with cutting edge X-ray detectors, give access to 3D images of bone tissue with isotropic nanoscale resolution, while keeping a relatively large volume of view (VOI). The possibility to select a monochromatic beam makes the reconstructed X-ray attenuation maps quantitative, i.e. the local degree of mineralization in the bone matrix can be evaluated (Nuzzo et al., 2002). This method is non-destructive, does not impose thin slicing of the specimens or any modifying sample preparation. The average acquisition time, with the currently available set-up at ID19 experimental beamline (ESRF), is about 40 minutes.

However, imaging of the LCN with SR-CT is not straightforward and has recently been considered unattainable (Schneider et al., 2010). One of the main challenges is the necessity to push the spatial resolution close to the diffraction limit of the visible spectrum, in order to achieve imaging of the canaliculi (~300-900 nm in diameter; 280 nm pixel size). The second major difficulty raises from the high radiation dose applied to the sample in order to create an image with nanoscale resolution.

Conversely to cone-beam acquisition geometry, the parallel beam allows exact tomographic reconstruction. Nevertheless, in this case the spatial resolution is limited by the detector, in particular by the scintillator which converts X-rays to visible light. The characteristic point spread function of the scintillator is the main determinant of the achievable spatial resolution and its conversion efficiency affects directly the necessary radiation dose. For higher efficiency the scintillator needs to be thick; conversely, for better spatial resolution it must be thin, hence a compromise is required. With a nominal pixel size close to the diameter of the canaliculi, a loss in resolution is not acceptable.

On the other hand, at very high levels of radiation dose the bone specimens become instable during the scan. This is due to generation and propagation of micro-cracks, or due to slight dehydration causing sample shrinking. These phenomena result in motion artifacts which make the reconstructed images unusable, considering that canaliculi occupy only one or two voxels in width. Therefore, an optimization of the imaging set-up and of the acquisition conditions is required to achieve imaging of the LCN.

5.2 Methods and materials

Imaging system

Image acquisition was performed at the ID19 experimental station (Weitkamp et al., 2010) (Salomé et al., 1999) at the European Synchrotron Radiation Facility (ESRF), Grenoble, France. Synchrotron radiation has several properties yielding exceptional performance in imaging. Due to elevated intensity, high spatial resolution can be reached while maintaining short acquisition times. The high flux also enables the selection of a monochromatic beam, which yields a high density resolution and eliminates beam hardening artifacts. At the ESRF, electrons circulate in a storage ring (844 m in circumference) with an energy of 6 GeV, producing very brilliant hard X-rays.

ID19 is a long insertion-device beamline dedicated to full-field parallel-beam imaging techniques. The distance of 145m between the experimental hutch and the source permits to obtain a parallel beam CT set-up (Figure 34). The beamline has two undulators (U32, U17.6) and a wiggler, as insertion devices. We used the undulators to generate X-rays since they yield a greater flux, which is desirable for high resolution experiments. The magnetic field is tuned by changing the gap between the upper and lower arrays of magnets. A monochromatic X-ray beam can be selected with a single-bounce multilayer in Bragg reflection geometry (Ru/B4C with a period of 4 nm, on Si substrate) giving a monochromaticity $\Delta E/E \approx 10^{-2}$.

The detector is composed of a scintillator converting X-rays to visible light, a magnifying optic system and a FReLoN (Fast Read Low Noise) cooled charge-coupled device (CCD) camera(Labiche et al., 2007). Two CCD cameras (FReLoN HD2K and FReLoN E2V) were evaluated.

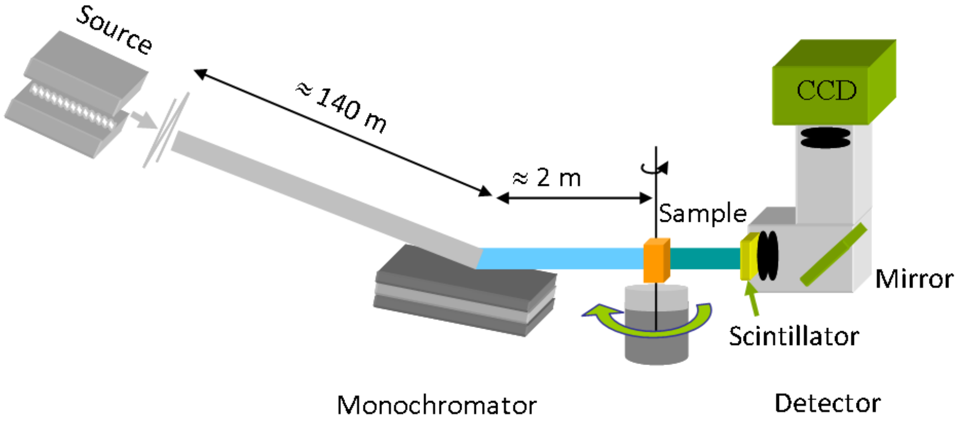

Figure 34 : Imaging set-up for parallel beam SR tomography at ID19. The source is situated at long distance from the experimental hutch, enabling to obtain a parallel beam, from which a single energy is selected with a multilayer monochromator. The sample is fixed on a precise rotation stage and projections are recorded for about 2000 angles. The detector is composed of a scintillating screen, a magnifying optic system and a CCD camera.

Several scintillators were tested: Ce doped Y3Al5O12 with a 25 µm thickness (YAG:Ce_25µm), Eu doped $Gd_3Ga_5O_{12}$ with a 10 µm, 6.6 µm and 6.2 µm thickness (GGG :Eu_6.2µm) and Tb doped Lu_2O_3, SiO_2 with a 4.5 µm thickness (LSO :Tb_4.5µm) (T. Martin et al., 2009).

The effective pixel size was set to 280 nm, giving a field-of-view of 574 µm. Different experimental conditions were tested in order to find the optimal parameters. These conditions are summarized in Table 1.

Image analysis

The 3D images were obtained from the projection images by applying the filtered backprojection algorithm (PyHST, developed at ESRF). Since the acquisition system is using a parallel beam, there is no magnification, no cone beam artifacts, and the tomographic reconstruction is exact (Salomé et al., 1999). The size of the cubic voxel in the reconstructed images is about $(280)^3$ nm^3. The volume-of-interest (VOI) of 2048x2048x2048 voxels corresponds to $(574)^3$ μm^3.

For image quality appraisal with different imaging conditions, we evaluated the signal to noise ratio (SNR) in the reconstructed images (coded in 32 bit real). The signal to noise ratio (SNR) was evaluated as the ratio between the mean value in a homogenous region in the sample and the standard deviation measured in the air. For each image we performed 10 measurements covering around 100 000 pixels in total and retained the mean value of the results.

For the visualization of the lacuno-canalicular network we used a 3D line enhancement filter (Sato et al., 1998) to improve the contrast of canaliculi with respect to the bone matrix. This filter is based on eigenvalue decomposition of the second order structure of the image, computed locally. The mutual relations between the eigenvalues permit to identify voxels belonging to a tubular-like structure, with the size given as a parameter. The voxels that are likely to be part of canaliculi are highlighted while the rest of the voxels are darkened. The algorithms for image analysis were implemented in C and C++ languages, based on an in-house library and on the ITK library (Kitware). For data visualization and generation of 3D renderings we used the software Avizo (VSG) and ImageJ (NIH).

Evaluation of radiation dose

For the estimation of the incident photon flux for each set of acquisition conditions, we used the tool XOP (Sanchez del Rio, M, 2004) to simulate the insertion device, the monochromator and the attenuators. The undulator radiation depends on the electron energy in the storage ring, on the undulator spatial period and on the maximum angular deviation from its axis, K (Als-Nielsen & McMorrow, 2011):

$$K = 93.4 \times \lambda_u \times B_0 \quad (1)$$

where λ_u [m] is the undulator spatial period and B_0 [T] is the maximum magnetic field.

The magnetic field varies with the gap between the magnet arrays. In Figure 35 are represented the resulting spectra of the two undulators used during the experiments, for a set of parameters (U32: gap = 12 mm, K = 1.8, I = 170mA; U17. gap = 18 mm, K = 0.14, I = 160mA). The spectrum of the undulator U32 is characterized by multiple narrowband peaks, while U17.6 outputs a nearly monochromatic flux.

The flux attenuation introduced by the beryllium window (0.5 mm thickness) and by the filters used for the absorption of low energies (Diamond 0.3 mm thickness, Aluminium 0.25 mm, 0.5 mm, 1 mm thickness), was assessed as well and the resulting flux was determined. The measurements were made in the range 1-100 keV with a resolution of about 0.1 keV. The reflectivity of the multilayer monochromator was simulated for each of the used energies.

The radiation dose is measured in grays (1 Gy ≡ 1 J kg−1) and it was estimated using the following procedure(Attix, 1986) (Barth et al., 2010). The radiation dose rate D_r [Gy/s] is computed from the energy density and from the X-ray mass attenuation coefficient of cortical bone μ / ρ [mm2/g] (http://physics.nist.gov/PhysRefData/XrayMassCoef). The energy density is obtained from the photon flux density ψ [ph/s/mm2], the elementary charge $1{,}6 \times 10^{-19} J / eV$ and the beam energy [eV]. The total applied dose D_t is then found by multiplication with the exposure time t [s].

$$D_r = \psi \times E \times 1{,}6 \times 10^{-19} \times \mu / \rho \times 1000 \qquad (2)$$

$$D_t = D_r \times t \qquad (3)$$

Sample preparation

Specimens were extracted from the mid-diaphysis of human (women, 78 and 92 years old) femurs obtained from a multi-organ collection. A slice of approximately eight millimeters thick was cut perpendicular to the bone axis at the mid-shaft of each femur. Bone samples underwent a treatment (Biobank, Presles en Brie, France) consisting of supercritical carbon dioxide for delipidation, chemical bath in order to eliminate medullary proteins and gamma irradiation for sterilization. After this treatment, samples are considered to be stable in time and can be stored at room temperature.

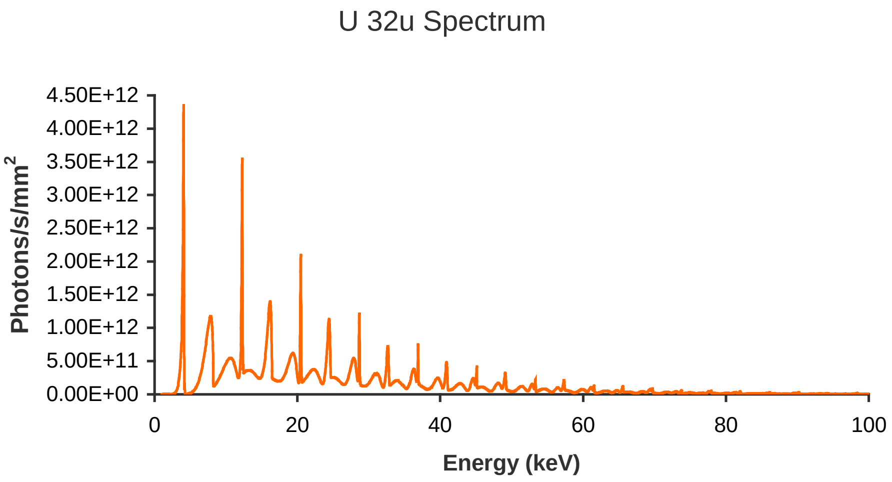
U 32u Spectrum

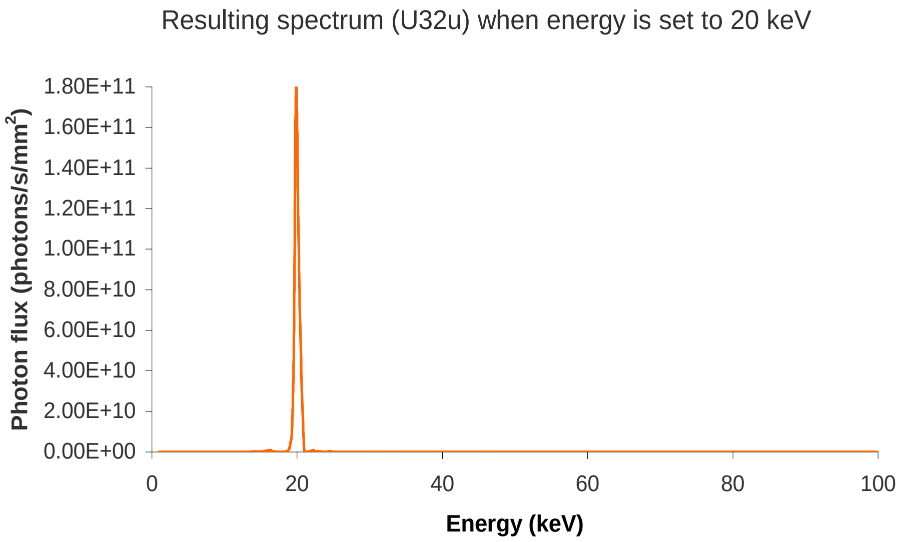
Resulting spectrum (U32u) when energy is set to 20 keV

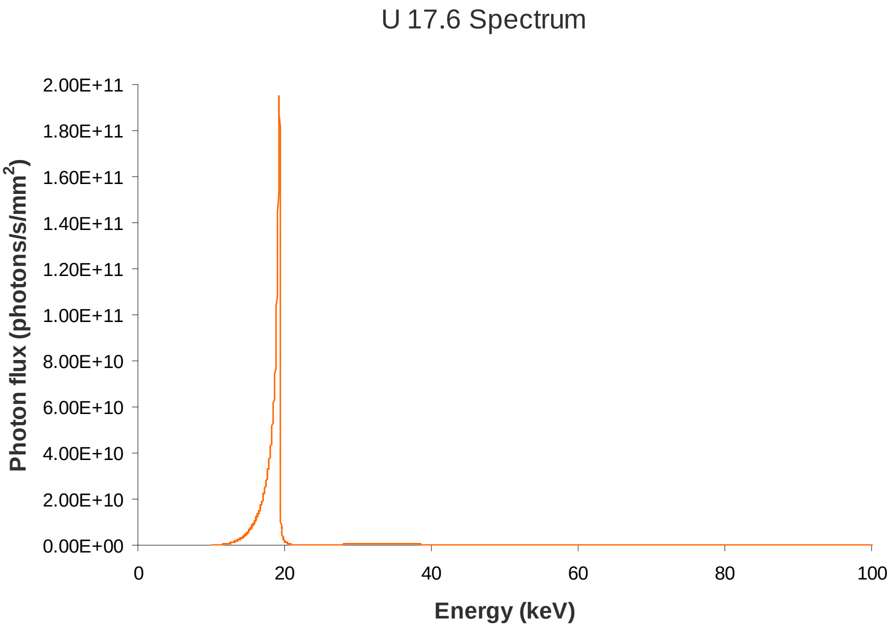
U 17.6 Spectrum

Figure 35 Characteristics of the undulators and of the monochromator. a) Spectrum of the undulator U32u (50 periods of λ_u = 32 mm) for the following parameters: gap = 12 mm, K = 1.8, I = 170 mA. b) Spectrum of the undulator U17.6 (79 periods of λ_u = 17.6 mm) for the following parameters: gap = 18 mm, K = 0.14, I = 160 mA. c) The resulting spectrum with U32u, after the attenuators and the monochromator, when the energy is set at 20 keV.

Ethical approval for the samples was granted by the Human Ethics Committee of the "Centre du don des Corps" at the University René Descartes (Paris, France). The tissue donors or their legal guardians provided informed written consent to donate their tissue for investigation, in accord with legal clauses stated in the French Code of Public Health. Small parallelepiped samples (0.4 mm x 0.4 mm x 5 mm) were then cut with a diamond saw for imaging.

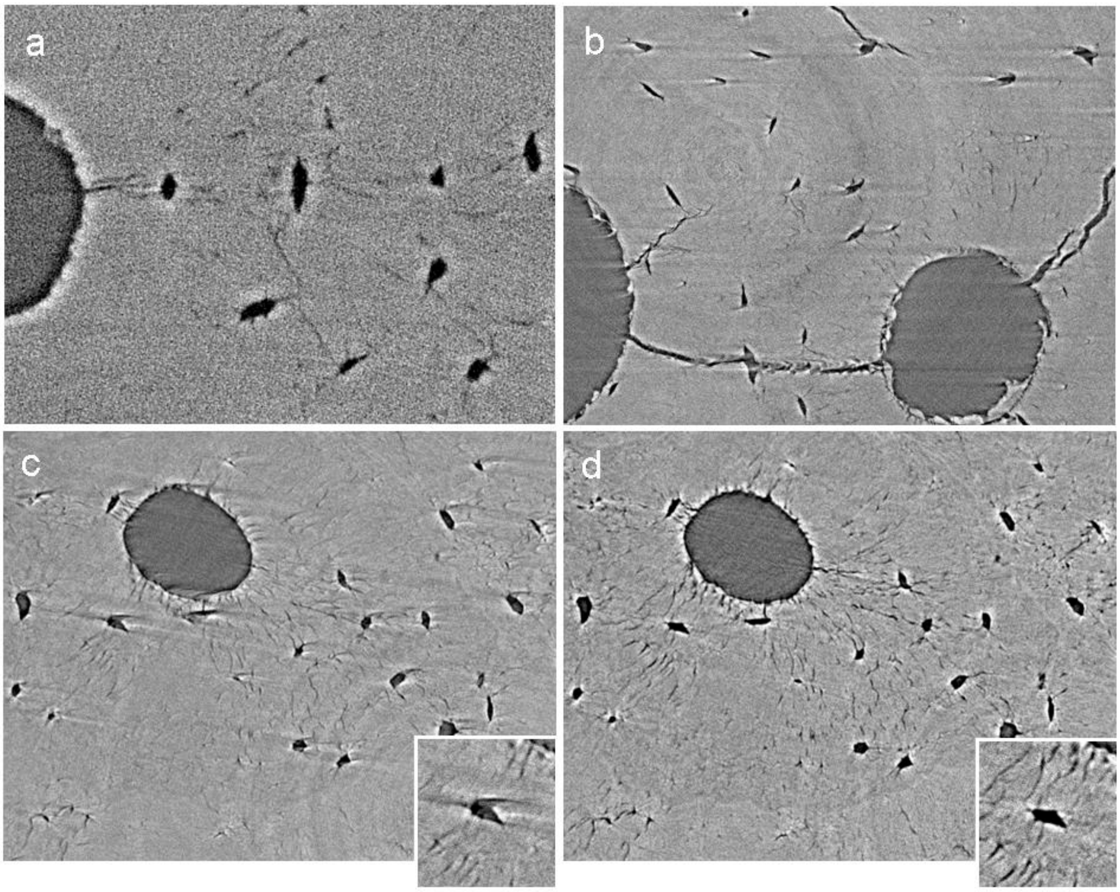

Figure 36 Illustration of the main difficulties to cope with. a) A high level of noise prevents the visibility of canaliculi at this resolution. b) Micro-cracks formation and propagation entail sample damage and motion artifacts. c) Sample motion due to shrinkage during the scan (dehydration). d) The same region reconstructed from a second scan, during which the sample was stable.

5.3 Results

Imaging setup

The first exploratory experiments did not achieve adequate imaging of the bone cell network due to sample motion during the scan and to insufficient efficiency and spatial resolution of the detector. Figure 36 illustrates how the encountered difficulties affect image quality. Low signal to noise ratio (Figure 36a) and distortions created by the motion artifacts, generated due to sample cracking (Figure 36b) and shrinking (Figure 36c), make the images unusable.

We found that the scintillator is the key element of the imaging setup, playing a decisive role in the feasibility of the technique to resolve the canaliculi. The scintillator should have high efficiency for converting the energy of the incident X-ray beam into scintillation photons and its characteristic Point Spread Function (PSF) should be as narrow as possible to avoid image blurring, hence spatial resolution loss. In addition, it should be transparent to its own scintillation light and resistant to radiation damage.

We tested a set of scintillators, described in the methods and materials section and found that the Tb doped Lu2O3, SiO2 with a 4.5 µm thickness (LSO :Tb_4.5µm) provides simultaneously high efficiency and good spatial resolution. The LSO substrate is, unlike YAG or GGG substrates, free from intrinsic luminescence yielding an improved spatial resolution (Paul Antoine Douissard et al., 2010). In the same time, LSO:Tb single crystal films present higher conversion efficiency and better X-ray absorption efficiency than the YAG:Ce or GGG:Eu thin films. In Table 1 it is shown that, by using this scintillator combined with the FReLoN E2V CCD camera, we obtain both lower radiation dose and higher signal to noise ratio. Figure 37 shows a comparison of three detector configurations in terms of image quality and canaliculi visibility. We could establish valid configurations with each one of the undulators. U32 allows a greater variation of the energy and a slightly higher monochromaticity due to the multilayer monochromator. On the other hand, U17.6 generates a nearly monochromatic flux, hence the multilayer monochromator is no longer necessary.

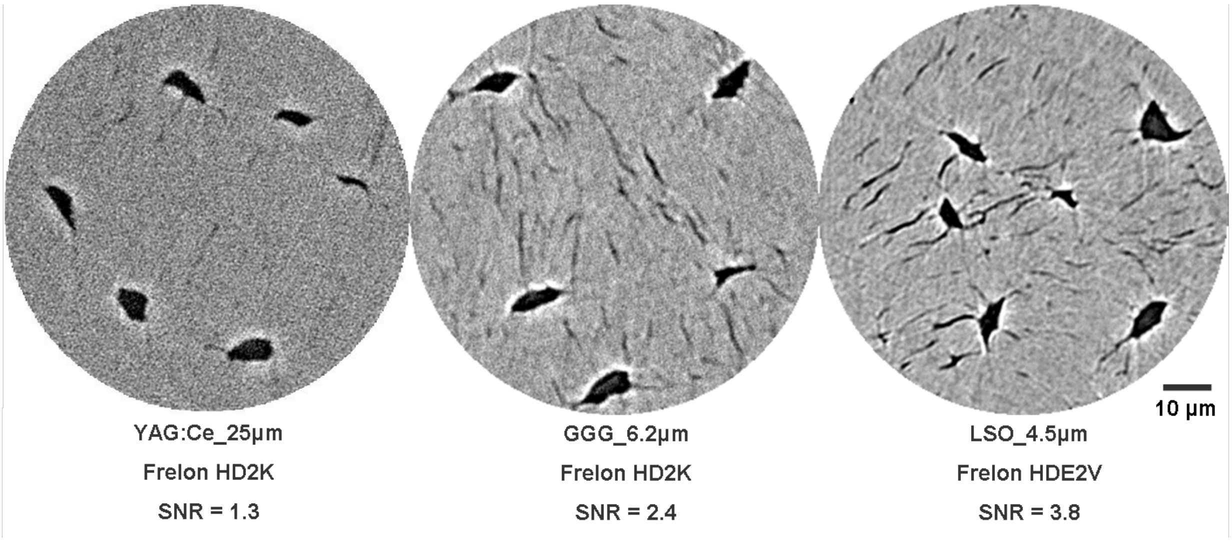

Figure 37 Visibility of canaliculi with three different scintillators coupled with a CCD camera. While using YAG:Ce_25um, the image resolution is affected and the signal to noise ration is low, despite the high number of projections (3500) acquired for the scan. With GGG_6.2um the canaliculi are visible but the image is still quite noisy. LSO_4.5um, combined with the HDE2V camera, give simultaneously better resolution and good SNR.

This yields potentially higher flux and the acquired images are no longer affected by artifacts due to the monochromator, leading to good beam stability over time and clean beam profile. As a consequence, the problem of ring artifacts, determined by the multilayer in the reconstructed images, is eliminated. The limitation in setting various beam energies with this insertion device is not problematic as long as the sample has similar attenuation characteristics (for cortical bone the sample cross section should not be much bigger than the FOV).

Sample preparation

Two types of sample preparation were tested: dry bone, prepared as described in the methods and materials section and bone specimens fixed in a resin (methyl methacrylate). The results suggested that delipidation and drying of the tissue is the optimal preparation. The embedded samples showed higher instability during the scan, due to the effects of the high temperature on the resin. We observed that by placing the sample in the experimental hutch a few hours before performing the scan in order to adapt to the temperature and humidity, sample motion was noticeably reduced.

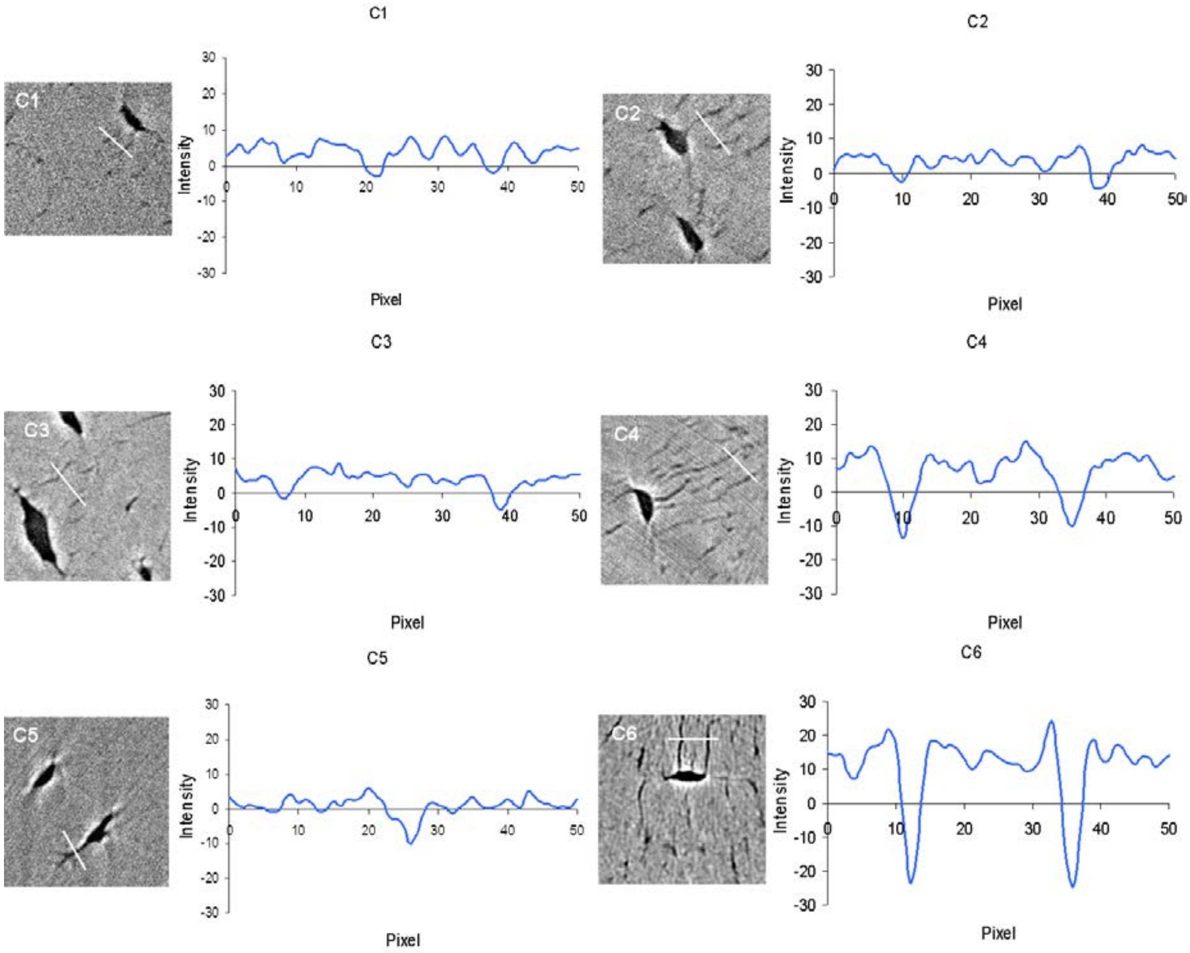

Figure 38 Profile plots along the line marked in the images, showing the visibility and contrast of canaliculi corresponding to different acquisition conditions (Table 1). The region for the measurements was selected to correspond to the best visibility of canaliculi identified for each set of conditions.

Ideally, the samples should be cut in cylindrical shape with a diameter of about 550 µm. In this case, the entire FOV is used and the reconstructed image is not affected by projection truncation due to local tomography (sample bigger than the FOV). If the available cutting tools make it difficult to achieve these characteristics, any size and shape is appropriate as long as it is not much bigger than the FOV. When the sample is large (6-9 mm cross section), the energy needs to be adapted and a higher number of projections is required. This resulted in a noisier image and higher radiation exposure, causing sample cracking (Figure 36b).

Acquisition parameters

The parameters to be set for imaging, such as the energy, the number of projection angles, the exposure time for each projection image or distance of propagation, depend on the setup, the machine mode and of the sample. However, we could establish some optimized general parameters. For the case where the sample is compact bone, cut to fit the FOV, we found that the suited energy is around 20 keV and a number of 2000 angular projections, recorded during a sample rotation of 180°, is appropriate. We tested projection numbers ranging from 1 000 to 4 000. The exposure time for each recorded projection depends on the machine mode, on the gap of the insertion device and on the detector. It is generally inferior to one second per image. When using an optimal setup, the total scan duration was about 40 minutes.

At this spatial resolution, phase contrast is always present, due to the relatively long distance between the sample and the detector (Snigirev et al., 1995). To avoid collision during rotation, the sample must be at a distance of minimum 2 mm from to the detector. In our case, phase contrast is desirable because it enhances the contrast of the interfaces between regions with different densities, hence it facilitates the visibility of canaliculi. We suggest to set this distance at around 10 mm in order to obtain phase contrast which is not excessive.

Table 1 summarizes the results obtained with a selection of setups and acquisition parameters. For each trial we report information about the insertion device, the machine mode, the filters and monochromator, as well as the composition of the detector and the sample size. The radiation dose and the signal to noise ratio, associated to each set of conditions, are indicators of the performance of each combination. When using the conditions C4 and C6, we obtained good results. We observed that using the scintillator LSO_4.5µm together with the Frelon HDE2V camera, enabled the acquisition of much sharper images, with improved resolution, while keeping the radiation dose relatively reduced. This is due to a good compatibility between the quantum efficiency spectrum of the camera and the emission spectrum of the scintillator(Paul Antoine Douissard et al., 2010). The obtained results showed that the samples did not undergo micro-cracking if the radiation dose was kept under 2 MGy.

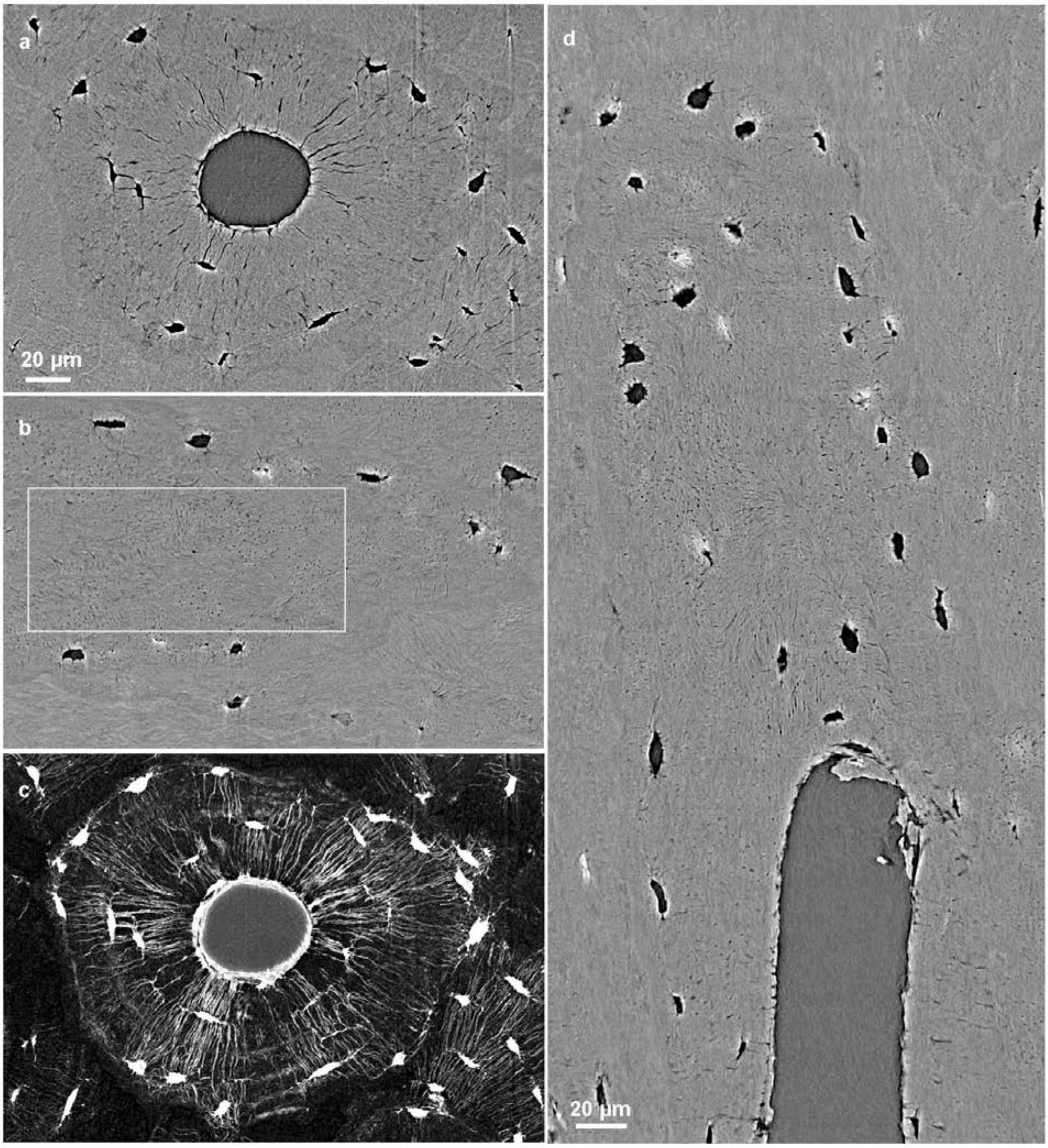

Figure 39 Orthogonal views (a) xy; b) yz; d) xz) and maximum intensity projection (c) over 50 slices in a volume of interest showing details about an osteon.

Figure 38 presents regions of interest extracted from images obtained with each of the imaging conditions presented in Table1. For each detailed image, the profile of a line crossing canaliculi is plotted, to show the level of contrast attained for canaliculi. This line plot is also relevant for the level of noise and for the spatial resolution.

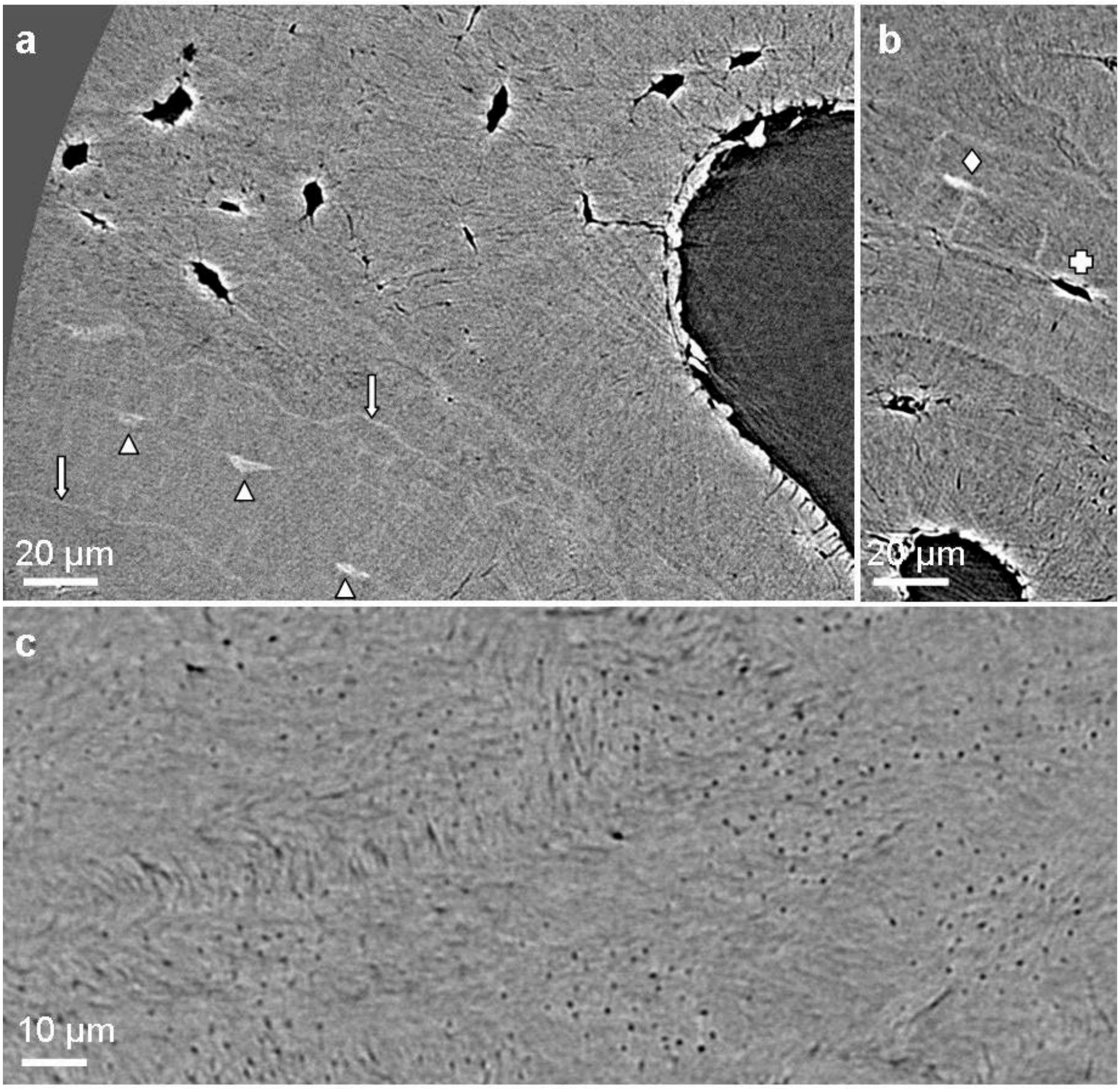

Figure 40 Details in the reconstructed images. a) Interstitial tissue delimited by 2 cement lines (arrows) can be seen in the lower left part of the image. The lacunae (triangles) underwent hypermineralization in this region. b) Hypermineralized lacuna (diamond) and canaliculi can be seen in the vicinity of a normal lacuna (cross) whose canaliculi are filled by mineral. Blocking of the canaliculi would probably entail death of the cell. c) Magnification of the region boxed in Fig. 5b. The canaliculi appear as dots and the collagen fibers orientation starts to be visible.

Information retrieved in the reconstructed images

The reconstructed images contain substantial information about the bone tissue at the sub-micrometric scale. The primary direct information is about the 3D architecture and integrity of the lacuno-canalicular system. Figure 39 illustrates regions in orthogonal slices (a,b,d) selected around an osteon, as well as a maximum intensity projection over 50 transverse slices permitting to observe the cell porosity. The organization of the cell lacunae in concentric layers around the Haversian canals can be observed together with their size, shape and orientation. Figure 41 displays a 3D rendering of the porosity in a volume of interest selected to contain the osteon visible in Figure 39.

Canaliculi appear as slender tubes, orientated mostly perpendicular to the Haversian canal. In a slice parallel with the vessel canal, canaliculi appear as groups of dots (Figure 41c). The high level of the cell connectivity via canaliculi, inside the osteons is revealed. In the interstitial tissue, lacunae are sparse and disorganized and canaliculi are almost absent (Figure 39c). Moreover, due to the correlation between X-ray attenuation and the mineralization degree (Nuzzo et al., 2002), variations of mineral content within the tissue can be identified. Based on this information, the Haversian systems can be delimited and the newer ones can be distinguished from the older osteons. At the same time, the cement lines can be observed, showing a higher level of mineralization comparing both the osteonal and the interstitial tissue (Figure 40a,b).

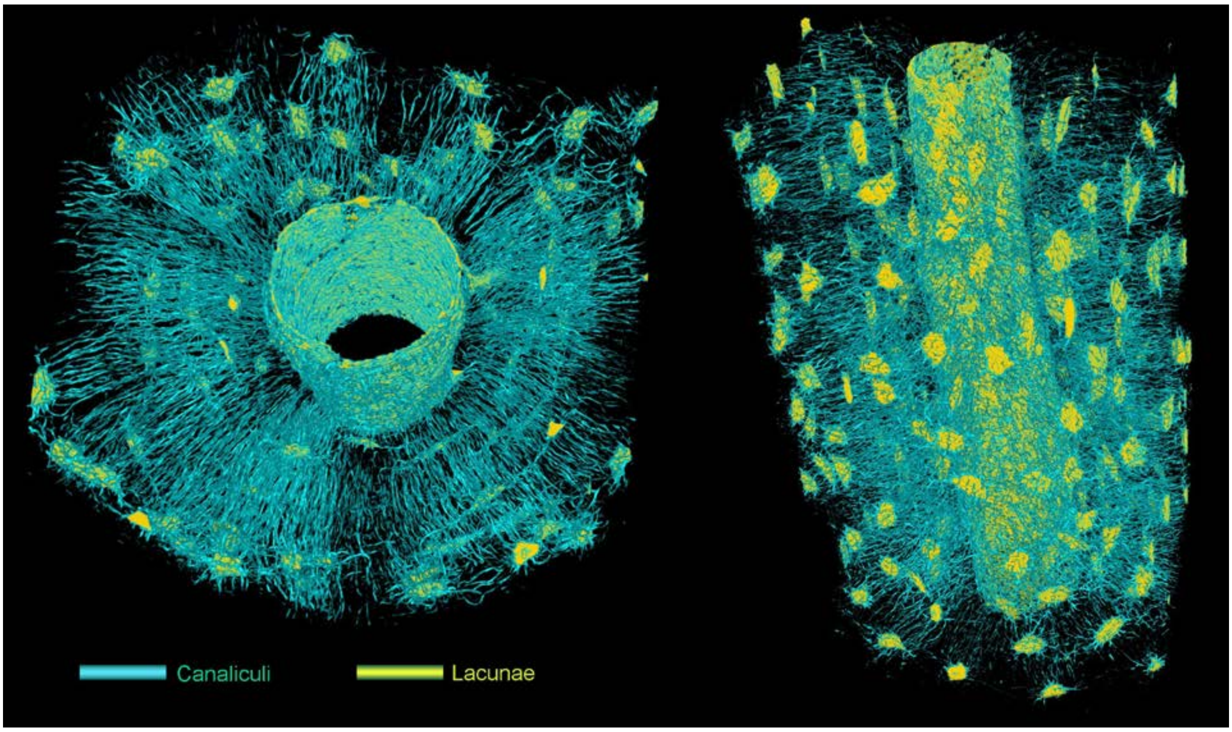

Figure 41 3D rendering of the osteocyte network organized around a Haversian canal (left - transverse view, right – frontal view). The lacunae are represented in yellow and the canaliculi in blue. The osteon visualized here corresponds to the one presented in Figure 6.

5.4 Conclusions and discussion

We demonstrated and evaluated here the feasibility of parallel beam SR-CT for imaging the bone lacuno-canalicular network. We show that SR-CT can now resolve in 3D this cell network, providing unprecedented investigation opportunities. Comparing to existing methods, the technique we propose gives access to unbiased appraisal of tissue covering a large number of cells. With a nominal pixel size of 280 nm and using a CCD detector measuring 2048×2048 elements, a VOI of approximately $574 \times 574 \times 574\ \mu m^3$ is imaged. This incorporates several thousand osteocyte lacunae compared to less than ten with other 3D imaging methods. In addition, SR-CT yields information on the mineralization degree in the bone matrix, making possible concurrent study of the structure and the composition of bone tissue at this scale. As opposed to scanning 3D techniques, this method maintains the acquisition duration sufficiently short to pursue imaging of sets of samples, necessary to reach statistically significant biomedical conclusions.

In order to find an imaging protocol suited for the LCN we tested a set of setups and acquisition conditions. The main challenges are the restriction of the spatial resolution and of the radiation dose. Image quality depends on a great number of factors, from the properties and performance of X-ray insertion devices, of the monochromator, or of the individual detector components, to sample characteristics and imaging parameters. Considering that beam time at the synchrotron facilities is limited and that putting together a setup can take several hours, the performed experiments were carried out under certain restrictions. Subsequent to a series of trials we established a viable imaging procedure based on the two undulators available as insertion devices at ID19 (ESRF). We concluded that the samples should preferably be dried and cut in such a way that the cross section fits in the FOV (~ 570 ×570 μm). The X-ray beam energy should be around 20 keV and 2 000 angular projection were sufficient.

The detector is decisive for a successful acquisition, influencing both the necessary radiation dose and the image quality. We presented an optimal combination between a scintillator and a CCD camera, currently available at ESRF. When using this setup, the radiation dose can be considerably reduced while the SNR is noticeably increased.

Research is continually progressing in the domain of X-ray detectors, hence these devices are likely to improve.

The dose effect of radiation exposure on the sample is poorly known in nanoscale CT. We have quantified the dose and we have observed that it yields cracking and instability of the sample during the scan. Exposure dose has most likely other effects on the bone material but here we have investigated the effect of dose only from an imaging point of view.

This method enables unprecedented studies of the morphology of the osteocyte cell network correlated with the degree of mineralization in the bone matrix. The 3D organization and integrity of this network can be investigated inside and outside the osteons, and the size (Hannah et al., 2010), shape (Vatsa et al., 2008) and orientation of the cell lacunae can be automatically measured. The structure observed in the acquired 3D images corresponds to the one expected from the extrapolation of the 2D images, provided by other techniques.

These findings are relevant to the fields of bone biology, pathology and physiology. This newly available data creates valuable input for biomechanical (Liyun Wang et al., 2005) studies at the cell level, due to direct access to 3D information on the lacuno-canalicular network, covering for the first time entire osteons. The osteons are fundamental structural and functional units of bone cortex and the study of the cell network within these systems was not possible previously. This method enables the assessment of tissue quality and evolution with age (Mullender et al., 1996), disease or treatment (Yajima et al., 2010). In addition, it permits the study of hypermineralized lacunae (Busse et al., 2010) and canaliculi which are related to micropetrosis (Frost, 1960) Figure 40a,b). This type of data can contribute as well to further advances in dentistry and biomaterials design.

To conclude, we proposed and evaluated a valid procedure for imaging of the bone lacuno-canalicular network with parallel beam SR-CT. Unique visualizations of the bone cell network were presented. Future work will focus on improving the resolution and image quality, as well as on developing methods for automatic segmentation and quantification of the osteocyte network from the obtained 3D images.

Imaging Set-Up	**C1**	**C2**	**C3**	**C4**	**C5**	**C6**
Insertion device	U32	U32	U32	U32	U32u+U32d	U17.6
Gap of the ID (mm)	13.5	12	12	11.95	12/12.63	18
Filters	Al_0.25mm	Al_0.5mm	Al_0.5mm	Al_1mm	Al_1mm	N.A.
Monochromator	Ru/B4C on Si	Ru/B4C on Si	Ru/B4C on Si	Ru/B4C on Si	Ru/B4C on Si	N.A.
Machine current (mA)	185	160	150	175	85	160
Scintillator	YAG:Ce_25µm	GGG_6.6µm	GGG_6.6µm	GGG_6.2µm	GGG_10µm	Lso_4.5µm
CCD Camera FRELON	HD2K	HD2K	HD2K	HD2K	HD2K	HDE2V
Sample section (mm^2)	9	9	2	0.5	0.5	0.25
Energy (keV)	25	25	25	20.5	40	19
(μ/ρ)(cm^2/g)	2.2	2.2	2.2	3.3	0.45	4.2
μ (cm^{-1})	4.1	4.1	4.1	6.1	0.8	7.8
Photon flux density (ph/s/mm2)	2.54E+12	2.32E+12	2.20E+12	1.99E+12	2.00E+12	1.90E+11
No Projections	3800	4000	3500	2000	2500	2000
Counting time (s)	1.3	1.4	1.3	0.8	1	0.7
Exposure time (s)	4940	5600	4550	1600	2500	1400
Radiation dose rate (kGy/s)	2.24	2.04	1.94	2.15	0.58	0.24
Total radiation dose (MGy)	**11.0**	**11.4**	**8.8**	**3.4**	**1.4**	**0.3**
Standard deviation in the air	3.1	2.4	1.6	3.3	1.6	2.2
Mean in bone matrix	4.1	4.4	4.0	8.0	1.9	10.3
SNR	**1.3**	**1.8**	**2.5**	**2.4**	**1.2**	**4.6**
Resolution ranking	*	**	**	**	**	***

Table 1 Summary of relevant elements and parameters of the imaging setup together with the corresponding radiation dose and signal to noise ratio, evaluated in the reconstructed images. Information on the insertion devices, monochromator, detector and imaging conditions is provided. We obtained data adequate for the segmentation and quantification of the cell network with the conditions C4 and C6. For these imaging setups, the signal to noise ratio was sufficiently high and the spatial resolution of the detector yielded reasonable contrast for the canaliculi.

Chapter 6

Image enhancement for visualization and segmentation

In this chapter we present a method of image enhancement aiming to improve the visibility of the canaliculi in the acquired images. This permits to visualize (Figure 42) the osteocyte network in the 3D images and it gives the opportunity to obtain a direct segmentation by simple thresholding.

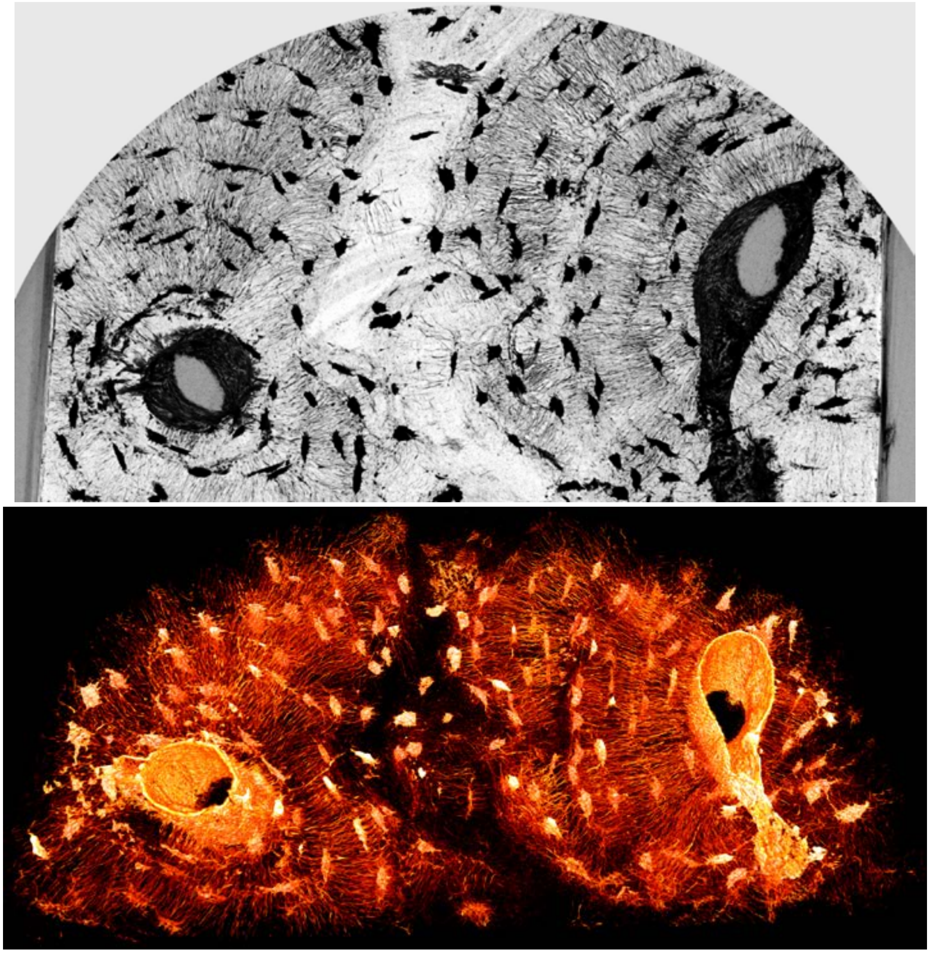

Figure 42 Minimum intensity projection over 256 slices (~72 µm) in a ROI from the original image. b) 3D rendering of the image obtained after filtering with the method proposed below.

Shape-based adaptive filtering for tubular structures in nanoscale synchrotron tomography images

Alexandra Pacureanu, Aymeric Larrue, Zsolt Peter, Vasile Buzuloiu, Françoise Peyrin

Manuscript in preparation for Pattern Recognition Letters

Abstract

The investigation of cellular aspects of bone tissue is generally performed from 2D microscopic techniques. Recent advances in Synchrotron Radiation Micro-CT allow to image biological samples at a sub-micrometric scale. In this paper, we propose to study the feasibility of this technique to visualize the bone lacuno-canalicular system, consisting in a complex network of thin canaliculi (diameter ~ 300-900 nm) joining osteocytes. Due to the limited spatial resolution of the imaging system compared to the structure size and the constraints in term of dose, the images have a low signal to noise ratio and the detection of canaliculi is challenging. We propose a 3D non-linear enhancement technique based on Hessian analysis. The method is evaluated on synthetic images and on experimental data. We also present 3D renderings of the canalicular network.

6.1 Introduction

Worldwide, one of three women and one of five men with the age over fifty suffer from osteoporosis. Leading to fragility fractures of vertebral column, rib or hip, osteoporosis significantly affects the life expectancy and the quality of life. Understanding the causes of bone fragility is thus the subject of substantial current research to prevent and manage bone diseases.

At the cellular level, osteocytes are the most numerous cells in bone and are hypothesized to control the bone resorption and formation, signaling the need for adaptive remodeling (Bonewald, 2011). These sensor cells are hosted within spaces called lacunae and communicate with each other via cytoplasmic extensions that occupy tiny canals called canaliculi. Together, the lacunar and canalicular porosities create a network for signal transfer via mechanical, electrical and chemical mechanisms. The ability of cells to recognize and respond to stimuli is fundamental for tissue health and depends of the architecture of the lacuno-canalicular system (Currey, 2003). The integrity and organization of this system is supposed to change in disease states such as osteoporosis and osteoarthritis (M. L. Knothe Tate et al., 2002) (van Hove et al., 2009). Thus, better understanding the connectivity and orientation of the lacuno-canalicular system is crucial for future development in the etiology, prophylaxis and treatment of bone diseases. So far, studies on the osteocyte system have been performed using microscopic techniques, mainly 2D histology.

In this paper, we propose to study the feasibility to visualize the 3D lacuno-canalicular system from synchrotron radiation computed tomography (SR-CT) images. The main difficulty in imaging the lacuno-canalicular network arises from the size of the canaliculi. The range of the canalicular diameter in human bone is 300 to 900 nanometers which requires a very high resolution imaging system. At the ESRF (European Synchroton Radiation Facility) is now possible to acquire 3D images with a voxel size up to 0.28 µm.

However, at this scale, the detection of thin tubular structures as canaliculi is difficult because of limited signal to noise ratio and partial volume effects. Here, we propose a 3D non linear enhancement method for tubular porosities in bone. We validate the method on synthetic images and we show the results on experimental data.

6.2 Image acquisition

Achieving accurate 3D visualization of the lacuno-canalicular system is conditioned by the experimental image acquisition conditions. The micro-CT setup at ESRF is based on parallel beam geometry. The acquisition consists in recording 2D projections of the sample rotated around a vertical axis with a total angle of view of 180° (Salomé et al., 1999). The 3D image is then reconstructed using a standard filtered backprojection algorithm. To avoid truncation of projections which yields artifacts in the reconstructed image, the sample should fit the field of view (FOV) of the 2D projections. When using a $(2048)^2$ detector and a pixel size of 0.28 µm, the FOV is limited to 574 µm. To fit this FOV, small cylinder samples (diameter: 500 µm, height: 1mm) were cut from cortical bone using a high precision drilling machine.

Tomographic acquisitions were performed in different experimental conditions yielding different absorbed dose on the sample. Higher exposure time and number of projections should theoretically improve signal to noise ratio (SNR) in the reconstructed image. However, in our case, this generates sample motion during acquisition due to radiation dose damage. Thus, the selection of the optimal acquisition parameters becomes a compromise between noise and motion artifact

For the acquisition of the images presented in this paper we used iliac crest biopsy samples embedded in methylmetacrylate from human osteoporotic patients. The specimens were provided by Marie-Hélène Lafage-Proust, from LBTO, St. Etienne, France. We set the energy at 18 keV and recorded 2000 projections with an exposure time of 0.5 s per projection. The scan duration was close to 30 minutes.

Figure 43 illustrates a Region of interest (ROI) (256×256 pixels) in a single tomographic slice. The osteocyte lacunae are clearly visible as elliptic structures. Although some canaliculi can be observed within the slice the contrast is relatively weak.

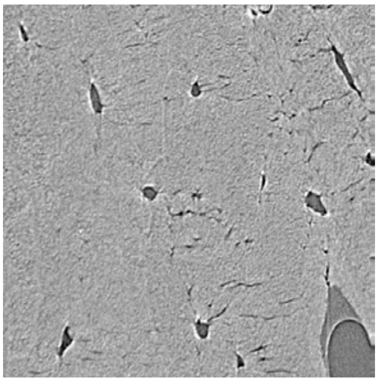

Figure 43 ROI in a 2D reconstructed slice (voxel size 280 nm, image width 70µm) showing osteocyte lacunae and canaliculi.

6.3 Image analysis

In this section, we present a procedure to enhance the features of interest in the 3D SR-CT images. The canaliculi and the osteocyte lacunae are respectively slender tubular and ellipsoidal structures. Since the detection of canaliculi is particularly difficult, we first use a Hessian based filter in order to enhance the visibility of tube-like features. Then, we propose a non-linear filter to combine the geometrical information with the grey levels from the original image.

Hessian-based analysis

Hessian-based filters (Lorenz et al., 1997) (Sato et al., 1998) (Alejandro Frangi et al., 1998) have primarily been proposed to enhance vessels in medical images from different modalities such as Magnetic Resonance Imaging or Computed Tomography Angiography (Olabarriaga S.D. et al., 2003) (Lesage et al., 2009) (Garcia et al., 2010). The Hessian matrix which describes the second-order structure of the local intensity variations, contains shape information about the objects in the image. Since the Hessian matrix is symmetric, it is possible to construct an orthonormal coordinate system from its eigenvalue decomposition. The mutual relationships between eigenvalues correspond to the geometrical properties of the local structure.

Let $f(\mathbf{x})$ with $\mathbf{x} = (x, y, z)$, be a 3D image. Since the second order derivatives are very sensitive to noise, the image is generally smoothed with a Gaussian kernel. Given the commutability of the convolution and derivation operators, the second derivatives of the smoothed image, denoted $f_{\mathrm{ab}}(\mathbf{x};\sigma)$, can be obtained as:

$$f_{\mathrm{ab}}(\mathbf{x};\sigma) = \left\{ \frac{\partial^2}{\partial a \partial b} g_{\sigma}(\mathbf{x}) \right\} * f(\mathbf{x}) \qquad (1)$$

where $g(\mathbf{x})$ is an isotropic Gaussian function with standard deviation σ and a,b are the row and column indices in the Hessian matrix. The analysis may thus be tuned to a specific scale width by adjusting σ.

Let λ_k be the eigenvalue with the k^{th} smallest magnitude ($|\lambda_1| \leq |\lambda_2| \leq |\lambda_3|$) of the Hessian matrix at voxel $\mathbf{x}$ (for simplicity we omit the dependency to $\mathbf{x}$). A voxel in an ideal tubular structure should be characterized by: $|\lambda_1| \approx 0$; $|\lambda_1| << |\lambda_2|$; $\lambda_2 \approx \lambda_3$. For bright structures, λ_2 and λ_3 must have negative values.

Sato et al. make use of two of the eigenvalues to compute a similarity measure (Sato et al., 1998). If $\lambda_c = \min(-\lambda_2, -\lambda_3)$, the line measure at point **x** is defined as :

$$l_S(\mathbf{x}) = \begin{cases} \exp(-\lambda_1^2 / 2(\alpha_1 \lambda_c)^2) & \lambda_1 < 0,\ \lambda_c \neq 0 \\ 0 & \lambda_c = 0 \\ \exp(-\lambda_1^2 / 2(\alpha_2 \lambda_c)^2) & \lambda_1 < 0,\ \lambda_c \neq 0 \end{cases} \quad (2)$$

Frangi et al. proposed a modified criterion (Frangi et al., 1998):

$$l_F(\mathbf{x}) = \begin{cases} 0 & \text{if } \lambda_2 > 0 \ \text{ or } \lambda_3 > 0 \\ (1-\exp(-\frac{R_A^2}{2a^2}))\exp(\frac{R_B^2}{2b^2})(1-\exp(-\frac{S^2}{2c^2})) & \end{cases} \quad (3)$$

where :

$$R_A = \frac{|\lambda_2|}{|\lambda_3|}, \ R_B = \frac{|\lambda_1|}{\sqrt{|\lambda_2 \lambda_3|}} \ \text{ and } \ S = \sqrt{\lambda_1^2 + \lambda_2^2 + \lambda_3^2} \quad (4)$$

Non linear enhancement

The line filters as defined by Sato or Frangi provide a robust similarity measure to tubular structures. However, these measures are not sufficient to extract the lacuno-canalicular system. Due to their ellipsoidal shape, the lacunae are removed from the filtered image. Moreover, the filter transforms the noise from the original image into a structured background noise. This is due, on one hand, to the fact that the bone matrix doesn't appear homogeneous at this spatial resolution. In addition, the size of canaliculi is in the range of the high frequencies, requiring to tune the filter to detect very fine features, creating opportunities to detect line-like paths formed by the noise.

We propose a non-linear filtering method, combining the 3D line filter map with the original grey-level image. Conversely to linear filters, the kernel is not fixed, but it updates for each image element as function of the local 3D line filter response. The method is inspired from bilateral filters (Tomasi & Manduchi, 1998).

If $f(\mathbf{x})$ denotes the original 3D image, and $l(\mathbf{x})$ is the 3D line-filter map, the expression of the proposed non-linear filter is $f_{NL}(\mathbf{x})$:

$$f_{NL}(\mathbf{x}) = \frac{1}{Z} \sum_{\mathbf{x}' \in W_{\mathbf{x}}} f(\mathbf{x}') \exp(-\frac{1}{2}(\frac{l(\mathbf{x}) - l(\mathbf{x}')}{\sigma_W})^2) \qquad (5)$$

$$\text{with} \qquad Z = \sum_{\mathbf{x}' \in W_x} \exp(-\frac{1}{2}(\frac{l(\mathbf{x}) - l(\mathbf{x}')}{\sigma_W})^2) \qquad (6)$$

where $W_{\mathbf{x}}$ is a neighborhood of $\mathbf{x}$, and σ_W is the standard deviation which enables to tune the selectivity of the filter. This permits to smooth the background without affecting the sharpness of the canaliculi and the cell lacunae are reconstructed.

6.4 Results

For the evaluation of the method we created a phantom simulating lacunae interconnected through canaliculi. We reproduced the feature sizes and the grey levels measured from the experimental data. The synthesized canaliculi have diameters of two and three voxels. The grey levels were set to 100 in the background and to 150 in the simulated structure. We added a zero mean Gaussian noise with a standard deviation of 18, similar to the noise estimated from the experimental images.

In order to find the optimal parameters tuning the 3D line filters described above (eq. 2-4), we performed systematic tests, starting from the values advised by the authors (Sato et al., 1998) (Frangi et al., 1998) and from the analysis presented in (Olabarriaga S.D. et al., 2003).

The selected parameters were $\alpha_1 = 0.5$, $\alpha_2 = 2$ for the filter in equation 2 and $a = 0.5$, $b = 0.5$, $c = 5$ for the filter in equations 3-4. The parameter tuning the scale of the sought features was set to $\sigma = 1$ for each of the line filters. The parameter σ_W was set to 10 and the size of the filter in equations 5-6 was 11.

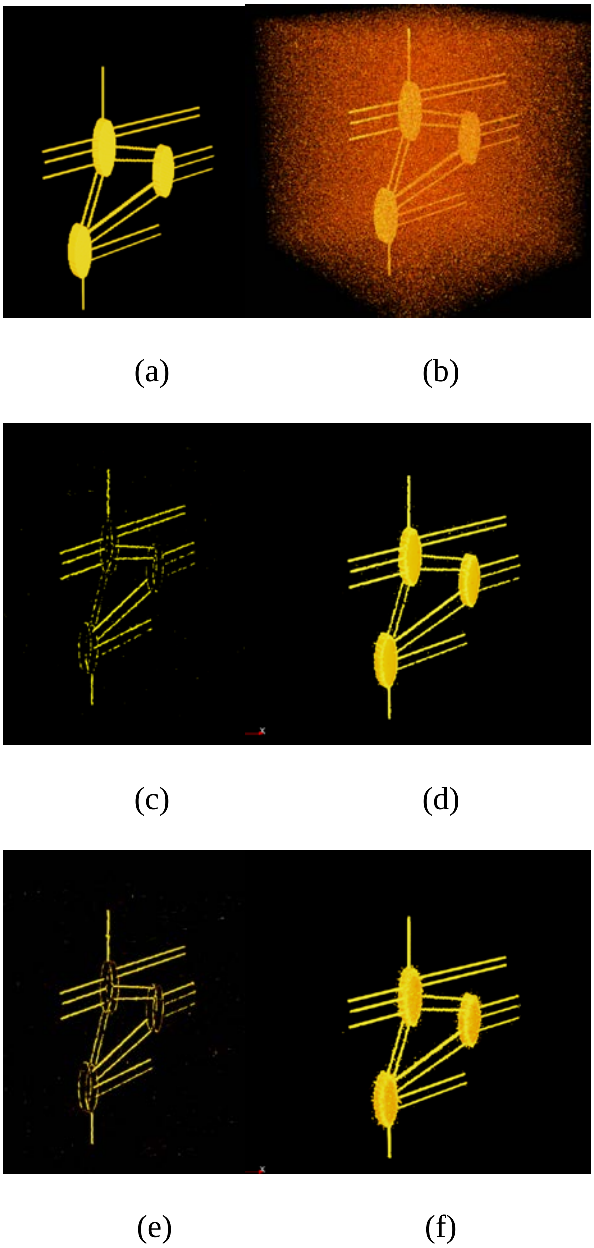

(a) (b)

(c) (d)

(e) (f)

Figure 44 Evaluation of a phantom a) original phantom; b) noisy phantom (Gaussian noise, σ=18); c) Output of the criterion proposed by Frangi d) Non-linear filtering based on Frangi's method ({$f_{NL}(x);I_S(x)$}) e) Output of the criterion proposed by Sato; f) Non-linear filtering based on Sato's method ({$f_{NL}(x);I_S(x)$}).

The resulting image was then segmented by thresholding and the percentage of well detected voxels was evaluated. Figure 44a,b show 3D renderings of the reference and the noisy images of the phantom. Figure 44c, illustrates the filter outcome obtained with the criterion from eq. 3-4 and Figure 44d shows the result obtained with the proposed non-linear method, using this filter map. Figure 44e and 43f show respectively, a rendering of the filter map obtained with the criterion from eq. 2 and after including this map in the non-linear approach.

By using the criterion l_F, we could detect 76% of the simulated canaliculi, and when applying the criterion l_S we retrieved 94% of the canaliculi. If the evaluation is made on the cell network (including lacunae), we detected 94% of the structure with $\{f_{NL}(\mathbf{x});l_S(\mathbf{x})\}$ (31% with $l_S(\mathbf{x})$ simple) and we retrieved the same percentage, 94%, with $\{f_{NL}(\mathbf{x});l_F(\mathbf{x})\}$ (17.4% with $l_F(\mathbf{x})$ simple). Whereas the quantitative evaluation gives similar results for the proposed filter, based on the $l_S(\mathbf{x})$ criterion or on the $l_F(\mathbf{x})$ measure, from the Figure 44d,f it can be observed that the integrity of canaliculi is better preserved when using $\{f_{NL}(\mathbf{x});l_S(\mathbf{x})\}$.

Application to experimental data

The same parameters were used on the experimental images. We show below the results obtained for a 256×256×256 sub-volume extracted from the original images. Figure 45a and Figure 45b respectively show 3D renderings of the resulting image after applying the criterion l_S and after non-linear filtering based on l_S. Figure 45c illustrates a detail in the last image showing that despite the complexity of the network, the connectivity seems to be well preserved. The total computation time for a volume of $(256)^3$ voxels was about 10 minutes. Figure 45d illustrates the result in a different region of interest.

6.5 Conclusion

The advances in X-ray micro CT open perspectives for the evaluation of biological tissue at the cellular scale. Direct, three-dimensional evaluation with isotropic spatial resolution becomes possible. Conversely to confocal microscopy, micro CT images are characterized by an isotropic voxel, which eliminates the distortions introduced by inhomogeneous resolution. However, at this scale, the image quality is limited and specific image processing methods have to be developed to detect sub-micrometric structures. Here, we proposed a non-linear filtering method to enhance the detection of tubular structures in noisy images. The results are demonstrated on experimental images showing the density and complexity of this network.

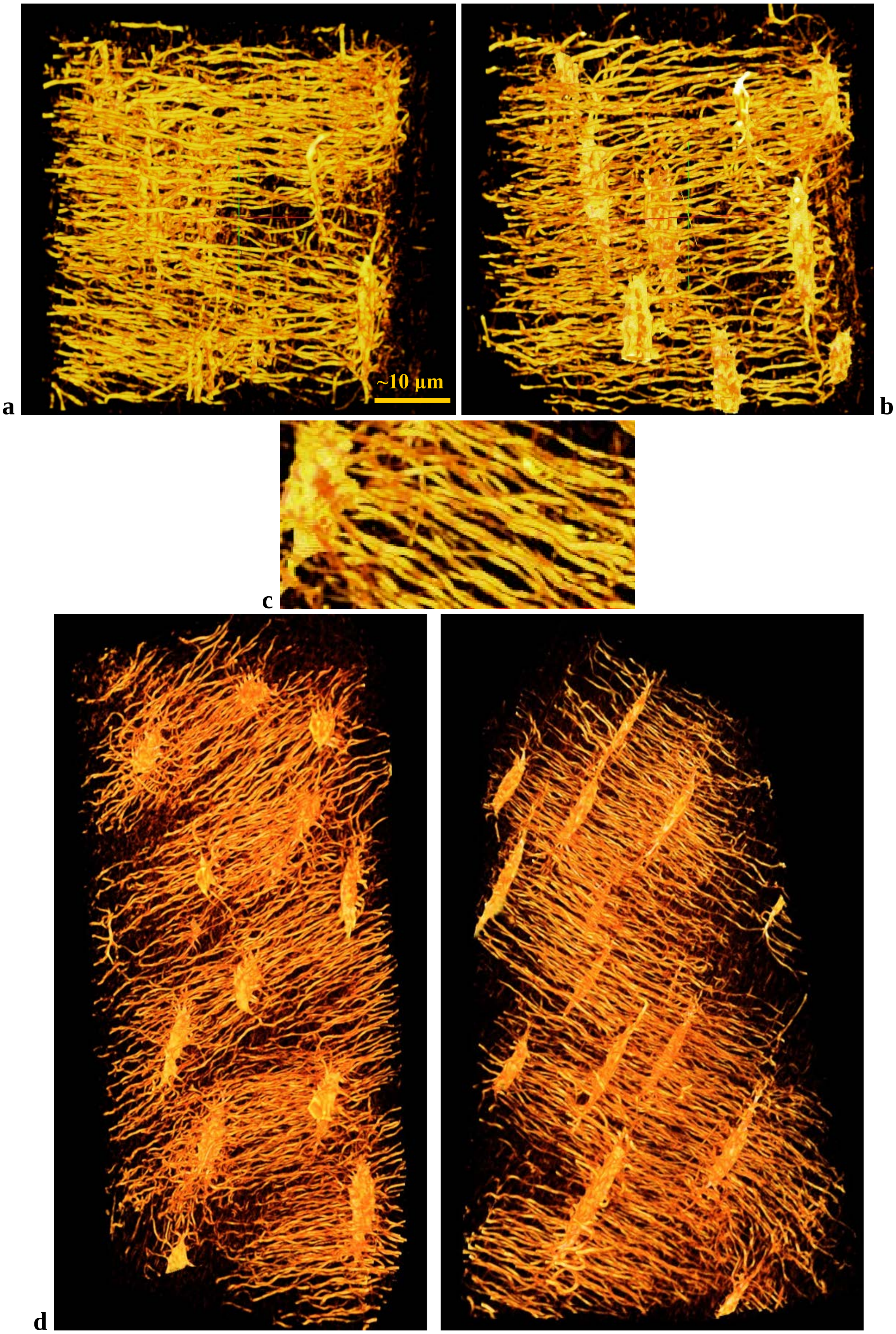

Figure 45 Volume of interest showing the lacuno-canalicular system in a human osteoporotic bone sample (image width ~70 µm) : a) 3D rendering after Sato filtering b) 3D rendering after Sato and non-linear filtering; c) Detail from figure (b) (image width ~20 µm). d) A different region.

The criterion for 3D line detection proposed by Frangi removes efficiently the background noise but it creates gaps within canaliculi. On the other hand, the method proposed by Sato preserves the connectivity of the structure but some background noise remains in the filtered image. When we apply the proposed non-linear filter, most of the background noise is removed. Therefore, for our case, the criterion proposed by Sato is better suited because it helps to keep the integrity of the canaliculi.

The proposed non-linear filter preserves the sharpness and integrity of the canaliculi provided by the 3D line filter, reconstructs the cell lacunae which are eliminated by the line filter, and removes most of the background noise. This enables the 3D visualization of the cell network in the experimental images. While the output of the filter can be used to obtain segmentation of the structure by thresholding, the result of the segmentation is affected by residual background noise, which is due to the inhomogeneity of the bone matrix, given by the composite.

A method of segmentation overcoming this problem is presented in the next chapter.

Chapter 7

A variational region growing approach for segmentation of the 3D bone cell network from nanoscale CT images

Alexandra Pacureanu, Jean-Loïc Rose, Chantal Muller, Françoise Peyrin
Manuscript prepared for Medical Image Analysis

7.1 Introduction

Bone is a dynamic tissue which is capable to repair, adapt and maintain itself. Due to its hierarchical organization, it can detect macro and micro lesions and replace the damaged tissue. At the micro and nano scales, a recurrent remodeling process permits the local maintenance of tissue quality. The mechanism governing this process remain poorly understood. In the last decades, studies revealed the central role of the osteocyte network (Bonewald, 2011) in controlling the remodeling process. This cell network is embedded in the mineralized bone matrix where it inhabits the lacuno-canalicular porosity, which represents its imprint. The architecture of this network reflects the tissue turnover and possibly its pathological state (Elisabeth H. Burger & Jenneke Klein-Nulend, 1999) (Knothe Tate et al., 2004).

The 3D assessment of the lacuno-canalicular network is essential for better understanding bone fragility and for advances in bone diseases management. Due to limiting factors in imaging and image analysis, this has not been achieved in a comprehensive way so far. The existing studies are based mainly on 2D data sets, analyzed manually on a reduced number of cells (<100). Advances in synchrotron radiation tomography at the nanoscale enabled recently imaging of the bone cell network in 3D with a field of view covering up to 4000 cells. This created unprecedented data which needs to be segmented and quantified to obtain biomedical conclusions. Considering that each cell lacuna has about 50-100 slender interconnecting canaliculi and that each image contains thousands of cell lacunae, a manual segmentation becomes unfeasible. Therefore, an automatic segmentation method suited to extract a complex cell network from 3D images affected by noise, feeble contrast and partial volume effects is necessary.

-

Image segmentation aims to determine a partition of the image into a set of regions corresponding to a set of sought structures. These regions can be distinguished based on specific properties such as uniformity with respect to the grey levels or to geometric characteristics. Two major approaches can be identified among the segmentation methods. One of them is based on similarity between the image elements within the objects to separate, and the second exploits the gradient of the image intensity localized on the objects boundary. The first approach gave rise to the region based methods while the second one determined the development of contour based techniques. However, the segmentation methods evolved towards a combination of the information describing regions and contours.

Many of the methods used and developed today are relying on the propagation of a contour, guided by the minimization of a functional which is fitted to the targeted structure. Starting from the “snakes” model (Kass et al., 1988) and the “level sets” approach (Osher & Sethian, 1988) proposed in the 1980s, several schemes for computing vision have been derived, seeking to improve performance and computation speed (Caselles et al., 1995) (Malladi et al., 1995) (J. A Sethian, 1995).

The propagation of the contour started to be driven by both boundary and region-based forces, in addition to be constrained by a regularization term (Zhu & Yuille, 1996) (Chakraborty et al., 1996) (Paragios et al., 1999) (Chan & Vese, 2001) (Yezzi et al., 2002) (Hernandez & Frangi, 2007). By using statistical region descriptors, the methods become more robust to noise.

Challenges

The main difficulties in segmenting the osteocyte network arise from the size of canaliculi which appear as thin linear structures occupying only one or few voxels in diameter. The nominal spatial resolution of the imaging system is 280 nm and the size of canaliculi in human bone, reported in the literature, varies between 200 and 900 nm. The performance of the detector is a limiting factor for the spatial resolution and the constrains imposed by the sensitivity of biological samples to radiation dose, affect the image quality in terms of signal to noise ratio (SNR). In consequence, in our segmentation task we have to deal with reduced SNR, partial volume effect and low contrast. To this, we have to add the high level of complexity of the three-dimensional cellular network combined with the large dimension of the images: 2048×2048×2048 voxels, corresponding to 8GB if the data is coded in unsigned char. Since in each image there are two to four thousands of cell lacunae and more than 100.000 canaliculi (value estimated based on information available from histological studies), a manual segmentation can not be considered.

Since 3D images of the LCN covering a large field of view were not available before, the inherent characteristics of this cell network create a new segmentation problem.

Contributions

Here we propose a technique to segment automatically the bone cell network from 3D synchrotron CT images at the nanoscale. The method is based on region growing, in a variational framework. We define the variational approach in the context of region growing and propose two energy functionals, adapted for the cell network. The designed energies take into account the local geometry and the intensity information. We describe a discrete algorithm for the evolution of this energy. We compare the proposed method with related segmentation techniques from literature.

For the evaluation of the segmentation results, we use both a synthetic phantom and a ground truth. The phantom simulating lacunae and canaliculi permits a qualitative assessment of the performance of the techniques. The quantitative assessment is done on a ground truth image extracted from an experimental volume.

The region-based variational approach described here can be directly used to minimize various energies leading to segmentation of different types of objects.

7.2 Methods

Variational region growing

Let $f(\mathbf{x})$ be a $3D$ image defined on Ω, a subset of $\Re^3$. We represent the evolving region through a characteristic discrete function $\varphi_{\mathbf{x}}$ defined as:

$$\varphi_{\mathbf{x}} = \varphi(\mathbf{x}) = \begin{cases} 1, & if \ \ \mathbf{x} \in \Omega_{in} \\ 0, & if \ \ \mathbf{x} \in \Omega_{out} \end{cases} \quad (1)$$

where $\mathbf{x} = (x, y, z)$ is an element of the image domain Ω.

The domain Ω_{in} is the subset representing the segmented region in Ω and $\Omega_{out} = \Omega \setminus \Omega_{in}$ is defined as the absolute complement of Ω_{in}.

The segmentation by variational region growing aims to reach the desired image partition by switching the discrete function $\varphi_{\mathbf{x}}$, in order to minimize a functional which models the structure to detect. This functional should describe the sought object and it should be designed in such a way that its minimum corresponds to the solution of the segmentation. In computer vision, this type of functionals are usually referred to as energies to minimize, a term inspired from physics.

In our segmentation approach, the energy functional, noted $J(\varphi)$ is region-based (Rose et al., 2010). The segmentation result can be then expressed as:

$$\varphi_{\mathbf{x}}^m = \arg\min_{\varphi_{\mathbf{x}}} J(\varphi_{\mathbf{x}}) \quad (2)$$

where $\varphi_{\mathbf{x}}^m$ is the optimal partition of the image, given by the minimization of the energy functional $J(\varphi_{\mathbf{x}})$. In order to find the solution, one can define the time-dependent variation of $\varphi_{\mathbf{x}}$, noted $\Delta_t \varphi$, and estimate the evolution of the energy for a small alteration of $\varphi_{\mathbf{x}}$, noted $\tilde{\varphi}$:

$$\Delta_t \varphi + F(\varphi_{\mathbf{x}}, \Delta J(\tilde{\varphi})) = 0 \qquad (3)$$

where $F(\varphi_{\mathbf{x}}, \Delta J(\tilde{\varphi}))$ is a functional controlling the region evolution.

In the formulation of the functional $F(\varphi_{\mathbf{x}}, \Delta J(\tilde{\varphi}))$ we introduce a function $c(\varphi)$, which determines the switch of $\varphi_{\mathbf{x}}$:

$$c(\varphi) = 1 - 2\varphi_{\mathbf{x}} \qquad (4)$$

We define therefore the function which governs the region propagation as:

$$F(\varphi_{\mathbf{x}}, \Delta J(\tilde{\varphi})) = -c(\varphi) \cdot H(-\Delta J(\tilde{\varphi})) \quad (5)$$

in which *H* stands for the one dimensional Heaviside function:

$$H(z) = \begin{cases} 0 & if\ z < 0 \\ 1 & if\ z \geq 0 \end{cases} \quad (6)$$

The Heaviside function switches on the function $c(\varphi)$ when the energy variation is negative and conversely, it is calling $c(\varphi)$ off when the energy variation is positive.

The initialization of the segmentation ($t = 0$) can be defined as:

$$\varphi^0 = \{\mathbf{x} \in \Omega \mid \varphi(\mathbf{x}, t = 0) = 1\} \quad (7)$$

In the discrete case, the equation (3) is solved iteratively by numerical methods starting from φ^0. The values of the function φ at the iteration *n+1* are evaluated in each point as follows:

$$\varphi_{\mathbf{x}}^{n+1} = \varphi_{\mathbf{x}}^{n} + c(\varphi_{\mathbf{x}}^{n}) \cdot H(-\Delta J(\tilde{\varphi}_{\mathbf{x}}^{n})) \quad (8)$$

Depending on the sign of $\Delta J(\tilde{\varphi}_{\mathbf{x}}^{n})$, the value of $\varphi_{\mathbf{x}}$ is switched or it remains unchanged. The evolution stops when $\varphi_{\mathbf{x}}$ does not encounter modifications in any of the assessed points.

Definition of the vicinity to assess

At each iteration, only a limited set of voxels are evaluated for possible aggregation. These voxels are selected by defining a vicinity which surrounds the boundary of the segmented region. The size of the neighborhood is set based on the Euclidian distance. We can define the vicinity of size ε of a point u as the set:

$$W_{\varepsilon}(\mathrm{u}) = \{v \in \Omega \mid \|v - u\| \le \varepsilon\} \quad (9)$$

The set of elements tested at each iteration represent the outer border of the segmented region, Ω_{in} and can be obtained as:

$$\partial_{\varepsilon} = \{v \in \Omega_{out} \mid \exists u \in \Omega_{in},\, v \in W_{\varepsilon}(u)\} \qquad (10)$$

For the implementation of the algorithm, we use the function $c_{\varepsilon}\left(\varphi_{\mathbf{x}}^{n}\right)$ to establish the vicinity of a given size ε, to be evaluated at the iteration *n*:

$$c_{\varepsilon}\left(\varphi_{\mathbf{x}}^{n}\right) = \begin{cases} 1 - 2\varphi_{\mathbf{x}}^{n} & if\ \mathbf{x} \in \partial_{\varepsilon} \\ 0 & otherwise \end{cases} \qquad (11)$$

Evolution of the energy functional

The minimization of the energy functional is based on the approach presented in (Jehan-Besson et al., 2002). Jehan-Besson et al. define a general expression of a region-based energy obtained from a “region-independent” descriptor $k_{\mathbf{x}}$ as:

$$J(\Omega_{in}) = \int_{\Omega_{in}} k_{\mathbf{x}} d\mathbf{x} \qquad (12)$$

Given the energy $J\left(\varphi^{n}\right)$ at the iteration *n*, we evaluate the energy $J\left(\tilde{\varphi}^{n}\right)$ which is the result of the aggregation of a candidate voxel **v.** In our discrete case, the expression of the energy becomes:

$$J(\varphi^{n}) = \sum_{\mathbf{x} \in \Omega} k_{\mathbf{x}} \cdot \varphi_{\mathbf{x}}^{n} \quad (13)$$

We assess the change of the status of a voxel *v* as follows:

$$\tilde{\varphi}_{v}^{n} = 1 - \varphi_{v}^{n} \quad (14)$$

which implies that: $\tilde{\varphi}_{\mathbf{x}}^{n} = \varphi_{\mathbf{x}}^{n} \quad if \quad \mathbf{x} \ne v \quad (15)$

From the relations (13), (14) and (15), the evaluated energy can be then written as:

$$J(\tilde{\varphi}^n) = k_v \cdot \tilde{\varphi}_{\mathbf{x}}^n + \sum_{\mathbf{x} \neq v,\, \mathbf{x} \in \Omega} k_{\mathbf{x}} \cdot \varphi_{\mathbf{x}}^n \qquad (16)$$

which is equivalent to:

$$J(\tilde{\varphi}^n) = k_v \cdot \left(1 - \varphi_v^n\right) - k_v \cdot \varphi_v^n + \underbrace{k_v \cdot \varphi_v^n + \sum_{\mathbf{x} \neq v} k_{\mathbf{x}} \cdot \varphi_{\mathbf{x}}^n}_{J(\varphi^n)} \qquad (17)$$

Therefore, the energy variation $\Delta J\left(\tilde{\varphi}_v^n\right)$, associated to a single voxel *v*, will have the following formulation:

$$\Delta J\left(\tilde{\varphi}_v^n\right) = \left(1 - 2\varphi_v^n\right) \cdot k_v \qquad (18)$$

This expression for the evolution of the energy functional is valid for any descriptor k_v.

Examples of energy functionals from the literature

In the literature, several region-based energies were introduced into the variational framework. Here we remind a few of them, which we tested on our data.

Chan and Vese proposed an energy based on the average calculated inside and outside the segmented region (Chan & Vese, 2001) :

$$J_{CV}(f) = \lambda_{\text{int}} \int_{\Omega_{in}} \left| f(\mathbf{x}) - \mu_{in} \right|^2 d\mathbf{x} + \lambda_{ext} \int_{\Omega_{out}} \left| f(\mathbf{x}) - \mu_{out} \right|^2 d\mathbf{x} \qquad (19)$$

Within our framework described above, the evolution of this energy can be expressed as following:

$$\Delta J_{CV}(\varphi^{n+1}) = \left(1 - 2\varphi^n\right)\left[\left| f - \mu_{in} \right|^2 - \left| f - \mu_{out} \right|^2\right] \qquad (20)$$

where μ_{in}, respectively μ_{out}, are the average grey levels of the domain Ω_{in}, respectively Ω_{out}.

Zhu and Yuille suggested a model based on probability distributions which can be particularized for the case of a Gaussian distribution (Zhu & Yuille, 1996):

$$J_{ZY}(f)=\int_{\Omega}-\log\left[\frac{1}{\sqrt{2\pi\sigma}}\exp\left(-\frac{\left|f(\mathbf{x})-\mu\right|^{2}}{2\sigma^{2}}\right)\right]d\mathbf{x} \qquad (21)$$

leading to the following expression of energy variation :

$$\Delta J_{ZY}(\varphi^{n+1})=-\left(1-2\varphi^{n}\right)\left(-\frac{\left|f-\mu_{in}\right|^{2}}{2\sigma_{in}^{2}}\right)-\left(-\frac{\left|f-\mu_{ext}\right|^{2}}{2\sigma_{ext}^{2}}\right) \qquad (22)$$

This energy can differentiate regions characterized by the same mean but with different variations.

Yezzi et al. proposed to take into account the area *A* of the region (Anthony Yezzi et al., 2002):

$$J_{YTW}(f)=\int_{\Omega_{in}}\frac{f(\mathbf{x})-\mu}{A}d\mathbf{x} \qquad (23)$$

Energy functionals proposed for the 3D cell network

In this section, we propose the expressions of two energy functionals based on region descriptors and shape information. The first one is related to the model proposed in (Chan & Vese, 2001) and the second one, to the approach presented in (Zhu & Yuille, 1996). We introduced in each functional information on the geometry of the structure to detect, extracted from the map of a 3D line enhancement filter.

The osteocyte cell network is essentially composed of ellipsoidal objects interconnected through tubular structures. The main difficulty in segmenting this formation arises from the slender canaliculi, the linear features occupying only a few voxels in diameter. We try to cope with these problems by exploiting the 3D line enhancement filter proposed by Sato (Sato et al., 1998), which yields a probability map of the tubular-like structures in the image. The filter can be tuned to enhance tubular features of a particular size.

The first proposed functional which is described below, combines knowledge on the mean grey level within and outside the segmented region. These values are extracted from both the original image and the filter map. Each term of the energy is weighted by the likelihood that the current element belongs to a canaliculus, which is given by the local result of the line filter. It can be expressed as:

$$J_A(f,l) = J_{Af}(f,l) + J_{Al}(l) \qquad (24)$$

where

$$J_{Al}(l) = \int_{\Omega_{in}} l(\mathbf{x}) \left| l(\mathbf{x}) - \mu_{l_{in}} \right|^2 d\mathbf{x} + \int_{\Omega_{out}} l(\mathbf{x}) \left| l(\mathbf{x}) - \mu_{l_{out}} \right|^2 d\mathbf{x} \qquad (25)$$

and

$$J_{Af}(f,l) = \int_{\Omega_{in}} (1 - l(\mathbf{x})) \left| f(\mathbf{x}) - \mu_{f_{in}} \right|^2 d\mathbf{x} + \int_{\Omega_{out}} (1 - l(\mathbf{x})) \left| f(\mathbf{x}) - \mu_{f_{out}} \right|^2 d\mathbf{x} \qquad (26)$$

where $l(\mathbf{x})$ is the 3D line similarity measure at the voxel $\mathbf{x}$ and $\mu_{l_{in}}, \mu_{l_{out}}$ (respectively $\mu_{f_{in}}, \mu_{f_{out}}$) are the average grey levels of the domains Ω_{in} and Ω_{out} in the 3D line map $l(\mathbf{x})$ (respectively in the original image $f(\mathbf{x})$).

The variation of the energy functional $J_A(f,l)$ can be expressed as follows:

$$\Delta J_A(\phi^{n+1}) = (1 - 2\phi^n)\left(\Delta J_{Al}(l) + \Delta J_{Af}(f,l)\right) \qquad (27)$$

where

$$\Delta J_{Al}(l) = l \left(\left| l - \mu_{l_{in}} \right|^2 - \left| l - \mu_{l_{out}} \right|^2 \right) \qquad (28)$$

$$\Delta J_{Af}(f,l) = (1 - l) \left(\left| f - \mu_{f_{in}} \right|^2 - \left| f - \mu_{f_{out}} \right|^2 \right) \qquad (29)$$

The output of the 3D line filter can be seen as a measure of the probability of each voxel to be part of a tube-like structure. It gives values in the interval [0,1]. During the segmentation evolution, when a tested voxel belongs to a canaliculus, the value of $l(\mathbf{x})$ is close to 1, therefore, the term $\Delta J_{Al}(l)$ in the equation (28), will be used. If the considered voxel is part of the background or of a lacuna, $l(\mathbf{x})$ will be close to 0 and the term $\Delta J_{Af}(f,l)$ will be employed, hence the information in the original image will be taken into account. This formulation permits to detect both lacunae and canaliculi and, by propagation on the line enhancement filter map, it makes possible to reconnect parts of the same canaliculus.

The second energy functional which we designed is based on a Gaussian probability distribution model, therefore the standard deviation is introduced as parameter. The 3D line filter is weighting the energy when the voxel tested for aggregation is likely not situated in a cell lacuna. The expression of the functional is:

$$J_B(f,l) = g(\mathbf{x})J_{Bf}(f) + [1 - g(\mathbf{x})]J_{Bfl}(f,l) \qquad (30)$$

with

$$J_{Bfl}(f,l) = \int_{\Omega_{in}} G_{in}(f,l)d\mathbf{x} + \int_{\Omega_{out}} G_{out}(f,l)d\mathbf{x} \qquad (31)$$

with

$$G_{in}(f,l) = \frac{1}{\sqrt{2\pi\sigma_{f_{in}}}}\exp\left(-\frac{\left|f(\mathbf{x}) - \mu_{f_{in}}\right|^2}{2\sigma_{f_{in}}^2 \, l(\mathbf{x})}\right) \qquad (32)$$

and

$$G_{out}(f,l) = \frac{1}{\sqrt{2\pi\sigma_{f_{out}}}}\exp\left(-\frac{\left|f(\mathbf{x}) - \mu_{f_{out}}\right|^2}{2\sigma_{f_{out}}^2 \left(1 - l(\mathbf{x})\right)}\right) \qquad (33)$$

and

$$J_{Bf}(f) = \int_{\Omega_{in}} \left|f(\mathbf{x}) - \mu_{f_{in}}\right|^2 d\mathbf{x} + \int_{\Omega_{out}} \left|f(\mathbf{x}) - \mu_{f_{out}}\right|^2 d\mathbf{x} \qquad (34)$$

and

$$g(\mathbf{x}) = \begin{cases} 0 & if \quad f(\mathbf{x}) < \delta \\ 1 & if \quad f(\mathbf{x}) \geq \delta \end{cases} \qquad (35)$$

where δ is a threshold value.

The variation of the energy functional $J_B(f,l)$ can be expressed as follows:

$$\Delta J_B(\phi^{n+1}) = (1-2\phi^n)\left(\Delta J_{Bf}(f) + \Delta J_{Bfl}(f,l)\right) \qquad (36)$$

with

$$\Delta J_{Bf}(f) = \left|f - \mu_{f_{in}}\right|^2 - \left|f - \mu_{f_{out}}\right|^2 \qquad (37)$$

and

$$\Delta J_{Bfl}(f,l) = \frac{1}{\sqrt{2\pi\sigma_{f_{in}}}} \exp\left(-\frac{\left|f-\mu_{f_{in}}\right|^2}{2\sigma_{f_{in}}^2 l}\right) - \frac{1}{\sqrt{2\pi\sigma_{f_{out}}}} \exp\left(-\frac{\left|f-\mu_{f_{out}}\right|^2}{2\sigma_{f_{out}}^2 (1-l)}\right) \qquad (38)$$

Initialization of the segmentation

The starting point of the segmentation is given as a 3D binary image. We tested several approaches for the generation of the segmentation germs. The desired initialization method should be automatic, it shouldn’t create false positive germs and it should help the segmentation algorithm to find the optimal solution in as little iterations as possible, thereby saving computation time.

One of the simplest ways to obtain the initialization image is by applying a very selective threshold on a slightly blurred version of the input image. In our case the chosen value of the threshold would be 254, as in the images rescaled to unsigned char, the voxels in the cell lacunae have the value 255 in quite large proportion, whilst in the rest of the image this value is hardly present. A Gaussian mask of size one is sufficient to eliminate noise points of value 255, if they exist in the image.

The initialization method yielding the best segmentation results was based on the 3D line filter map. By thresholding the filter map image, we obtain portions of canaliculi.

Figures of merit

For quantitative assessment of the segmentation methods, we evaluated several parameters. These are the Dice’s coefficient, the precision of the method with respect to over-segmentation and under-segmentation, and the level of connectivity of the structure. These metrics are defined as follows:

$$DICE = \frac{2|R \cap S|}{|R| + |S|} \qquad (36) \qquad\qquad Err_{cc} = \frac{cc_S - cc_R}{cc_R} \qquad (37)$$

$$P_{-} = \frac{|R \cap S|}{|R \cap S| + |R - S|} \qquad (38) \qquad\qquad P_{+} = \frac{|R \cap S|}{|R \cap S| + |S - R|} \qquad (39)$$

where R, S are the sets of voxels belonging to the targeted structure in the ground truth volume and respectively in the segmented volume. The notations cc_S and cc_R stand for the number of connected components retrieved in the reference image and in the segmented image.

7.3 Experiments

Image acquisition

Image acquisition was performed at the ID19 experimental station at the European Synchrotron Radiation Facility (ESRF), Grenoble, France. The experimental hutch is located at a long distance from the source (145m), permitting to obtain a truly 3D parallel beam CT set-up. X-rays were generated with an undulator yielding very high flux with a spectrum distributed in narrow bandwidths and a monochromatic X-ray beam was selected with a single-bounce multilayer. The detector was composed of a scintillator converting X-rays to visible light, a magnifying optic system and a cooled charge-coupled device (CCD) camera. The effective pixel size was 280 nm giving a field-of-view of 574 µm. The sample-to-detector distance was set at 11 mm in order to obtain propagation based phase contrast which enhances the visibility of interfaces, hence the visibility of canaliculi. The sample was rotated over 180° and 2000 angular projections were recorded. The 3D images were obtained from the projection images by applying a 3D version of the filtered backprojection algorithm. The reconstructed images measure 2048×2048×2048 voxels.

The spatial resolution of the system is on the same range as the canalicular diameter, hence the slender channels occupy only one or two voxels in the 3D reconstructed images.

Imaged samples

The specimens were extracted from the mid-diaphysis of human femur and underwent a treatment consisting of supercritical carbon dioxide for delipidation, chemical bath and gamma irradiation for sterilization (Biobank, Presles en Brie, France). Ethical approval for the samples was granted by the Human Ethics Committee of the Centre du don des Corps at the University René Descartes (Paris, France). The tissue donors or their legal guardians provided informed written consent to donate their tissue for investigation, in accord with legal clauses stated in the French Code of Public Health. Small parallelepiped samples (0.5mm x 0.5mm x 10mm) were then cut with a diamond saw for imaging.

7.4 Results

Tuning the parameters

For the parameters of 3D line filter, results reported in (Sato et al., 1998) (Olabarriaga S.D. et al., 2003) were used as starting point for tuning. Several tests have been performed and the filter parameters were set to $\sigma=1$, $\alpha_1=0.5$, $\alpha_2=2$. For the variational region growing, the size of the neighborhood for each energy functional has been set based on tests performed on the volume for which a ground truth has been prepared. The metrics used for the algorithm validation have been computed in order to find the optimal parameters. The size of the vicinity was set to 2, for all the energy functionals.

Evaluation on a synthetic phantom

For the evaluation of the segmentation we prepared a synthetic phantom and a ground truth. The 3D synthetic phantom (100×100×50 voxels, unsigned char) simulates three cell lacunae and canaliculi. The thickness of canaliculi varies between one and three voxels and some small interruptions have been created purposely.

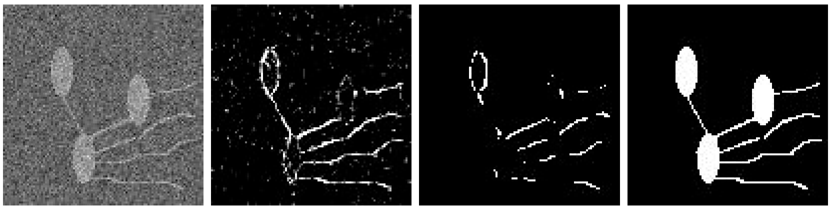

Figure 46 Slices in the designed phantom a) Input image b) Filter map c) Initialization d) Reference

Following measurements in the experimental images, the grey level of the background was set to 100 and inside the simulated cell network to 150. Random noise with a Gaussian distribution of standard deviation 18 was added, corresponding to the noise evaluated in the acquired images. Figure 46 shows a slice in the designed phantom (a), as well as the corresponding slices in the 3D line filter map (b), in the initialization image (c) and the reference image (d).

The procedure for the segmentation was identical with the one used on the real data in terms of preprocessing, initialization method, parameters for the filter and for the segmentation.

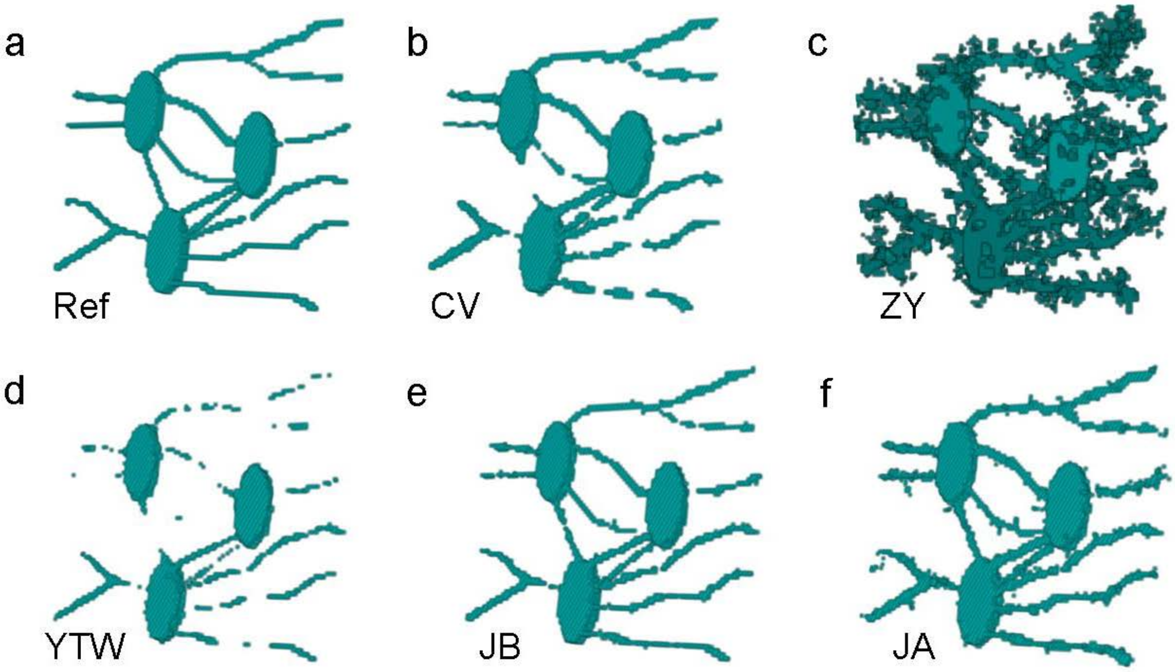

Figure 47 Results on the synthetic phantom a) Reference b) CV c) ZY d) YTW e) JB f) JA

Figure 47 illustrates 3D renderings of the segmentation results with each method, as well as the ideal segmentation. This facilitates the qualitative analysis of the segmentation methods performance.

It can be observed that YTW does not propagate enough in the simulated canaliculi and ZY propagates too much. CV achieves a better segmentation but several gaps are created in the slender structures and it has the tendency to thicken the canaliculi. JB yields a more accurate segmentation in terms of structure thickness but a few small disconnections are present. JA also tends to thicken the fine 3D lines but it keeps a good connectivity, attempting even to refill very small gaps existing in the original image.

In Figure 48 are rendered the segmentation results superimposed over the ideal segmentation result. The patches that appear in yellow/green correspond to portions of the object which the segmentation failed to detect.

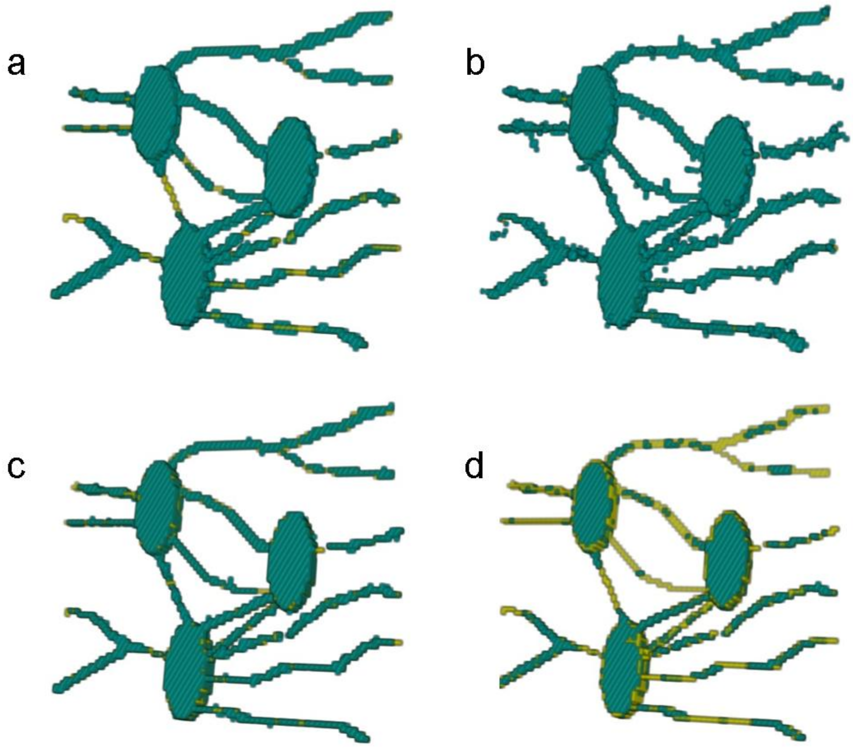

Figure 48 Figure Results on the synthetic phantom – superimposed with ideal segmentation for evaluation. a) CV b) JA c) JB d) YTW. One can observe that CV does not propagate in some regions of the tubular structures, creating disconnections. JA achieves the best connectivity and coverage of the ideal structure, but it creates some false positive detections on the surface of the object. JB yields a better coverage comparing to CV but somewhat less good that JA. While it keeps the object surface smooth, the resulted disconnections are undesirable. YTW can only detect a part of the object.

Evaluation on ground truth

For a quantitative analysis of the segmentation results we prepared a ground truth image extracted from an experimental volume (256×256×256 voxels). The reference image was obtained by manual segmentation. The figures of merit presented in section 7.3 were assessed. The quantitative results of the segmentation methods appraisal are in agreement with the results observed on the synthetic phantom. One can observe that the best results in terms of connectivity level are given by the JA (Table 1). This method detects 97% of the structure but, because it tends to broaden the canaliculi, the precision for over-detection is not as good.

Comparing to CV, JA improves the segmentation with respect to each metric, with the exception of the over-detection, which is similar. The considerable improvement in terms of connectivity is rather important for our particular data. We added the comparison with the level sets method, as proposed in (Caselles et al., 1995) and (Sethian, 2000). This was applied with the parameters presented in **Annex I**, starting from the same initialization as for the variational region growing. The evaluation shows that while it gives fairly good with respect to outflow from the targeted object, it does not achieve a very good connectivity of the network.

	Error CC (%)	**Dice (%)**	**Precision over-detection (%)**	**Precision under-detection (%)**
YTW	288	74	100	59
ZY	18	56	39	96
CV	57	75	63	93
JB	21	79	67	96
JA	11	77	63	97
LS	218	75	72	78

Table 1 Quantitative results of the segmentation evaluation. YTW – Yezzi; CV – Chan and Vese; JB – proposed energy A; JA – proposed energy B; LS- level sets (Caselles, Sethian)

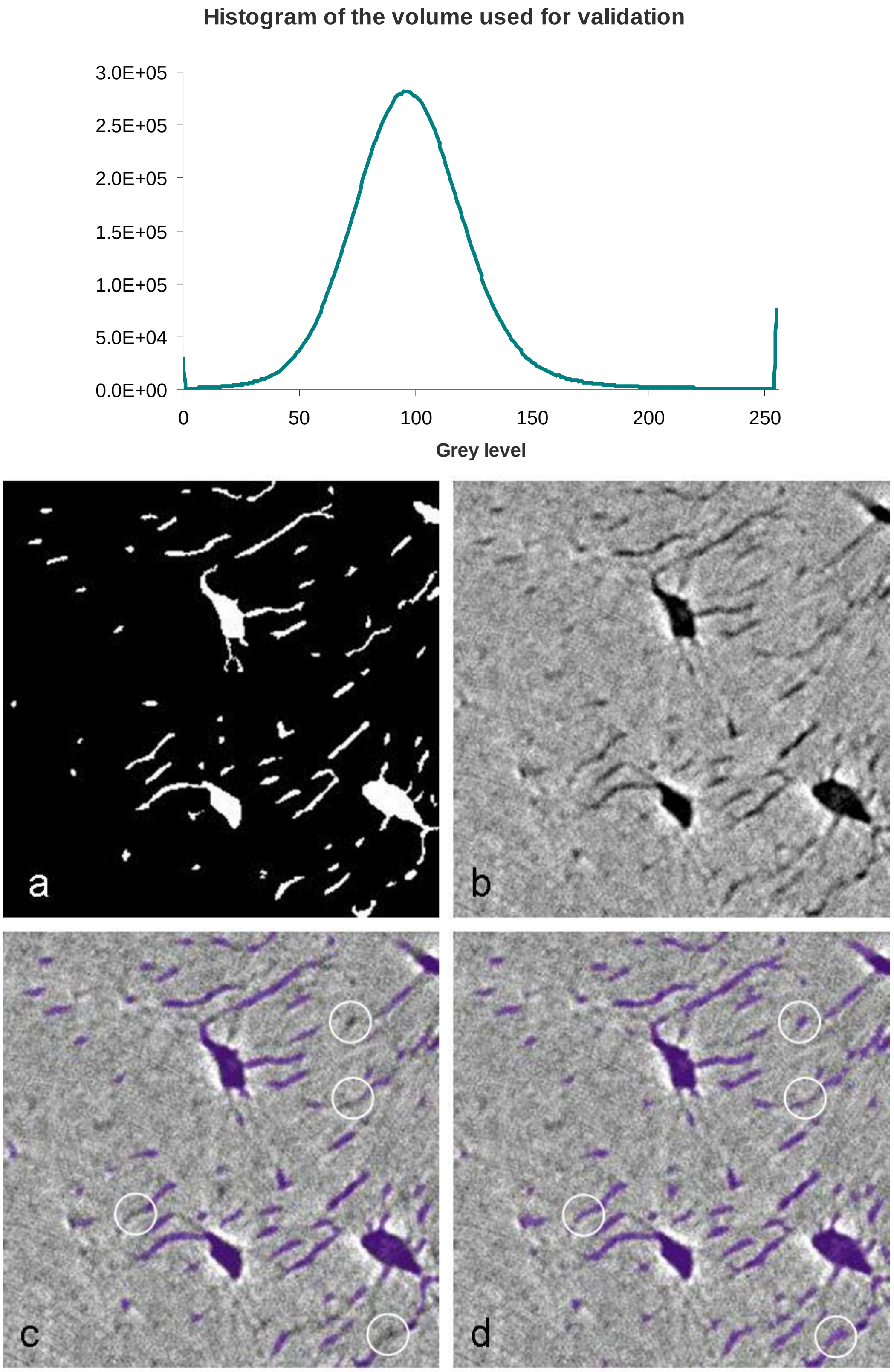

Figure 49: Histogram and slices from the volume of interest used for validation a) Ground truth b) Original data c) Segmentation result with LS overlaid over original image d) Segmentation result with JA overlaid over original image. Circles indicate regions where JA propagated and LS did not.

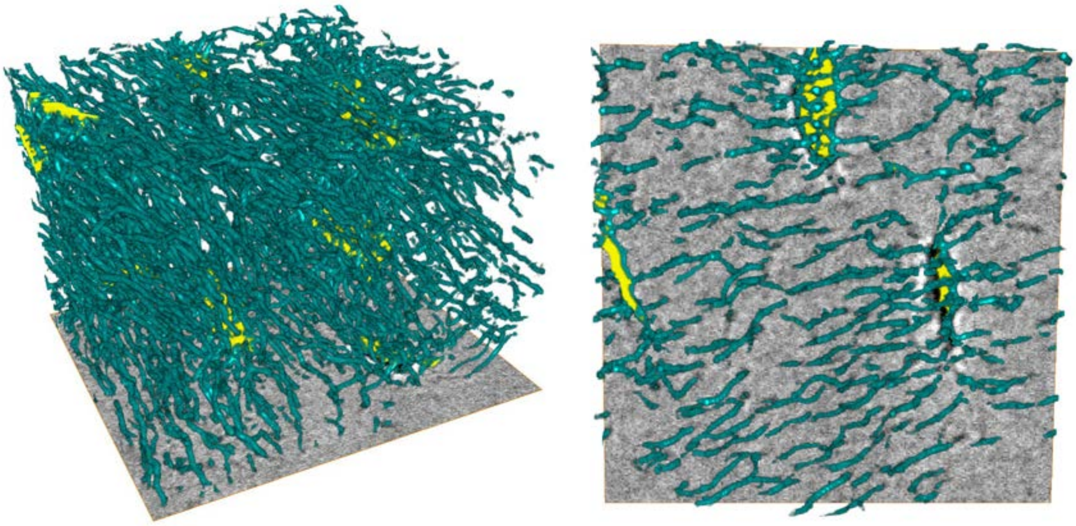

Figure 50 Three-dimensional renderings of the segmentation result (JA) in the volume for which a ground truth was prepared (256^3 voxels ↔ ~ 72^3 µm^3). For visualization reasons, the cell lacunae have been segmented separately by manually selected thresholding and rendered in a different color (yellow).

Figure 50 shows 3D renderings of the segmentation result obtained when using the energy functional JA, on the region of interest used for validation. Figure 51 illustrates the result of the segmentation with JA on a larger volume, extracted from the experimental data. In order to facilitate the visualization, the cell lacunae and the vessel canals have been segmented also separately and assigned a different color map.

Implementation of the method

The algorithms have been implemented in C++ language using the ITK library (Kitware). The calculation time for an input image of 256^3 voxels was 30 seconds when using YTW energy (3 iterations), 1’10” (22 iterations) when using CV energy, 2’30” (39 iterations) with the JA energy, 2’40” with JB (22 iterations) and 21 minutes for the level sets approach. For an input image measuring 1600x1000x256 voxels the calculation time was 55 minutes (49 iterations) with CV and 73 minutes (49 iterations) in the case of JA. For this size of the input image (391 MB), the allocated dynamic memory was about 22 GB.

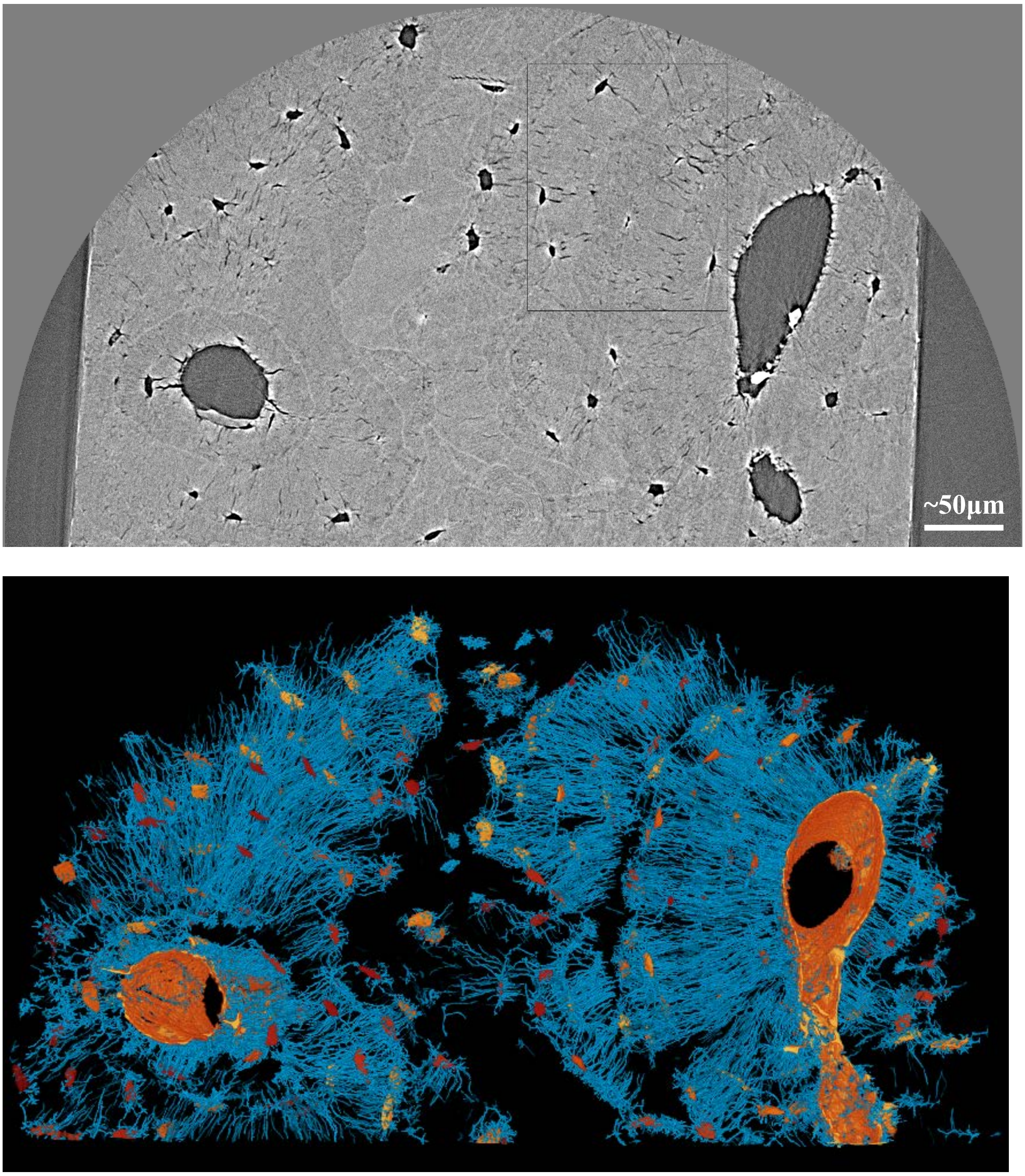

Figure 51 Three-dimensional volume rendering showing the result of the segmentation on a volume of interest measuring 1500×1800×256 voxels. The cell lacunae (yellow to red) and the vessel canals (orange) have been segmented separately by manually selected thresholding followed by connected components analysis (Hoshen & Kopelman, 1976). For visualization, the segmented image has been used as a mask on the line filter map, thereby the rendered canaliculi have different grey levels.

7.5 Discussion and conclusions

Due to the inherent characteristics of the bone cell network a manual or even interactive segmentation approach are not feasible, especially when a single image contains thousands of cell lacunae and at least a hundred thousands canaliculi. Therefore, an automatic segmentation method is imposed. We proposed here two methods based on active regions, which permit to achieve a rather good segmentation of the cell network, with a high level of connectivity.

Inspired from two energy functionals found in the literature, we proposed new expressions adapted for the cell network, which include geometrical information on the object to detect. The regularization term acting on the length or curvature of the region boundary was omitted because it would stop the propagation in the regions where canaliculi connect to the cell lacunae.

The criterion controlling the regions propagation based on the inner and external averages in the evolving components yields the best results in terms of connectivity. The validation of the method shows that almost the entire structure is detected, but some voxels connected to the structure but not necessarily belonging to it are attached. However, the individuality of the canaliculi is conserved, i.e. two parallel neighboring canaliculi are not erroneously connected. This means that an automatic quantification can be accurate for the number of canaliculi per lacuna or for the evaluation of the level of connectivity of the network for example. On the other hand, when quantifying the volume occupied by the canalicular porosity one should correct it down, taking into account the over-segmentation.

The functional based on both average and standard deviation inside and outside the segmented regions and weighted by the line filter, is more robust to noise, gives a decent connectivity and the precision for over-segmentation is improved. However, due to the gaps left in some of the canaliculi, the connectivity of the network is underestimated. This method is more appropriate for images more severely affected by noise, when the previous criterion may retain voxels from the background.

Comparing to the contour-based level sets approach, the active regions method seems to be better suited for our case, yielding a more accurate segmentation with less computational costs.

Chapter 8

Quantitative 3D imaging of the human bone lacuno-canalicular network with synchrotron radiation computed tomography

Alexandra Pacureanu , Max Langer , Cécile Olivier, Quentin Grimal, Françoise Peyrin

Manuscript submitted to Bone

Abstract

The osteocytes are spread throughout the bone matrix and they are interconnected by a complex dendritic network. These properties indicate their potential function as mechanosensory cells. Due to recent results suggesting the major role of the osteocyte lacuno-canalicular network in mechanotransduction and bone remodeling, a need to study this system has arisen. However, comprehensive assessment of this cell network has remained unachievable due to limitations of the investigation techniques. Here we propose a new technique, parallel beam synchrotron computed tomography, to image in three dimensions (3D) this cellular network. Combining nanoscale spatial resolution and large field of view, the method provides the first 3D quantitative images of the osteocyte network covering both osteons and interstitial tissue. The technique is reproducible, relatively fast and does not rely on special specimen preparation. This method enables direct measurements of 3D morphological parameters as well as evaluation of the degree of mineralization in the surrounding bone matrix. We present unparalleled visualizations of the lacuno-canalicular network in human cortical bone tissue covering several osteons. The cell network appears dense and well organized in the osteons, while in the interstitial tissue the cell lacunae are isolated and sparse. This

tool can be used for the assessment of the tissue quality at sub-micrometric scale and it facilitates realistic estimation of aspects of bone physiology. For instance, the accurate 3D data represents a valuable input for the study of the bone fluid flow through the osteocyte lacuno-canalicular system. We foresee that this investigation method will enhance understanding of bone fragility and contribute to new perspectives in diagnosis and treatment of bone diseases.

8.1 Introduction

Bone tissue is strong, yet light, it combines stiffness and elasticity and is capable to maintain itself. With a multiscale hierarchical organization, bone has the ability to detect and repair micro and macro damage and to adapt to external mechanical loads, through a permanent remodeling process (Huiskes et al., 2000) (Taylor et al., 2007). When various factors disturb the remodeling process, the balance between tissue resorption and formation is lost and the bone architecture is deteriorated. The consequence is weakened connective structures giving rise to bone fragility and ultimately failure. Better understanding of the mechanisms controlling bone remodeling is fundamental for advancement in treatment of bone diseases.

The remodeling process is likely regulated by the osteocytes, which are the most abundant cells in the bone cortex (Bonewald, 2011) (Burra et al., 2010). They reside in lacunae formed around the nascent osteocytes where they are trapped during bone matrix deposition, and communicate through dendritic processes hosted in canaliculi. The lacuno-canalicular network (LCN) allows transport of signals, nutrients and waste through the mineralized bone matrix. The architecture of this network is correlated with the remodeling process and with tissue quality (Elisabeth H. Burger & Jenneke Klein-Nulend, 1999) (Kerschnitzki et al., 2011) (Melissa L. Knothe Tate et al., 2004). The nanometric size of canaliculi (200-900 nm in diameter) combined with the complex three dimensional (3D) organization of the LCN and its situation inside a solid matrix, restricted previously the exploration (Schneider et al., 2010). Here we present a non-destructive, truly 3D imaging method that enables quantitative analysis of the LCN with a large field of view (up to 4000 cells), which is based on parallel beam synchrotron radiation nano-tomography. The technique is reproducible, relatively fast and does not require special specimen preparation. This method enables automatic evaluation of quantitative architectural parameters as well as measurements of degree of mineralization in the surrounding bone matrix.

The investigation of the osteocyte network has been done mainly in 2D, using optical or electron microscopes. Confocal microscopy can produce 3D images of the LCN (Sugawara et al., 2005), but the data is distorted by the anisotropic resolution and limited by the restricted depth of field, caused by low penetration of visible light in bone tissue. Recently, truly 3D imaging techniques reaching resolutions of tens of nanometers have been reported (Dierolf et al., 2010) (Stokes et al., 2005) (Schneider et al., 2011). While these methods enable precise visualization covering one to three lacunae, their reduced field of view makes unfeasible a comprehensive characterization of the LCN considering that in a single osteon, which is the elemental functional unit of bone cortex, there are hundreds or thousands of cells. In addition, these methods impose destructive and tedious sample preparation or long imaging duration (~24 hours per scan).

X-ray micro-tomography has proven to be a valuable imaging technique making possible non-destructive 3D exploration of the internal structure of materials at micrometric scale, and it is now widely used in biomedical imaging (Muller, 2009). The elevated brilliance of synchrotron X-ray sources permits to use a high flux monochromatic beam, giving access to quantitative images at sub-micrometric spatial resolution while maintaining short acquisition times. Synchrotron tomography (SR-CT) has demonstrated to be an accurate tool to investigate in 3D bone architecture and local mineralization at different hierarchical levels (Muller, 2009) (Nuzzo et al., 2002). Assessment of the osteocyte lacunae has been reported at a nominal resolution of 1.4 μm (F Peyrin, 2009) and 700 nm (Schneider et al., 2007). However, imaging of canaliculi with SR-CT has not been achieved before due to limitations in spatial resolution and radiation dose (Schneider et al., 2010).

We sought to overcome the limitations of the SR-CT imaging system and achieved a valid set-up to image in 3D the osteocyte LCN, based on parallel beam synchrotron radiation nano-tomography (SR-nano-CT).

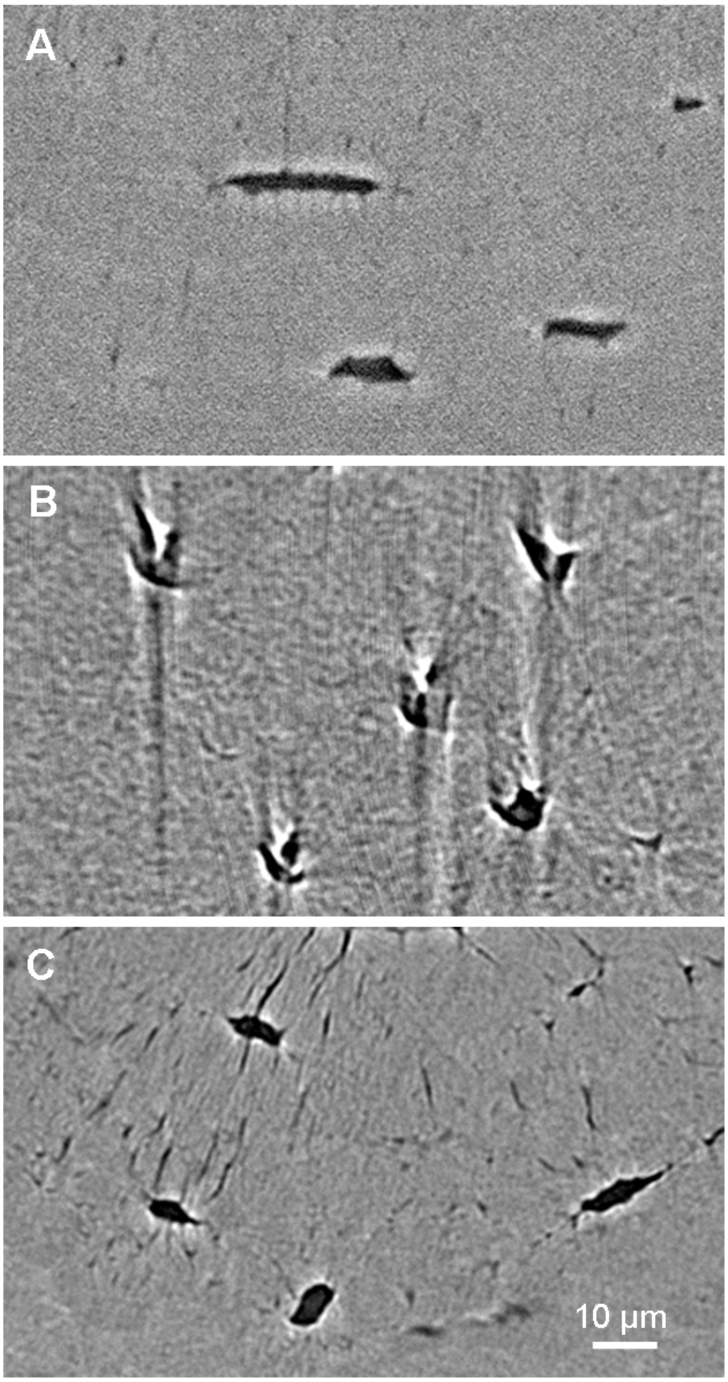

Figure 52: Regions in slices extracted from the 3D images acquired with different imaging configurations, showing the impact of the imaging set-up and of the acquisition conditions on the visibility of canaliculi. A: If the detector efficiency and its point spread function are not optimal, the reconstructed images are corrupted by noise, low contrast and partial volume effects. B: If the X-ray flux is increased in order to compensate for the low efficiency of the detector, the augmented level of the radiation dose causes sample shrinkage and micro-crack propagation, resulting in motion artifacts. C: The optimization of the detector and of the acquisition parameters enables imaging of the lacuno-canalicular network.

8.2 Materials and methods

Sample preparation

Specimens were extracted from the mid-diaphysis of human (women, 87 and 92 years old) femur obtained from a multi-organ collection. A slice of approximately eight millimeters thick was cut perpendicular to the bone axis at the mid-shaft of each femur. Bone samples underwent a treatment (Biobank, Presles en Brie, France) consisting of supercritical carbon dioxide for delipidation, chemical bath in order to eliminate medullary proteins and gamma irradiation for sterilization. After this treatment, samples are considered to be stable in time and can be stored at room temperature. Ethical approval for the samples was granted by the Human Ethics Committee of the Centre du don des Corps at the University René Descartes (Paris, France). The tissue donors or their legal guardians provided informed written consent to donate their tissue for investigation, in accord with legal clauses stated in the French Code of Public Health. Small parallelepiped samples (0.5mm x 0.5mm x 10mm) were then cut with a diamond saw for imaging.

Imaging set-up

Image acquisition was performed at the ID19 experimental station (Weitkamp et al., 2010) at the European Synchrotron Radiation Facility (ESRF), Grenoble, France. The experimental hutch is located at a long distance from the source (145m), permitting to obtain a truly 3D parallel beam CT set-up. X-rays were generated with an undulator yielding very high flux, with a spectrum distributed in narrow bandwidths. A monochromatic X-ray beam was selected with a single-bounce multilayer (Ru/B_4C with a period of 4 nm, on Si substrate) giving a monochromaticity $\Delta E/E \approx 10^{-2}$. The detector was composed of a scintillator (LSO:Tb_4.5 μm) converting X-rays to visible light, a magnifying optic system and a FReLoN (Fast Read Low Noise) cooled charge-coupled device (CCD) camera (Labiche et al., 2007). The pixel size was set to 280 nm which, coupled with a 2D charge coupled device detector, enables imaging of $\sim(574)^3$ μm^3 of tissue in one scan. The sample-to-detector distance was set at 11 mm in order to obtain propagation based phase contrast which enhances the visibility of interfaces, hence the visibility of canaliculi. Data acquisition consists in recording X-ray attenuation maps at different angles of view of the specimen, mounted on a rotating sample stage. Subsequently the volume is reconstructed from the projections with the filtered back-projection algorithm. Different experimental conditions were tested in order to find the optimal parameters. We found that a number of 2000 projections recorded during sample rotation of 180° is suitable. The scan time after optimization was about 35 minutes.

Image reconstruction

The three-dimensional images were obtained from the projection images by applying the filtered backprojection algorithm (PyHST, developed at ESRF). Since the acquisition system is using a parallel beam, there is no magnification and the tomographic reconstruction is exact. The size of the cubic voxel in the reconstructed images is about $(280)^3$ nm^3 (≈ 0.02 μm^3). The resulting image measures 2048x2048x2048 voxels corresponding to a volume of $(574)^3$ μm^3.

Image analysis

For 3D visualization and quantification, the LCN needs to be separated from the bone matrix. Due to the small size of canaliculi and presence of noise in the images, the contrast can be weak and thus a simple thresholding method is not adequate. We designed an analysis method based on contrast enhancement of tubular structures, level set segmentation and connected components filtering. Specific algorithms were developed and implemented in C and C++ based on an in-house library and on ITK library (Kitware). A 3D line enhancement filter (Sato et al., 1998) was applied to improve the visibility of canaliculi. Based on eigenvalue decomposition of the local second order structure of the image, this filter can identify voxels belonging to canaliculi and increase their contrast with respect to the bone matrix. The automatic segmentation was based on the evolution of an initialized level set function which was controlled by a speed factor containing a propagation term (accelerating the evolution in homogeneous regions), a regularization term (based on the mean curvature) and an advection term (J. Sethian, 2000). The initialization of the segmentation was also automatic, created with maximum entropy thresholding and morphological and logical binary operations. After the segmentation, a connected components analysis (Hoshen & Kopelman, 1976) permitted to filter out the residual noise (independent components smaller than 30 voxels were removed). This analysis enables also automatic measurements of the individual components, hence we used it for the quantification of the lacunae, which were segmented separately. For data visualization and 3D renderings we used the software Avizo (VSG) and ImageJ (NIH).

8.3 Results

Whereas the nominal pixel size is 280 nm, the actual spatial resolution is limited by the detector and the image quality is degraded by radiation dose. In conditions of high radiation exposure, the specimen can develop micro-cracks during scan, creating motion artifacts. Therefore, a minimization of the dose is required, although this entails a diminution of signal to noise ratio in the reconstructed image. Since the size of the canaliculi is close to the resolution limits of the system, a loss in image quality is not admissible, hence the necessity to improve and adapt the imaging system.

Figure 52 illustrates the impact of the imaging setup on the image quality. We found that the decisive element in the imaging setup is the scintillator, which needs to be as thin as possible to provide high resolution and efficient in converting X-rays to visible light in order to reduce the required number of photons to create the image. Conversely, the efficiency is proportional to the thickness of the scintillator, thus a tradeoff has to be made. The results showed that using the scintillator LSO_4.5µm (T. Martin et al., 2009) (Douissard et al., 2010) together with the Frelon HDE2V camera, permits simultaneously an improvement of the image quality and a reduction of the radiation dose. Figure 52 C shows a region from a transverse slices extracted from an image acquired with optimal experimental setup.

In Figure 53 A,B are displayed transverse and frontal slices from a reconstructed image showing the size of the field of view which covers both Haversian systems and interstitial tissue. Figure 53 C illustrates a magnified region of interest from a frontal slice, enabling to observe details on the osteocyte network and the bone matrix.

We assessed some measurements on the porosity in the volume shown in Figure 53A.B.

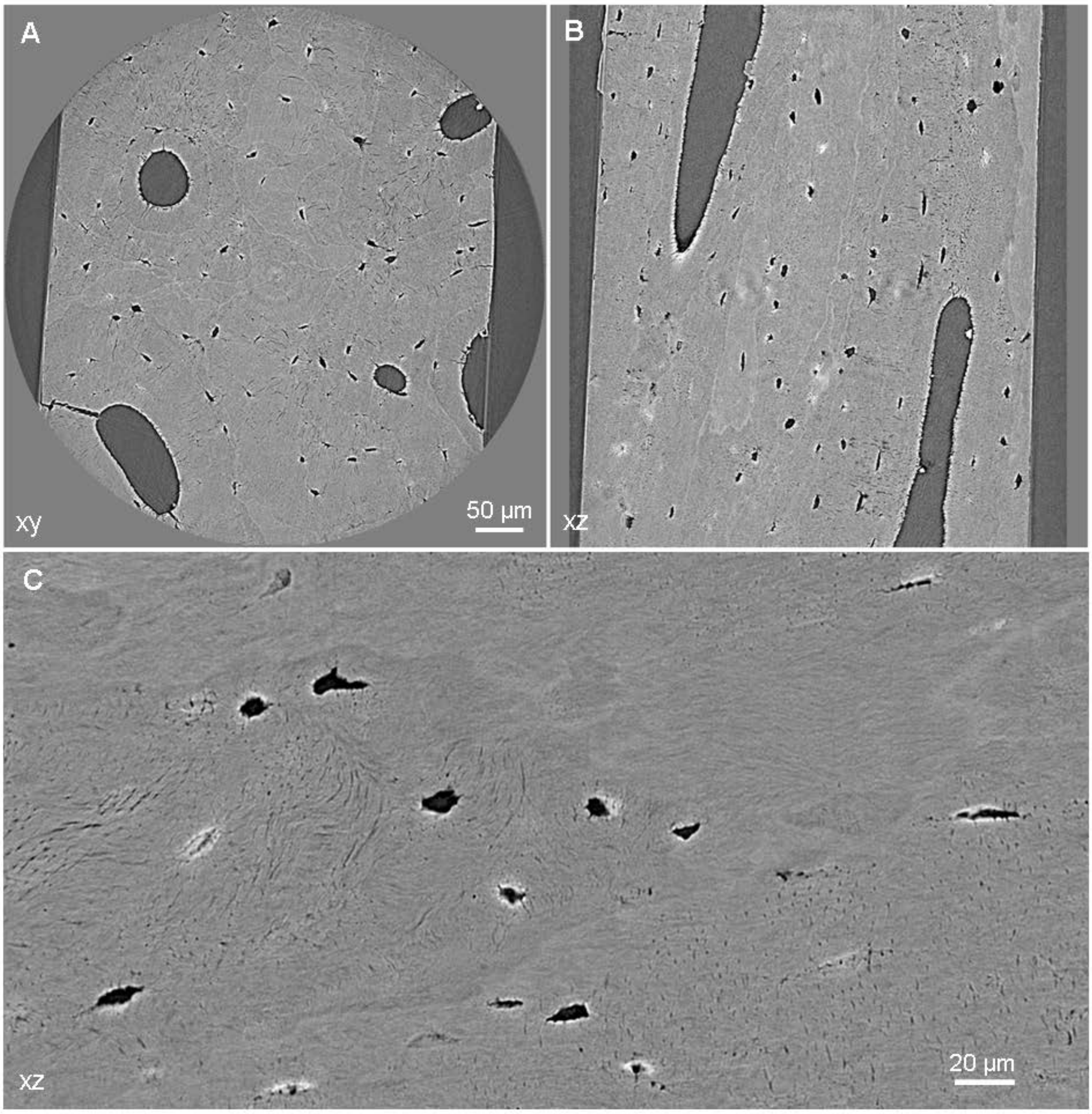

Figure 53: Transverse (A) and frontal (B) slices in the imaged specimen extracted from the mid-shaft of human femur (female, 92 years old) showing the lacuno-canalicular network in several osteons. C: Magnification in a frontal slice, showing canaliculi appearing as dots or linear segments. Details from the bone matrix, as collagen fibers, begin to be visible.

The quantitative results are described in Table 1 and Figure 54. We found 3174 osteocyte lacunae in a human femoral cortical sample measuring 1.36×10^8 μm^3 (TV). The individual lacunar size (<Lc.V>.) exhibits a bimodal distribution, which can be observed on the histogram in Figure 54. The total lacunar volume (Lc.V) was $1.13\times10^6 \mu m^3$, which represents 0.85% of the bone volume (BV). The density of the osteocyte lacunae (N.Lc./BV) was about 24 000 per cubic mm.

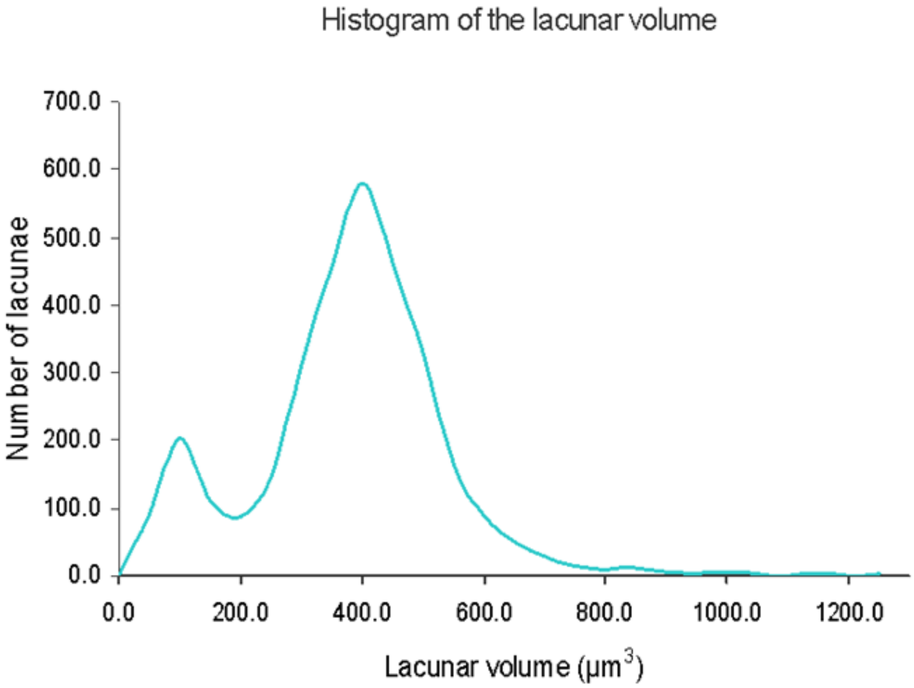

Figure 54: Histogram showing the distribution of the lacunar volume in the sample illustrated in Fig.2 A,B. The imaged sample volume (Sa.V) contains 3174 lacunae (N.Lc) occupying a total volume (Tt.Lc.V) which represents about 8.5 ‰ of the bone volume (BV). We found an average lacunar volume of about 356 µm^3. For the generation of the histogram we used a bin width of 50 µm.

Inside one of the osteons we selected a region measuring 1.3×10^6 µm^3 in which we evaluated the ratios between the lacunar, respectively canalicular volumes and the bone matrix volume. The lacunar porosity represented 0.95% of the bone volume while the canalicular porosity was 1.33% of the bone volume. This suggests that the canalicular porosity is slightly larger than the lacunar porosity.

Figure 55 exhibits the lacuno-canalicular network in a region of interest containing two osteons in the transverse plane. The canaliculi are clearly visible in the reconstructed slices and appear as slender linear segments (Figure 55 A). In order to facilitate the visualization of the variation in degree of mineralization in the intra-osteonal bone matrix with respect to the interstitial tissue, we show an image of the average intensity calculated over 10 slices (2.8 µm) (Figure 55 B). In this image one can observe as well the cement lines, demonstrating higher level of mineralization compared to both osteonal and interstitial tissue.

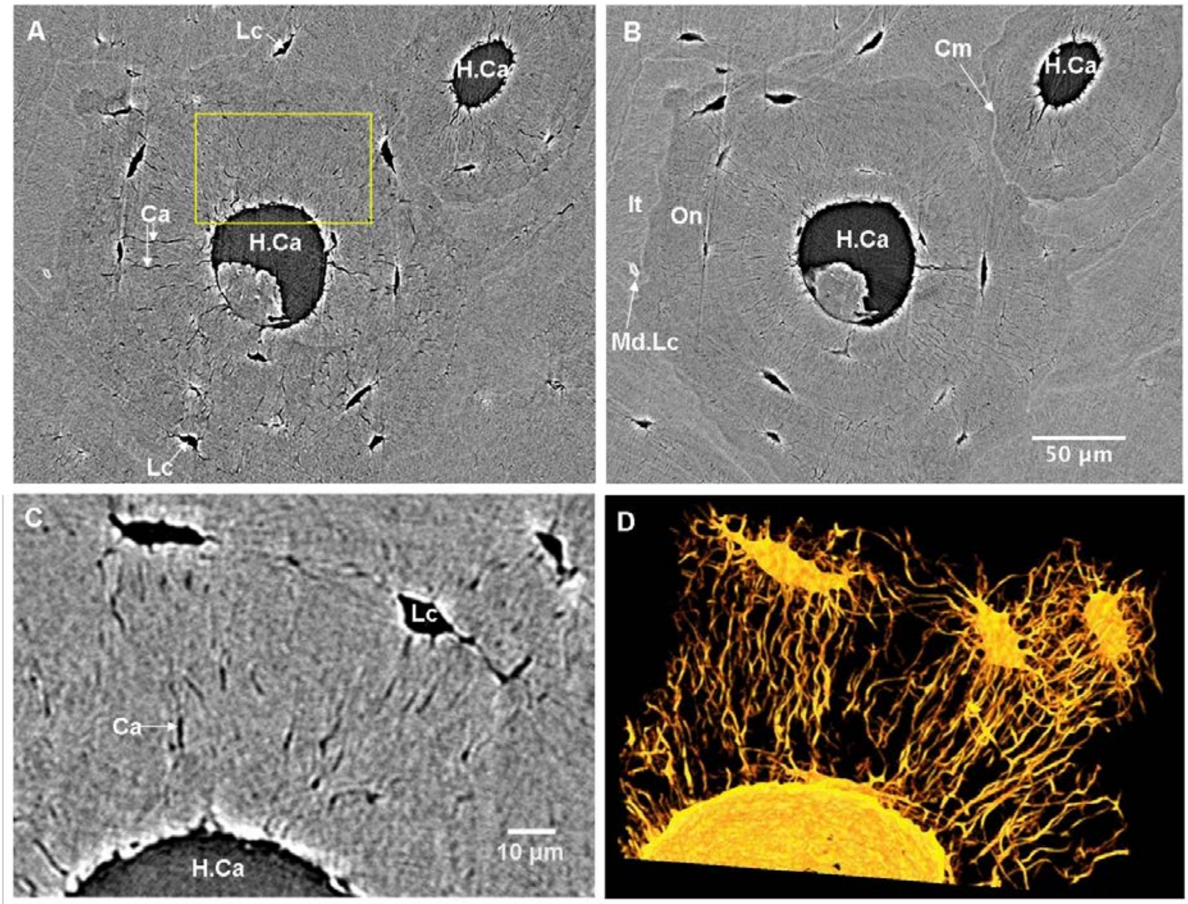

Figure 55: The lacuno-canalicular network in an osteon A: Region of interest in a slice showing a transverse plane in two osteons with Haversian canals (H.Ca), lacunae (Lc) and canaliculi (Ca) (pixel size in slice 0.28 µm, slice thickness: 0.28 µm). B: Average intensity over 10 slices (2.8µm) showing variations in mineralization between the osteon (On) and interstitial tissue (It). The grey level in the image is proportional to the degree of mineralization of bone. In addition one can observe the cement lines (Cm) which appear more mineralized than the rest of the tissue (≈+30% comparing to the osteonal tissue). In the interstitial tissue can be seen a mineralized lacuna (Md.Lc). C: Magnification in a slice corresponding to the position marked in Fig. 3A (slice situated lower in the osteon). D: Three-dimensional rendering of the lacuno-canalicular network in a small volume of interest (98 µm × 68 µm × 32 µm) containing the slice from Fig. 3C. The imaged specimen was human femoral cortical bone from the mid-shaft of a 87 years old female.

Using the cement lines as reference, the osteons can be readily identified. Furthermore, a mineralized lacuna can be seen in the adjacent interstitial tissue. In Figure 55 C and Figure 55 D are displayed, respectively, a magnified area in a slice and the corresponding 3D rendering of the porosity in a region measuring 98 µm × 68 µm × 32 µm. The canaliculi can be seen splitting in two or three branches close to the lacunae.

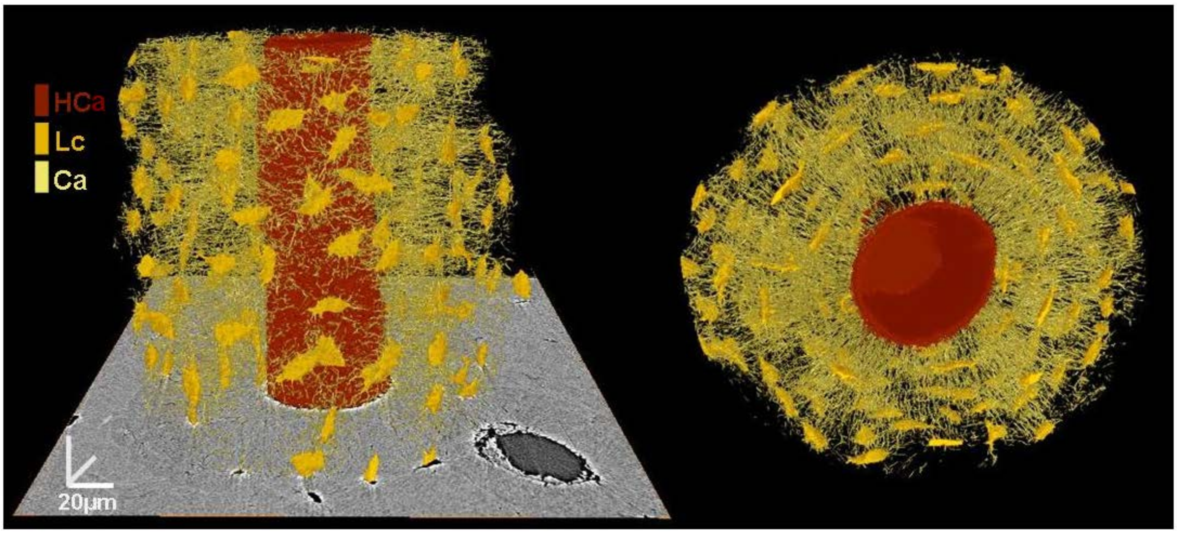

Figure 56: Volume rendering of the segmented porosity in an osteon (left: front view and right: top view), containing the slice depicted in Fig.2A. The image illustrates the organization of lacunae (Lc) and canaliculi (Ca) around the Haversian canal (HCa). This can be seen here for the first time in 3D. The depicted volume contains 160 lacunae with an average individual volume of 230 µm^3.

Figure 56 depicts a 3D rendering of the segmented LCN in an osteon. Within the osteon, the lacunae are highly interconnected by canaliculi running radially from the vessel canal. The shape of the osteocyte lacunae is precisely resolved in these images. A voxel rendering of a volume of interest extracted from the sample presented in Figure 53 A,B is shown in Figure 57. This depicts the organization of the LCN in a larger area covering several osteons with dense cell structures and interstitial tissue showing a sparse and disrupted cell network.

8.4 Discussion and conclusion

We propose a new technique for direct 3D investigation of the lacuno-canalicular network in bone tissue, based on synchrotron radiation CT. In contrast with the commonly used 2D investigation methods, this technique gives access directly to unbiased 3D parameters describing the architecture of the cell network. Compared to the recently proposed 3D imaging techniques, the method proposed here extends the volume of view by three orders of magnitude in terms of number of cells covered and pioneers the 3D investigation of whole osteons. Moreover, this procedure is not dependent of complex sample preparation and the acquisition times are reasonably short (~ 40 minutes/sample).

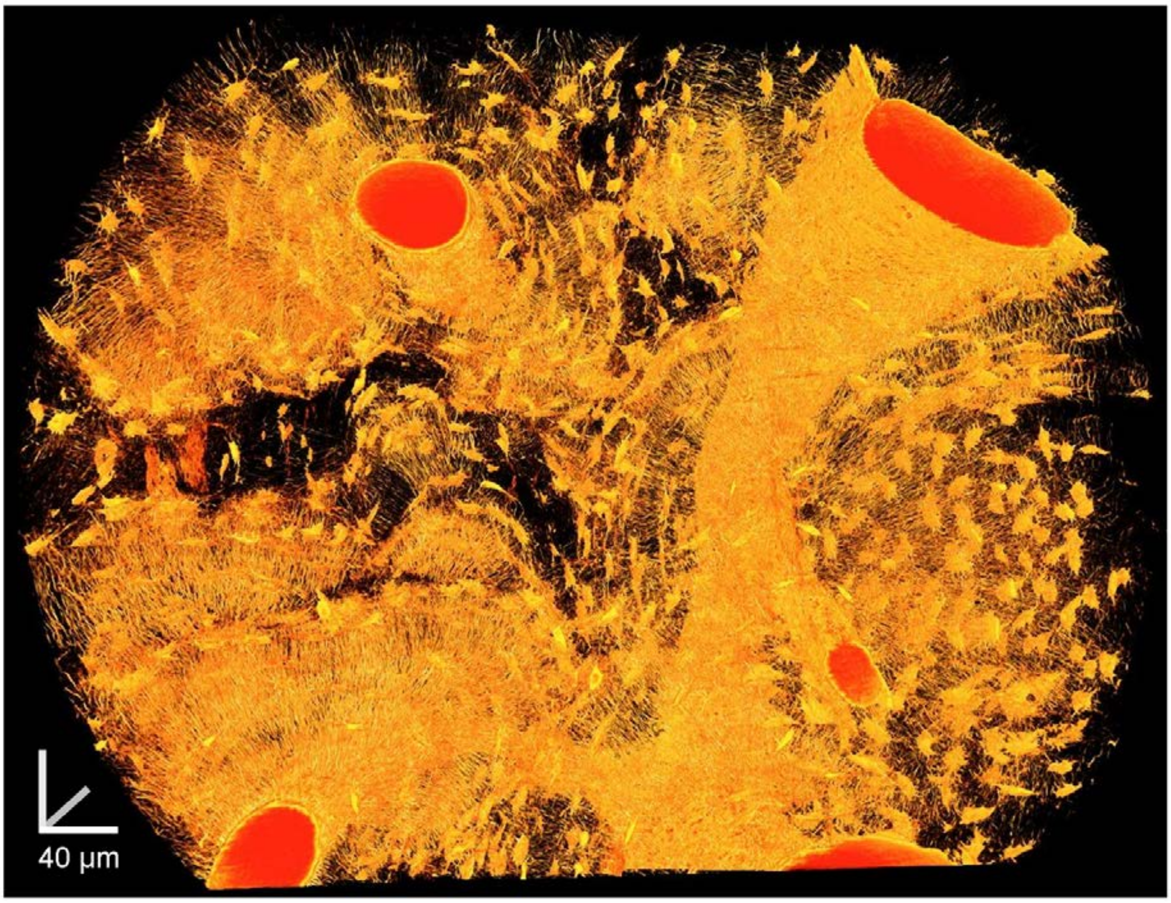

Figure 57 : Three-dimensional rendering of the lacuno-canalicular network and of the vessel canals, in a sub-volume extracted from the sample presented in Fig.2. The showed volume measures 478 µm × 570 µm × 215 µm, corresponding to 37% of the total imaged volume. The cell network in Haversian systems and in interstitial tissue is depicted. One can observe the circular distribution of lacunae around Haversian canals, the elevated density of canaliculi in the osteons as well as the lack of lacunae and canaliculi in the interstitial tissue. The specimen was human femoral cortical bone from the mid-shaft of a 92 years old female.

This advance is contrary to what was believed achievable with available parallel beam X-ray CT techniques (Schneider et al., 2010). This was obtained by improving state of the art synchrotron imaging without the need to resort to scanning techniques, thus keeping acquisition times short (<40 minutes). This enables imaging of series of samples, necessary for biomedical conclusions, which is a significant advantage over imaging techniques proposed so far. This finding enables exploration of correlation between bone diseases and the organization of the cell network and it offers the essential support for further understanding of bone remodeling. In addition, it gives a valuable input for biomechanical modeling of mechanotransduction.

We report the first three-dimensional images of the lacuno-canalicular network on a large field of view, covering several osteons, the primary structural and functional units of compact bone. We present preliminary quantitative results indicating that, inside the osteon, the canalicular volume is larger than the lacunar volume. The individual lacunar volume exhibits a bimodal distribution.

Since the images contain simultaneously information on the degree of mineralization, newer osteons can be distinguished from the older ones. At the same time, the degree of mineralization analyzed at this spatial resolution, permits the examination of the cement lines and of the hypermineralized lacunae and canaliculi which have recently raised attention (Busse et al., 2010) (Frost, 1960) (Yajima et al., 2010).

With a pixel size set at 280 nm and using a 2048x2048 CCD detector, the resulting imaged volume is ~$(574)^3$ μm^3. In human cortical bone such a volume contains up to 4000 osteocyte lacunae, distributed around several Haversian canals. Therefore, this method offers an adequate volume of view to pursue statistical assessment of the LCN architecture within one or more osteons.

In a volume of interest of $(514)^3$ μm^3 we found 3176 lacunae with an average individual volume of ~ 356 μm^3. The histogram of the lacunar volume shows a bimodal distribution with the , which is in agreement with the study from (Hannah et al., 2010). The secondary peak in the histogram could be explained by the presence of partially mineralized lacunae in the interstitial tissue, in this specimen (92 years old, female). We observed numerous totally or partially mineralized lacunae in the interstitial tissue. This is indication of micropetrosis, which is not surprising considering the age of the subject (92 years old) (Busse et al., 2010). The lacunae density was estimated to be ~ 24 000 mm^{-3} which is in the same range as found in the literature (van Hove et al., 2009). Considering that, at this spatial resolution, an average size lacuna (~356 μm^3) occupies around 17,000 voxels, the measurement of the lacunar volume should be accurate. The parameters measured in 3D have the advantage of not being biased by model assumptions, necessary to infer 3D quantities from 2D measurements.

The images show the complexity of the LCN in 3D with a large number of canaliculi running radially from the Haversian canal, orientated mainly perpendicular. Canaliculi branch shortly after leaving from the cell and there are junctions between canaliculi coming from two or three lacunae, at a longer distance from the cell. Due to the possibility to access simultaneously, information on the 3D morphology of the osteocyte network and on the mineralization degree of the bone matrix, the delimitation of the osteons can be done and the behavior of the canaliculi in the vicinity of the cement line can be observed. We noticed that canaliculi are interrupted when reaching the cement line from within the osteon, confirming the conclusions from (Kerschnitzki et al., 2011).

An important application of this method is to provide experimental data at a new scale for biomechanical modeling. At the moment, biomechanical studies (Han et al., 2004) (Liyun Wang et al., 2005) (Beno et al., 2006) at the cellular scale are based on idealized geometry, or on estimation of the cell network characteristics from 2D images. The accurate 3D microstructure of the porous network within complete osteons gives a valuable input for studies assessing solute transport in lacuno-canalicular network and its impact on mechanotransduction.

The main limitation of this technique is the necessity to use a synchrotron X-ray source in order to attain the required beam brilliance, hence the needed spatial resolution. Since the diameter of canaliculi is close to the pixel size, the measurement of the canalicular thickness is not accurate. However, an improvement of the spatial resolution would be in the detriment of the size of the field of view. Although no specific specimen preparation is imposed, in order to obtain a quantitative reconstruction of the degree of mineralization, the samples should be cut small enough to fit in the FOV (0.6 mm). Future work will focus on the reduction of the radiation dose, on the enhancement of image quality and on the development of automatic methods for segmentation and quantification of the cell network.

Morphometric index	**Value**
TV [µm^3]	1.36 10^8
Ca.V [µm^3]	3.60 10^6
Lc.V [µm^3]	1.13 10^6
<Lc.V> [µm^3]	356±164
Lc.V/BV [%]	0.85
N.Lc	3174
N.Lc/BV [mm^{-3}]	~ 24 000

Table 1 Quantitative information extracted from the image shown in Figure 53 and Figure 57 (the specimen was human femoral cortical bone, female, 92 years old). The vessel canals volume (Ca.V) represents 2.7 % of the bone volume (BV) while the osteocyte lacunar volume corresponds to 0.85 % of the BV. The average lacunar volume was 356 µm^3, with a standard deviation of 164 µm^3.

Chapter 9

X-ray phase nanotomography resolves the 3D human bone ultrastructure

Max Langer, Alexandra Pacureanu, Heikki Suhonen, Quentin Grimal, Peter Cloetens, Françoise Peyrin

Manuscript submitted to Plos One

Bone strength and failure are increasingly thought to be due to ultrastructural properties, such as the morphology of the lacuno-canalicular network, the collagen fiber orientation and the mineralization on the nanoscale. However, these properties have not been studied in 3D so far. Here we report the investigation of the human bone ultrastructure with X-ray phase nanotomography, which now provides the required sensitivity, spatial resolution and field of view. The 3D organization of the lacuno-canalicular network is studied in detail over several cells in osteonal and interstitial tissue. Nanoscale density variations are revealed and show that the cement line separating these tissues is hypermineralized. Finally, we show that the collagen fibers are organized as a twisted plywood structure in 3D.

9.1 Introduction

Bone is a hierarchically organized, multiscale natural nanocomposite that is stiff and tough while maintaining lightness. It is also a dynamical tissue that detects and repairs damage at all length scales, thereby adapting to external mechanical constraints (Huiskes et al., 2000), (Taylor et al., 2007)) The mechanisms enabling and controlling these processes are not entirely understood, mainly due to the complex, multiscale 3D organization combined with mechanical and biochemical processes at the cellular level. Bone fragility disease is generally associated with a disturbance of the bone remodeling process, disrupting the balance between tissue resorption and formation. Understanding the mechanisms controlling bone remodeling is fundamental for the understanding of bone failure and to advance treatment of bone disease. At the nanometric scale, the bone matrix does not appear homogeneous since it is made of interwoven mineralized collagen fibers. In mature human cortical bone, osteons, forming units of bone remodeling, are organized in concentric layered lamellae around canals containing vessel and nerve. The osteons are delimited by a layer of tissue called the cement line. The osteocytes and their processes reside in the lacuno-canalicular system, which is the imprint made by the cells. It is increasingly thought that failure is due to microscopic and ultrastructural properties, therefore the need for quantitative 3D imaging at the nanoscale has arisen (Schneider et al., 2010).

Confocal laser scanning microscopy offers 3D imaging of bone ultrastructure, but the depth of penetration is limited, spatial resolution is anisotropic, it is a scanning technique so data acquisition is slow, and use of advanced staining and sample preparation is necessary (Sugawara et al., 2005). Serial sectioning using a focused ion beam followed by imaging with scanning electron microscopy to image the lacuno-canalicular network has been reported (Schneider et al., 2011), which offers excellent spatial resolution, but is a destructive technique, requiring advanced sample preparation, and relatively long acquisition times.

Different X-ray imaging schemes have been proposed to image the ultrastructure of bone. Transmission X-ray microscopy (TXM) has been used to resolve individual lacunae with canaliculi in mouse cancellous bone (Andrews et al., 2010). TXM provides high resolution (40 nm) tomographic imaging with quantitative information on the surrounding bone matrix, but the limited field of view ($5.5\times5.5\times5.5\ \mu m^3$) precludes analysis of more than one cell, thus limiting the prospect to perform quantitative studies. Ptychographic imaging with X-rays has recently shown promising results in imaging the lacuno-canalicular network, but limitations are associated with the scanning acquisition which restricts the practical field of view and yields long data acquisition times (Dierolf et al., 2010). The overlapping of the illumination spots also makes ptychography less dose efficient than full-field techniques. Finally the stringent coherence requirements result in inefficient use of the photon flux.

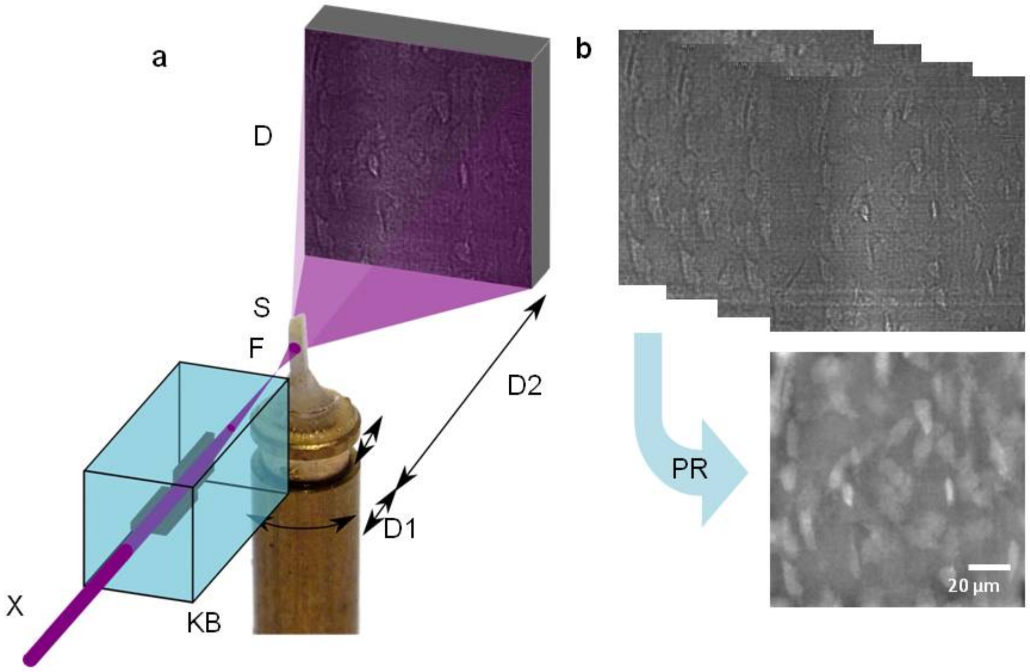

Figure 58 Experimental setup and image reconstruction. (a) Schematic of experimental setup. The X-ray beam (X) is monochromatized and focused into a focal spot (F) by X-ray reflective optics (KB). The sample (S) is positioned on a translation-rotation stage downstream of the focus and imaged onto a stationary detector. Due to the resulting divergent beam, different spot-sample distances (D1) and different free space propagation distances (D2) imply different magnification factors on the detector. (b) Images were recorded at four focus-to-sample distances over a complete turn of the sample at 2999 projection angles. The images were used to reconstruct the phase shift at each angle (phase retrieval PR), which was used as input to a tomographic reconstruction algorithm to reconstruct the 3D local mass density.

X-ray micro-tomography has proven to be a valuable imaging technique enabling non-destructive 3D analysis of internal structures of materials and is now widely used in biomedical imaging (Muller, 2009). The high brilliance of synchrotron X-ray sources gives access to sub-micrometric resolution and the possibility to select a monochromatic beam, allowing quantitative imaging of the degree of mineralization, while maintaining short acquisition times. Synchrotron tomography (SR-CT) has proved to be an accurate tool to investigate 3D bone architecture and local mineralization at different hierarchical scales (Lane et al., 2005) (Bousson et al., 2004) but has so far not been demonstrated for imaging of the lacuno-canalicular network.

Here, we report the first non-destructive true 3D imaging of bone at the ultrastructural level, using X-ray magnified phase tomography. The X-ray beam is monochromatized and focused using X-ray reflective optics to a spot size of 50×50 nm^2 (Kirkpatrick & Baez, 1948), (Bleuet et al., 2009). The sample is placed behind the focal spot and imaged onto a scintillator screen and a CCD camera a fixed distance downstream of the focal spot (Figure 58a). Due to the resulting divergent beam, different magnification factors can be achieved by moving the sample relative to the focal spot. Specimens measuring 0.4×0.4×5 mm^3 were extracted from the mid-diaphysis of a human femur (Figure 59f). The sample is mounted on an air bearing rotation stage to perform tomographic imaging (Figure 58a).

Due to the large relative propagation distances, phase contrast images are obtained with an exceptional sensitivity for density changes. A series of tomographic scans were recorded at four positions relative to the focal spot. The recorded images are not suitable for direct use for standard tomographic reconstruction, but they allow the calculation of phase shift through phase retrieval. At each projection angle, the four images were used to retrieve the phase using a linear filtering based algorithm (Cloetens et al., 1999) (Fig. 1b). Due to the long propagation distance, the non-linear contribution to the contrast is non-negligible. The retrieved phase was further refined using a non-linear conjugate gradient descent algorithm to account for the non-linear contribution in the radiographs and to improve resolution. The retrieved phase maps were input to a tomographic reconstruction algorithm based on filtered backprojection. The resulting tomograms are a reconstruction of the 3D refractive index distribution, being proportional to the local mass density in the object.

9.2 Results

Reconstructed tomographic slices in the transverse (a), frontal (b) and sagittal (c) plane are shown in Figure 59. These show ultrastructural features in bone in 3D with unprecedented quality. Not only are the osteocyte lacunae (Lc) and canaliculi (Ca) clearly visible, but also features such as the cement line (Cm), the structure of the surrounding matrix and its mineralization. The composite nature of an interwoven mineralized fiber matrix can be clearly seen (Figure 59a-d, i,).

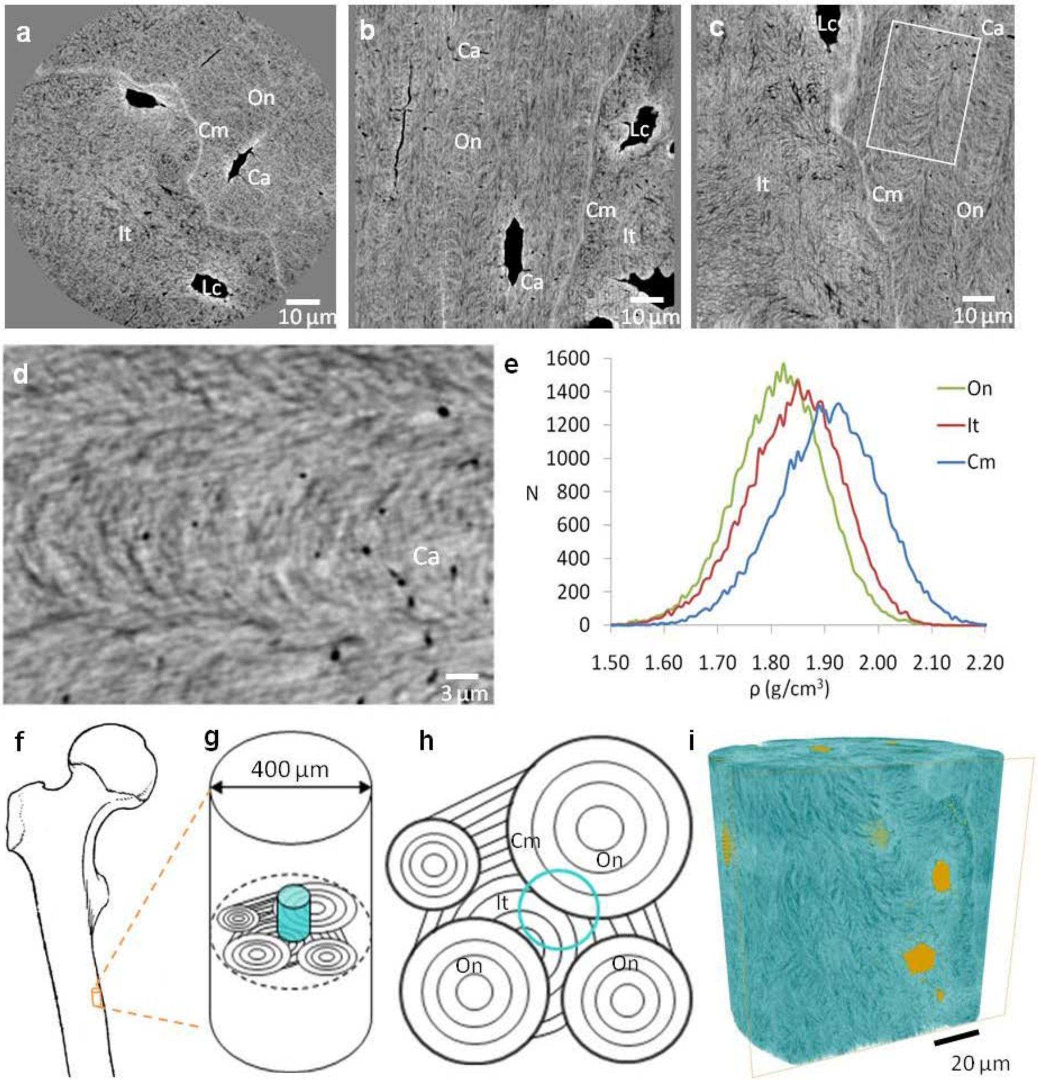

Figure 59 Retrieved information in the reconstructed images. (a) Transverse, (b) frontal and (c) sagittal slices through the images reconstructed from phase data. Grayscale is proportional to local density. Osteocyte lacunae (Lc) and canaliculi (Ca) can clearly be seen. The heterogeneous organization of the matrix by mineralized collagen fibers can also be distinguished (box). In this sample, a continuous change in collagen orientation can be seen between adjacent lamellae. The cement line (Cm), separating osteonal (On) and interstitial (It) tissue, can clearly be distinguished as more mineralized than the surrounding matrix. Tissue close to osteocyte lacunae is also hypermineralized. (d) Zoom on the boxed area in C. Matrix orientation is clearly visible and canaliculi are seen as black dots. (e) Mass density histograms in the three tissue types. (f) Samples were extracted from the mid diaphysis of a human femur. (g) The blue cylinder shows the imaged region inside the sample. (h) Schematic of a transverse section showing the organization of lamellar bone in osteons, interstitial tissue and cement lines. Blue circle shows the positioning of A. (i) Rendering of the electron density in the sample (blue) and porosity (yellow). Structures such as osteocyte lacunae (Lc) and canaliculi (Ca), the cement line (Cm) and collagen fibers are revealed.

In the tomographic images, osteocyte canaliculi enclosing the cellular processes are visible as black spots and striations depending on their orientation relative to the virtual cutting plane (Figure 59a-d). We remark the flattened lenticular drop shape of the osteocyte lacunae, the top end being wider and rounder and tapering off towards the bottom (Figure 60, Supp. Figure 66, Supp Figure 67). In osteonal tissue the canaliculi are resolved, perfectly maintaining the connectivity of the network, and we can see that most canaliculi branch into two or three a short distance from the lacuna (Figure 60b). The canalicular network is considerably decreased in the interstitial tissue (Figure 60a, Supp. Figure 66, Supp Figure 67).

The cement line can clearly be seen in the tomograms as a bright line (Figure 59a-d, i). This is the tissue separating osteons from each other and from interstitial tissue, forming the boundary between the end point of bone resorption and the starting point of new bone formation. From the grayscale images, the local mass density can be directly measured. We can see that in this sample, the cement line is hypermineralized; it has a significantly higher density (1.909±0.097 g/cm^3) than the surrounding osteonal (1.818±0.089 g/cm^3) and interstitial tissue (1.845±0.090 g/cm^3) (ANOVA F-test, $p<0.01$, Post-hoc Tukey's HSD test, $p<0.01$). The interstitial tissue is also significantly more mineralized than the osteonal tissue (Post-hoc Tukey's HSD test, $p<0.01$). Histograms of the mass density in the different tissue types measured in subvolumes of 8 µm^3 are shown in Figure 59e.

Further, in this volume no canaliculi cross the cement line, they rather turn and run parallel with it, in line with what has been previously observed by confocal light scanning microscopy (Kerschnitzki et al., 2011). Here however, we can observe that some canaliculi also end at the cement line (Figure 60b). In the osteonal tissue, lacunae have similar shape and size (286.4±1.2 µm^3) and they are well connected via the canaliculi (canalicular volume over lacunar volume ~50 %). Conversely, in the interstitial tissue all the lacunae are disconnected, with variable shapes and sizes (364.1±63.6 µm^3), larger in volume than the intra-osteonal lacunae (ratio canalicular volume over lacunar volume ~6 %). From the tomographic slices (Figure 59a-c) we can see that, in this sample, the osteonal tissue demonstrates a plywood-like structure. There is a continuous variation of angles of orientation throughout the lamellae, showing the characteristic arc-like structure in slices oblique to the lamellae orientation (Figure 59c).

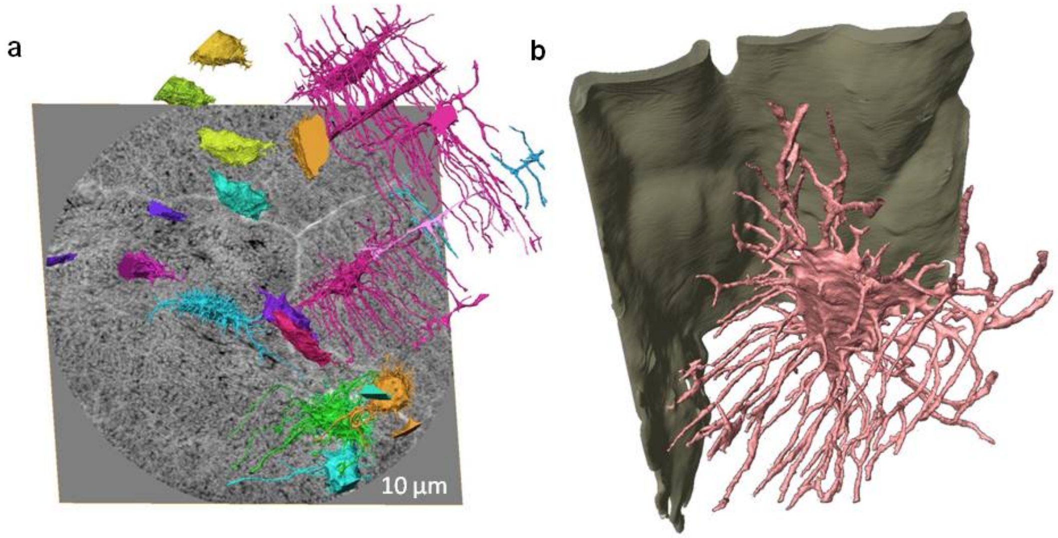

Figure 60 3D renderings of ultrastructural bone features. (a) Rendering of osteocyte lacunae and canaliculi in the whole imaged volume overlayed over the bottom slice shown in grayscale. Colors correspond to connected components and grayscale to mass density. Note the difference in structure in the interstitia and osteon: the connected cells are all in the osteonal tissue, the others in the interstitial. The canaliculi are considerably reduced in the interstitia. (b) Zoom on the highlighted lacuna in A showing the interaction between the canaliculi (pink) and the cement line (green), and branching of the canaliculi.

9.3 Discussion

We have demonstrated tomographic imaging of bone ultrastructure with 3D X-ray phase nanotomography. This method allows full-field imaging with a large field of view without reverting to scanning techniques. In addition, no special sample preparation is needed. The zoom effect available with the projection setup allows for imaging of a specific region of interest selected inside an extended sample. The method is more sensitive than attenuation based techniques, such as TXM, but also phase based techniques such as ptychography. This is evidenced by not only revealing the 3D organization of the lacuno-canalicular network, but also the collagen fiber orientation and differences in mineralization between different bone tissue types.

There are still disagreements about the exact role of the osteocytes in bone remodeling and control of bone mineralization. Very little quantitative data on the osteocyte system is available and many interpretations are questionable due to possible artifacts in the techniques used so far. Here, we have shown anatomical features of the LCN, such as precise shape of the lacunae, branching of the canaliculi and the relationship between the LCN and the cement line, unattainable with previously used techniques.

The cement line is thought to have an important role in limiting damage propagation and the overall stiffness of bone. It has been disputed whether the cement line is hypomineralized or hypermineralized (Skedros et al., 2005). Here we can directly measure the relative density of the different tissues, and show that the cement line has a significantly higher mass density than the surrounding osteonal and interstitial tissue.

The ability to directly study the collagen fiber orientation in 3D in the bone opens completely new possibilities for studying bone fragility. Collagen fiber orientation analysis has so far been performed in 2D using scanning electron microscopy (Pannarale et al., 1994), transmission electron microscopy (Giraud-Guille et al., 2003), atomic force microscopy (27), or indirectly analyzed by polarized light microscopy (Bromage, Goldman, et al., 2003) and Raman spectral mapping (Kazanci et al., 2006). The precise description of the 3D arrangement of collagen fibers as can be obtained with the proposed technique is fundamental for the understanding of the mechanical properties of bone.

Magnified phase tomography allows adequate investigation of the anatomy of the osteon at the collagen fiber level in 3D. Due to this, coupled with the fast acquisition time and simple sample preparation, the proposed methodology is expected to have a major impact in the production of new quantitative data, necessary for advances in bone biology and in designing biomedical and bioinspired materials.

9.4 Materials and Methods

Sample preparation

Specimens were extracted from the mid-diaphysis of human (women, 87 and 92 years old) femur obtained from a multi-organ collection. A slice of approximately eight millimeters thick was cut perpendicular to the bone axis at the mid-shaft of each femur. Bone samples underwent a treatment (Biobank, Presles en Brie, France) consisting of supercritical carbon dioxide for delipidation, chemical bath in order to eliminate medullary proteins and gamma irradiation for sterilization. After this treatment, samples are considered to be stable in time and can be stored at room temperature. Ethical approval for the samples was granted by the Human Ethics Committee of the “Centre du don des Corps” at the University René Descartes (Paris, France). The tissue donors or their legal guardians provided informed written consent to donate their tissue for investigation, in accord with legal clauses stated in the French Code of Public Health. Small parallelepiped samples (0.4 mm x 0.4 mm x 5 mm) were then cut with a diamond saw for imaging.

Imaging set-up

Nano-tomography was performed at the nano-imaging station ID22NI of the ESRF. The technique uses as illumination source the X-ray spot focus produced by dynamically figured multilayer-coated mirrors (Kirkpatrick-Baez crossed mirror geometry). An X-ray energy of 17 keV was selected corresponding to the first harmonic of a single-line undulator (19 mm period U19). No other monochromatization than the one provided by the multilayer coatings was used, assuring a high flux and short acquisition times. The undulator-multilayers system provides a medium monochromaticity of $\Delta E/E=1.6\times10^{-2}$. The sample was set at a small distance downstream of the focus and the transmitted intensity was recorded with a two-dimensional detector set at a large distance from the focus. The geometric magnification M of this setup is given by

$$M = \frac{\mathrm{D1} + \mathrm{D2}}{\mathrm{D1}} \quad (1)$$

where D1 is the distance between the focal point and the sample, and D2 the distance between the sample and the detector. The radiographs were acquired with a detector system consisting of a high efficiency LSO:Tb luminescent converter screen (30), lens coupled to a large dynamic range and highly efficient Charge-Coupled Device camera (ESRF developed FReLoN camera). A detector area of 1500×1500 pixels and an effective pixel size of 1 µm was used. Radiographs were taken at four sample-source distances (D1 = {32.6, 33.6, 37.6, 47.6} mm) while keeping the detector position fixed at D1+D2 = 525 mm. This geometry results in a final pixel size of 60 nm and a field of view of 90 µm. The sample being significantly larger (0.4 mm sides) than the field of view, local tomography was performed after selecting the relevant region of interest on a low resolution tomography scan (0.32 µm pixel size with a single propagation distance). For tomography, images were recorded at 2999 angular positions of the sample around a vertical rotation axis over one complete turn. The exposure time for each radiograph was 100 ms, resulting in a total acquisition time of 1.9 hours for the tomographic scans at four focus-to-sample distances.

Image reconstruction

From the data acquired in the four tomographic scans the 3D mass density distribution in the sample is reconstructed. We briefly outline here the different steps of this process. The radiographs recorded in the divergent beam geometry of Figure 58 are magnified Fresnel diffraction patterns that contain the object information in an entangled form. A phase retrieval step based on radiographs measured at the same angular position but different distances allows to "deconvolve" the image formation process and retrieve the object information. The radiographs depend on the sample through its complex refractive index $n(x,y,z)$ and on the settings of the experiment (propagation distances *D1*, *D2* and the X-ray wavelength λ). In the present case of hard X-rays the propagation and dynamical effects inside the sample can be neglected, and the wave exiting the sample is modulated in amplitude as

$$A(x,y) = \int \frac{2\pi}{\lambda} \beta(x,y,z)dz \quad (2)$$

and in phase as

$$\varphi(x,y) = -\int \frac{2\pi}{\lambda} \delta(x,y,z)dz \qquad (3)$$

with the absorption index β and the refractive index decrement δ. These optical properties describe the complex refractive index as

$$n = 1 - \delta + i\beta \qquad (4)$$

As equations (2) and (3) are projections along the X-ray path, the distributions of β and δ can be reconstructed with tomography techniques assuming the amplitude and phase modulation can be measured for different angular positions of the sample. The absorption index β is proportional to the familiar linear attenuation coefficient μ (=4πβ/λ). The dominant information resides in the refractive index decrement given by

$$\delta = \frac{r_c \lambda^2}{2\pi V} \sum_j (Z_j + f_j') \quad (5)$$

where r_c = 2.8 fm is the classical electron radius. The summation is over all atoms contained in the representative volume V; Z_j is their atomic number and f'_j the real part of the wavelength dependent dispersion correction. By selecting an X-ray energy of 17 keV, far above the absorption edges of the elements present in the sample, the dispersion correction is negligible (highest K 1s binding energy at 4.0 keV for Calcium). Thus the refractive index decrement is simply proportional to the electron density in the sample. As bone tissue is mostly constituted of light elements, the ratio atomic number over atomic mass Z/A is very close to 1/2 and the refractive index decrement can be well approximated as (Guinier, 1994):

$$\delta \approx 1.310^{-6}\, \rho\, \lambda^2 \qquad (6)$$

where the mass density ρ is expressed in g/cm^3 and the wavelength λ in Å (0.729 at X-ray energy of 17 keV).

For the phase retrieval we use the equivalence between spherical wave illumination and plane wave illumination with a magnification given by equation (1) and the equivalent propagation distance

$$D = \frac{\mathrm{D1} \cdot \mathrm{D2}}{\mathrm{D1} + \mathrm{D2}} \qquad (7)$$

The four radiographs are resampled to a unique magnification corresponding to the plane closest to the focus (pixel size of 60 nm). A first estimate of the phase map is obtained with a linear least squares method weighting correctly the contribution of each of the four propagation distances. An adaptation of the linear method described in (Cloetens et al., 1999) is used. Here, we assume proportionality between the phase and amplitude modulation according to a fixed δ/β ratio. This supplementary assumption allows to use the absorption information, sensitive to low spatial frequencies, to complement the phase information, mainly sensitive to high spatial frequencies. The high δ/β ratio of 202 for cortical bone (ICRU-44) quantifies well the higher sensitivity of phase imaging as compared to attenuation imaging. Due to the large equivalent propagation distances and the high spatial resolution, the non-linear contributions in the image contrast are non-negligible. The retrieved phase was therefore refined using an iterative procedure based on a non-linear conjugate gradient method. This refinement is crucial for the spatial resolution. Ten iteration steps were used. In this part of the phase retrieval, the amplitude and phase modulation were no longer assumed to be proportional, but the amplitude modulation was enforced to contain no high spatial frequency information.

The retrieved phase maps were used as input for tomography reconstruction using a filtered backprojection algorithm. We used the ESRF inhouse developed software PyHST that includes a specific padding scheme adapted to local tomography. According to eq. 6, the reconstruction of the distribution of the refractive index decrement δ yields directly the distribution of the mass density ρ. A simple correction of the offset is required due to the local tomography setting. It is based on the knowledge that the density inside the osteocyte lacunae is equal to zero.

Image analysis

For the segmentation of the lacunar-canalicular network we used a 3D line enhancement filter (Sato et al., 1998) to improve the contrast of canaliculi with respect to the bone matrix. This filter is based on eigenvalue decomposition of the second order structure of the image, computed locally. The mutual relations between the eigenvalues permit to identify voxels belonging to a tubular-like structure, with the size given as a parameter. The voxels that are likely to be part of canaliculi are highlighted while the rest of the voxels are darkened. This filter permits to keep the connectivity of the canaliculi while thresholding.

Let $f(\mathbf{x})$ with $\mathbf{x} = (x, y, z)$, be a 3D image. Because the second order derivatives are sensitive to noise, the image is smoothed with a Gaussian kernel. The second derivatives of the smoothed image, denoted $f_{\mathrm{ab}}(\mathbf{x};\sigma)$, can be calculated as:

$$f_{\mathrm{ab}}(\mathbf{x},\sigma) = \left\{ \frac{\partial^2}{\partial a \partial b} g_\sigma(\mathbf{x}) \right\} * f(\mathbf{x}) \quad (8)$$

where $g(\mathbf{x})$ is an isotropic Gaussian function with standard deviation σ and a,b are the row and column indices in the Hessian matrix. The filter may thus be tuned to a specific scale by adjusting σ.

Let λ_k be the eigenvalue with the k^{th} smallest magnitude ($|\lambda_1| \leq |\lambda_2| \leq |\lambda_3|$) of the Hessian matrix at voxel $\mathbf{x}$. A voxel in an ideal tubular structure is characterized by: $|\lambda_1| \approx 0$; $|\lambda_1| << |\lambda_2|$; $\lambda_2 \approx \lambda_3$. For bright structures, λ_2 and λ_3 must have negative values. The similarity measure as defined in (32) can be expressed as following:

$$v(\mathbf{x}) = \begin{cases} \exp(-\lambda_1^{\ 2} / 2(\alpha_1 \lambda_c)^2) & \lambda_1 < 0,\ \lambda_c \neq 0 \\ 0 & \lambda_c = 0 \\ \exp(-\lambda_1^{\ 2} / 2(\alpha_2 \lambda_c)^2) & \lambda_1 < 0,\ \lambda_c \neq 0 \end{cases} \qquad (9)$$

with $\lambda_c = \min(-\lambda_2, -\lambda_3)$.

Subsequently we performed an analysis of the connected components (Hosen,) in order to quantify the network and to remove residual noise. Unconnected components measuring less than ~2 µm^3 were eliminated.

The algorithms for image analysis were implemented in C and C++ languages, based on an in-house library and on ITK library (Kitware). For data visualization and generation of 3D renderings we used the software Avizo (VSG) and ImageJ (NIH).

Chapter 10

Perspectives and conclusions

We sought to achieve imaging of the lacuno-canalicular network in bone tissue with synchrotron radiation computed tomography. Following a considerable number of tests and experiments, we established two valid imaging setups with respect to the instrumentation and the acquisition parameters. These are based on parallel beam SR-CT, with a spatial resolution of 280 nm. This permits to acquire images of tissue covering about 600^3 μm^3 from which the lacuno-canalicular network can be segmented and quantified. Compared to the existing 3D imaging techniques, the developed method covers a vastly larger volume of view, it is non-destructive, considerably quicker, it does not require modifying sample preparation and it yields simultaneously information on tissue structure and composition.

Further improvement of the quality of the acquired images could be obtained with an enhanced detector, permitting to improve the spatial resolution and the signal to noise ratio, for the same amount of radiation dose. Since the contrast created by the phase shift can be detected as well when the X-ray attenuation is fairly week, a reduction of the radiation dose could be obtained by using phase reconstruction which permits to scan the samples at higher energies. Moreover, by using phase imaging, the sensitivity to the degree of mineralization can be improved. However, the currently available phase retrieval algorithms introduce a slight blur in the images, due to approximations necessary for the reconstruction of the phase shift. Given the limitations in terms of spatial resolution, this blurring effect is severe enough to cancel the visibility of canaliculi. Alternatively, the reconstruction of the 3D refractive index distribution can be used as a complement to the reconstruction of the X-ray attenuation coefficient with enhanced edges by phase contrast. At present, research work is attempting to improve the phase retrieval accuracy, which would eventually enable to detect canaliculi as well.

We proposed an image enhancement method and two segmentation methods, adapted for the detection of the lacuno-canalicular network, from SR-CT images. One of the segmentation techniques is based on level sets and the second is based on active regions. The second method, based on the evolution of seeded regions controlled by information extracted from both the original image and the 3D line enhancement filter map, gave better results. This permitted to detect more than 95% of the cell network with a good level of connectivity. The drawback of this technique is that it tends to thicken the canaliculi. This could be overcome by computing the 3D skeleton of the segmented structure. This would result in a more accurate segmentation of the canaliculi since they are normally not thicker than one voxel. The lacunae can be obtained from the segmented image by morphological operations. Another limitation of the method comes from the connectivity of canaliculi which is not guaranteed at 100%. For example, if the canaliculi are interrupted in the acquired images due to partial volume effect, the missing portion will not be reconstructed.

A different approach for the image segmentation could rely on finding the minimal path cost to connect two cell lacunae through canaliculi. This type of methods inspired from Dijkstra's algorithm, are currently expanding in the field of image segmentation (Dijkstra, 1959) (Hua Li & A. Yezzi, 2007) (Rouchdy & L. D Cohen, 2008) (Benmansour & Laurent D. Cohen, 2010). The advantage of this method would be that the connectivity of canaliculi is imposed; therefore the partial volume effect is no longer problematic.

Once the automatic segmentation of the cell network is achieved, automatic methods for quantification are necessary. For example, evaluating the length of each canaliculus or counting the number of canaliculi attached to each lacuna, are not trivial problems.

Very little quantitative studies on the 3D morphology of the lacuno-canalicular network can be found in the literature. The possibility to image and quantify in 3D the lacuno-canalicular network creates opportunities to conduct new research studies related to mechanotransduction, bone remodeling and the effects of pathology and treatment on the osteocyte network. For example, preliminary results indicate that the integrity of the osteocyte network is strongly affected in case of advanced stages of osteoporosis (Figure 61), supporting results from (M. L. Knothe Tate et al., 2002).

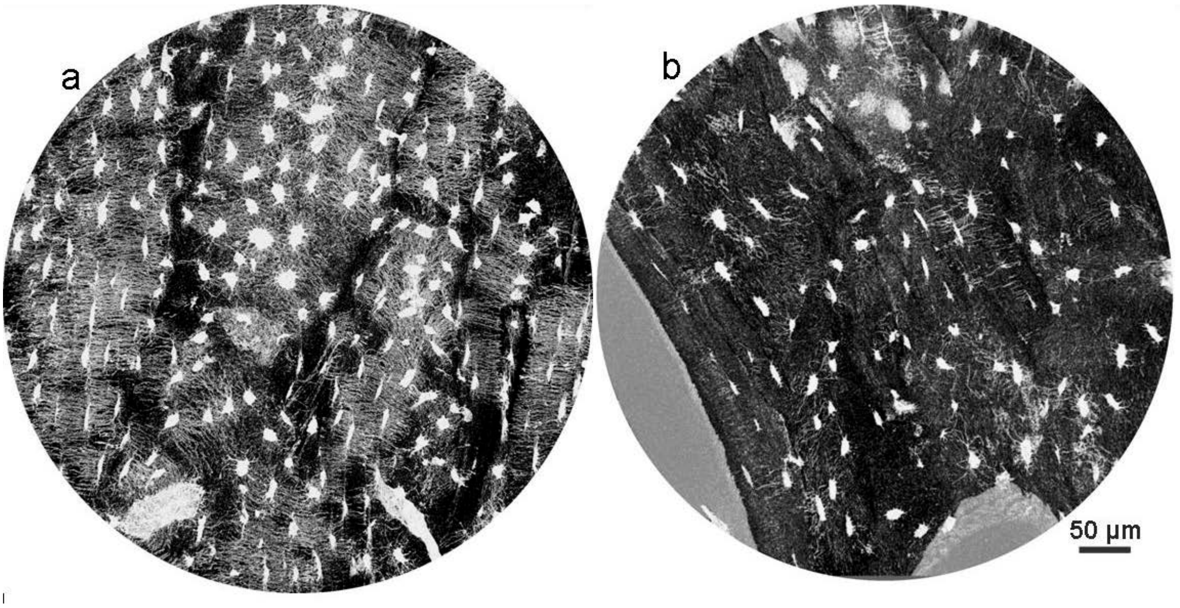

Figure 61 Effects of osteoporosis on the integrity of the osteocyte network. a) Maximum intensity projection (MIP) (~ 15 µm) showing the cell network in a sample of hip biopsy taken from a patient suffering of early stage osteoporosis. b) MIP (~ 15 µm) showing the disrupted cell network in a sample of hip biopsy taken from a patient with advanced stage of osteoporosis. Image spatial resolution was 280 nm. The osteoporotic human specimens were provided by Marie-Hélène Lafage-Proust from LBTO, St Etienne).

Imaging of bone tissue at this scale can be useful as well for measurements of the mineralization level within and outside the osteons. It is widely accepted that osteonal tissue is less mineralized because it is younger. However, the difference in mineralization degree evaluated from lower resolution images is biased due to the canaliculi which can not be seen, but can influence the appearance of the tissue.

Whereas the aim of this thesis was to image and analyze the architecture and integrity of the osteocyte cell network, some additional features can be studied from the acquired images. We give here a few examples which we illustrate and relate to the literature.

We observed that in the interstitial tissue, many osteocyte lacunae and their canaliculi are filled with mineral. We could distinguish three different typologies. A part of the lacunae are completely filled with mineral which shows a higher degree of mineralization than the surrounding interstitial tissue (Figure 63). These hypermineralyzed lacunae are related to the disorder called micropetrosis (Frost, 1960). Another part of the lacunae are filled with mineral with a similar degree of mineralization compared to the adjacent tissue. However, in this case the lacuna “shell” is more mineralized.

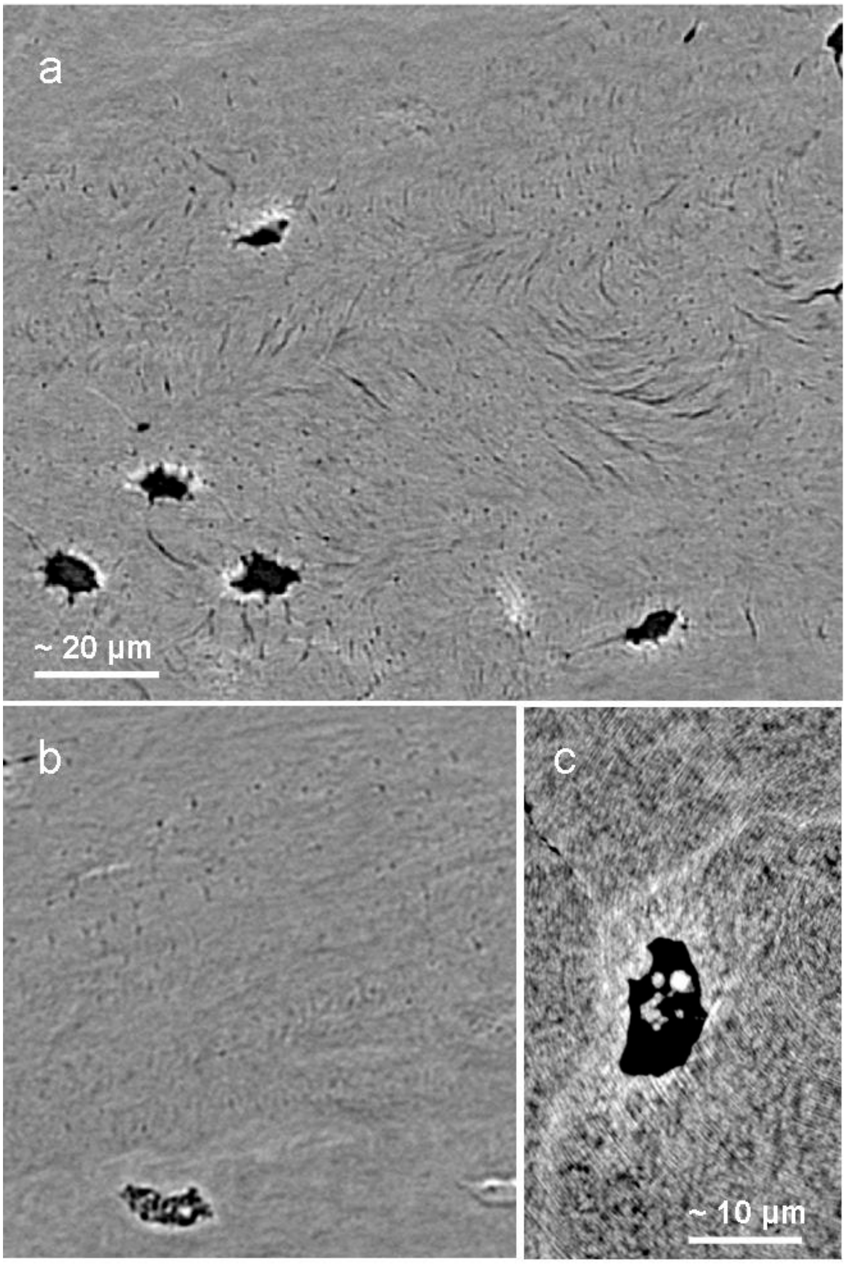

Figure 62 Collagen fibres are visible and mineral particles are observed in the osteocyte lacunae a) Region from a frontal slice in a reconstructed image showing that the pattern made by the collagen fibres is visible. b), c) Small regions from slices showing mineralized particles inside the cell lacunae. Most of the lacunae exhibiting this particularity are located in interstitial tissue. Spatial resolution was 280 nm in panels (a),(b) and 60 nm in panel (c).

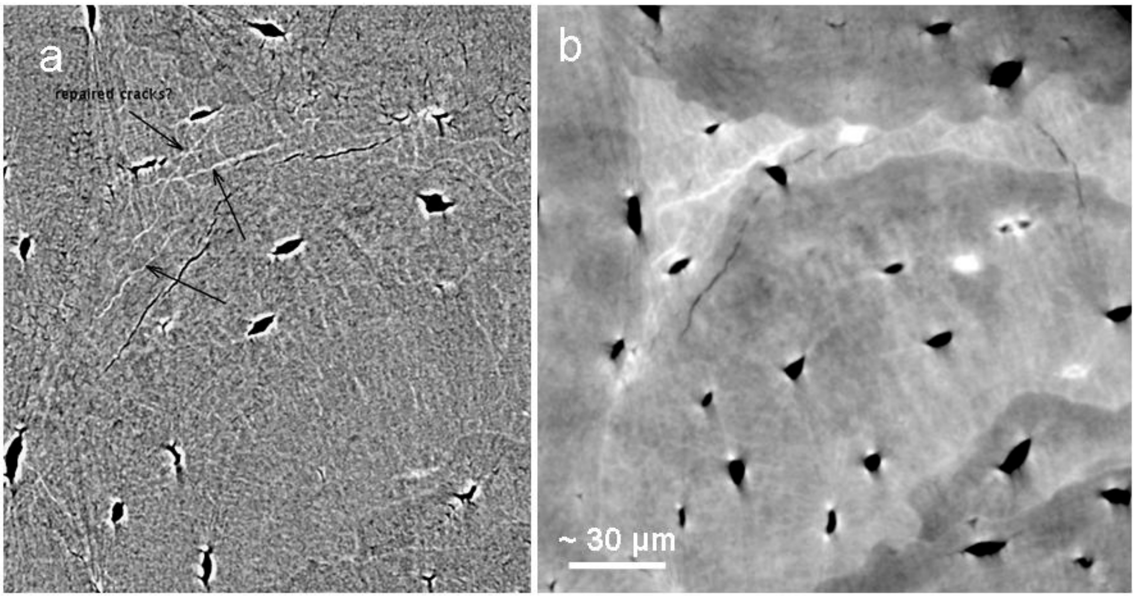

Figure 63 Regions from reconstructed slices showing mineralized micro-cracks located in interstitial tissue. a) Image reconstructed from X-ray attenuation combined with phase contrast b) Image reconstructed after phase retrieval. Image spatial resolution was 280 nm.

Finally, some lacunae contain small mineralized parts, usually with blob-like shapes, which are noticeably more mineralized than the rest of the bone matrix (Figure 62b,c). This last situation was referred to in the literature as lacunae containing “mineralized” pearls (A. Boyde, P. Hendel, et al., 1990). The relation between these three types of presence of mineral within lacunae and osteocyte death or bone disorders might be interesting to be investigated more in depth (Busse et al., 2010).

Figure 62 b, c shows lacunae located in the interstitial tissue containing particles which exhibit a high level of mineralization. The images are acquired at two different spatial resolutions (280 nm and 60 nm). In Figure 63b, a few lacunae which are completely filled with mineral (hypermineralized) can be observed. This image is extracted from a volume which was obtained after applying a phase retrieval algorithm (Paganin et al., 2002).

We observed the existence of some hypermineralized microcracks within interstitial tissue. These are usually quite thin (1-2 µm thick) and sometimes crossed (Figure 63). This could be related to a different way to repair micro-damage, which is alternative to tissue renewal (Alan Boyde, 2003).

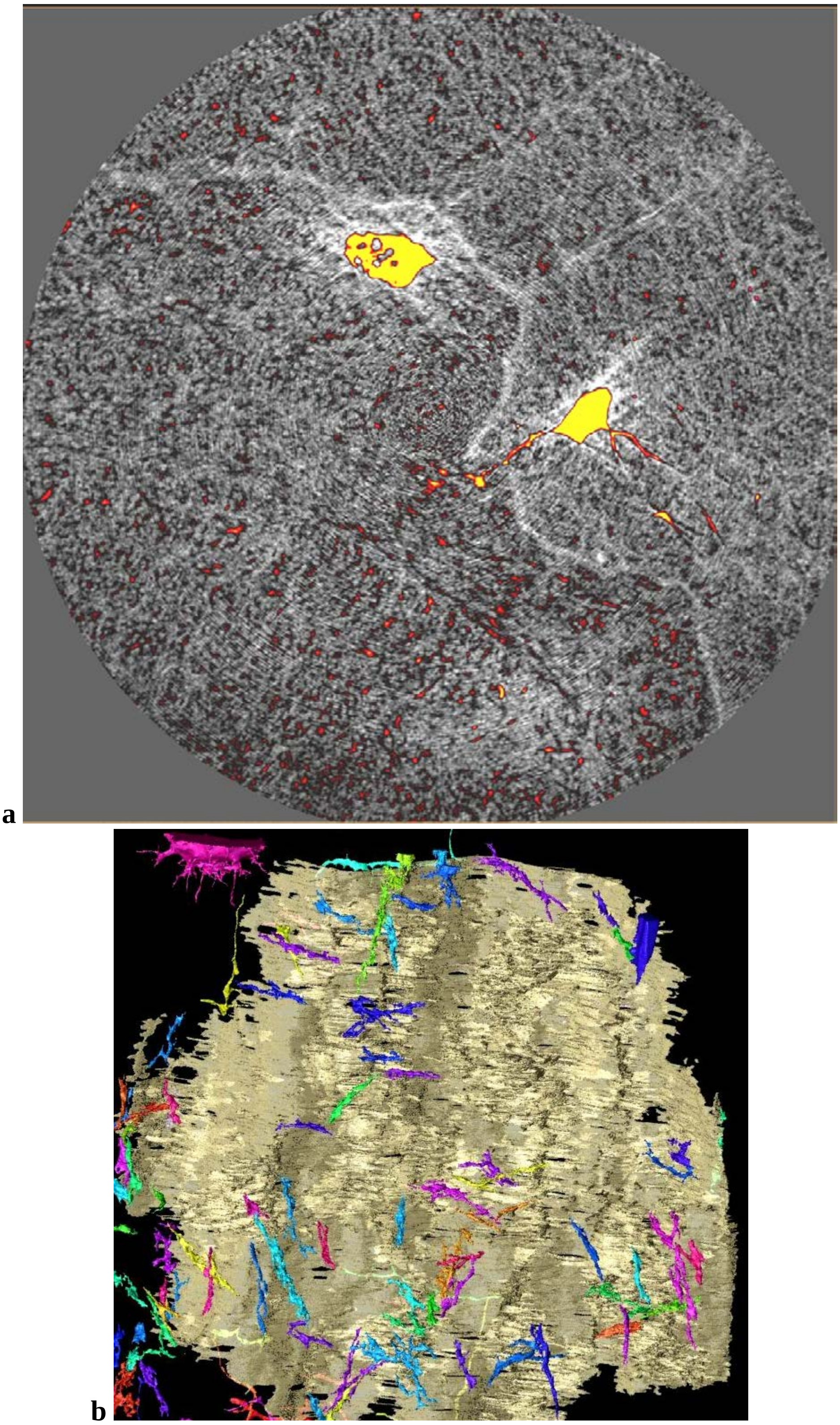

Figure 64 Slice and 3D rendering showing nanoporosities in the bone matrix of interstitial tissue. a) Slice showing that in the matrix of older tissue (left side of the cement line) there are more and bigger spaces (orange). Image width is 90 µm. b) 3D rendering showing the shape, size and distribution of these spaces which seem to be similar to collagen fibres. In beige is the cement line.

We proposed as well, the application of a new technique, called magnified holotomography, to image the bone tissue at a higher spatial resolution. This technique makes use of a focused X-ray beam to attain spatial resolutions down to a few tens of nanometers. The image is reconstructed from phase maps, calculated from radiographs recorded at different propagation distances downstream the sample, through dedicated algorithms. This technique enables, in addition to the imaging of the lacuno-canalicular network with higher accuracy (spatial resolution of 60 nm), to obtain 3D images of the collagen fibres in tissue covering 10 to 20 osteocyte lacunae (FOV ~100×100×100 μm^3). This makes possible to perform different studies. Based on the first acquired images, we could give some preliminary remarks. The collagen fibres seem to be better organized within osteons compared to the interstitial tissue. We observed that in the interstitial tissue the bone matrix is more mineralized in average and some of the collagen fibres seem to have been replaced by nanoporosities. This is shown in Figure 64 where we assigned a different color map to the porosity (in yellow are the cell lacunae, in orange are smaller porosities) (Figure 64a) and we rendered the surfaces of this type of porosities located within interstitial tissue (Figure 64b).

The imaging and image analysis methods proposed, applied and demonstrated in this thesis made possible to obtain unique images of the osteocyte lacuno-canalicular network and of human bone tissue at the nanoscale. Some preliminary observations and quantitative studies have been performed. The future work will focus on the accomplishment of a robust, fully automatic tool, for image segmentation and quantification, dedicated to the lacuno-canalicular structure. This paves the way to unprecedented studies with applications in biology, biomechanics, medicine or biomaterials.

Chapter 11 ANNEX I

Segmentation of 3D cellular networks from SR-micro-CT images

Alexandra Pacureanu, Jérôme Rollet, Chantal Revol-Muller, Vasile Buzuloiu, Max Langer, Françoise Peyrin

Paper published in the Proceedings of the IEEE International Symposium of Biomedical Imaging, 2011

Abstract

Bone fragility involved in diseases such as osteoporosis implicates many mechanisms at the cellular level. It was recently shown that the lacunar-canalicular network interconnecting osteocytes has a major role in mechanosensitivity. So far, this system has only been studied from 2D microscopic images. In a previous work, we demonstrated the feasibility of synchrotron radiation micro-CT with a voxel size of 0.28µm, to image the lacunar-canalicular porosity in 3D. Nevertheless, the segmentation of this dense network of slender channels with average diameters of ~300-900 nanometers, at the limit of the spatial resolution, is difficult. In this work we propose a level set based method to automatically segment this complex system. To this aim, we designed an automatic initialization process and we apply a post-processing filter. Quantitative results on a ground truth prepared image are presented. On real data sets, expert evaluation showed good results.

ANNEX II Additional images

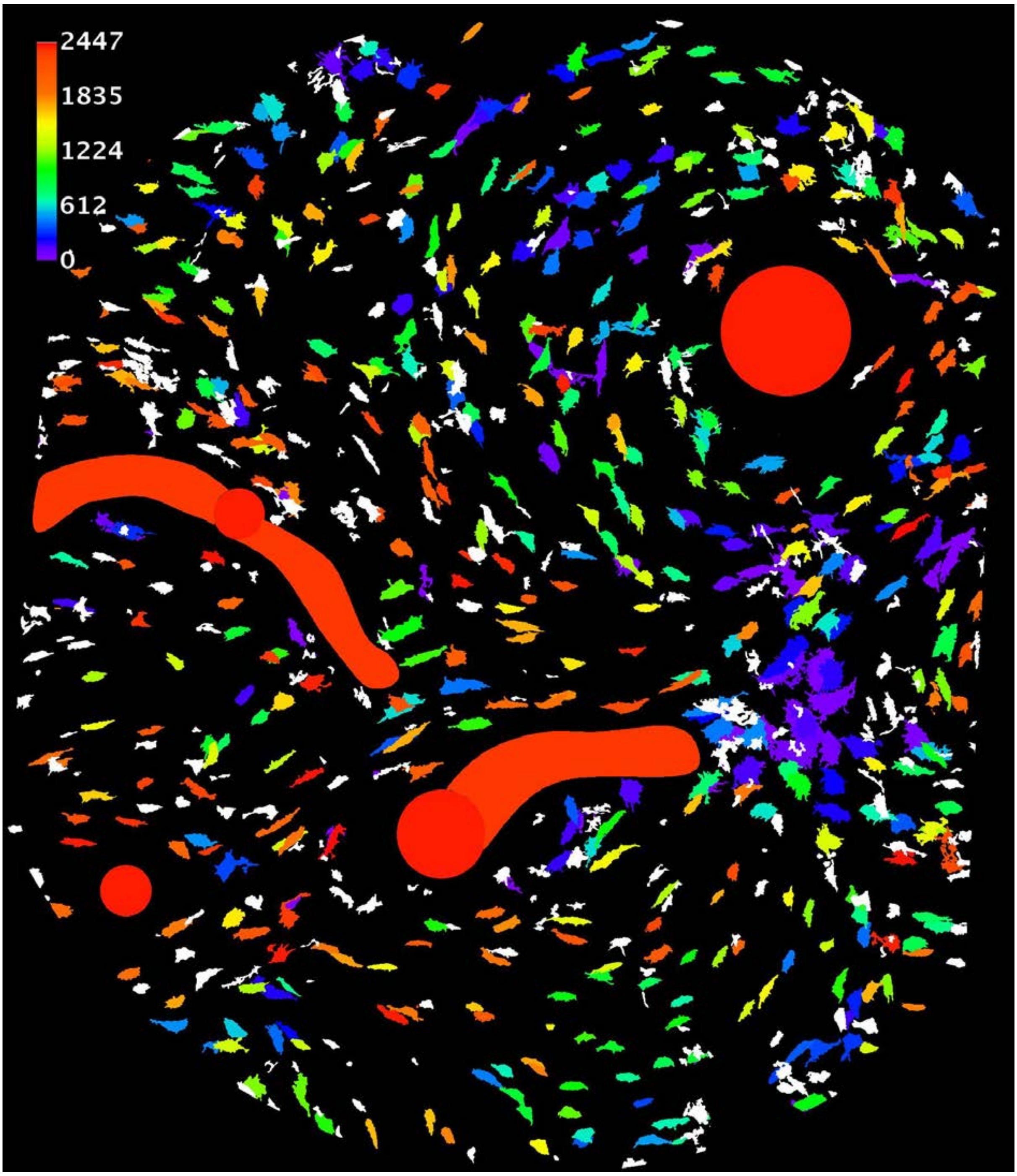

Figure 65 Maximum intensity projection over 400 slices (112 µm) from the labeled image obtained after segmentation of the cell lacunae followed by connected components analysis. The color map (rainbow) is related to the size of the objects in the image. The smallest lacunae are white and the biggest are indigo. The image suggests that lacunae close to the Haversian canal tend to be smaller and the lacunae close to the outer border of the osteons tend to be bigger. Please note that the vessel canals have been removed during the segmentation and in the shown image the canals have been added artificially at the end of the analysis, with the purpose to indicate the rough location of the canals in the experimental image. Pixel size was 280 nm.

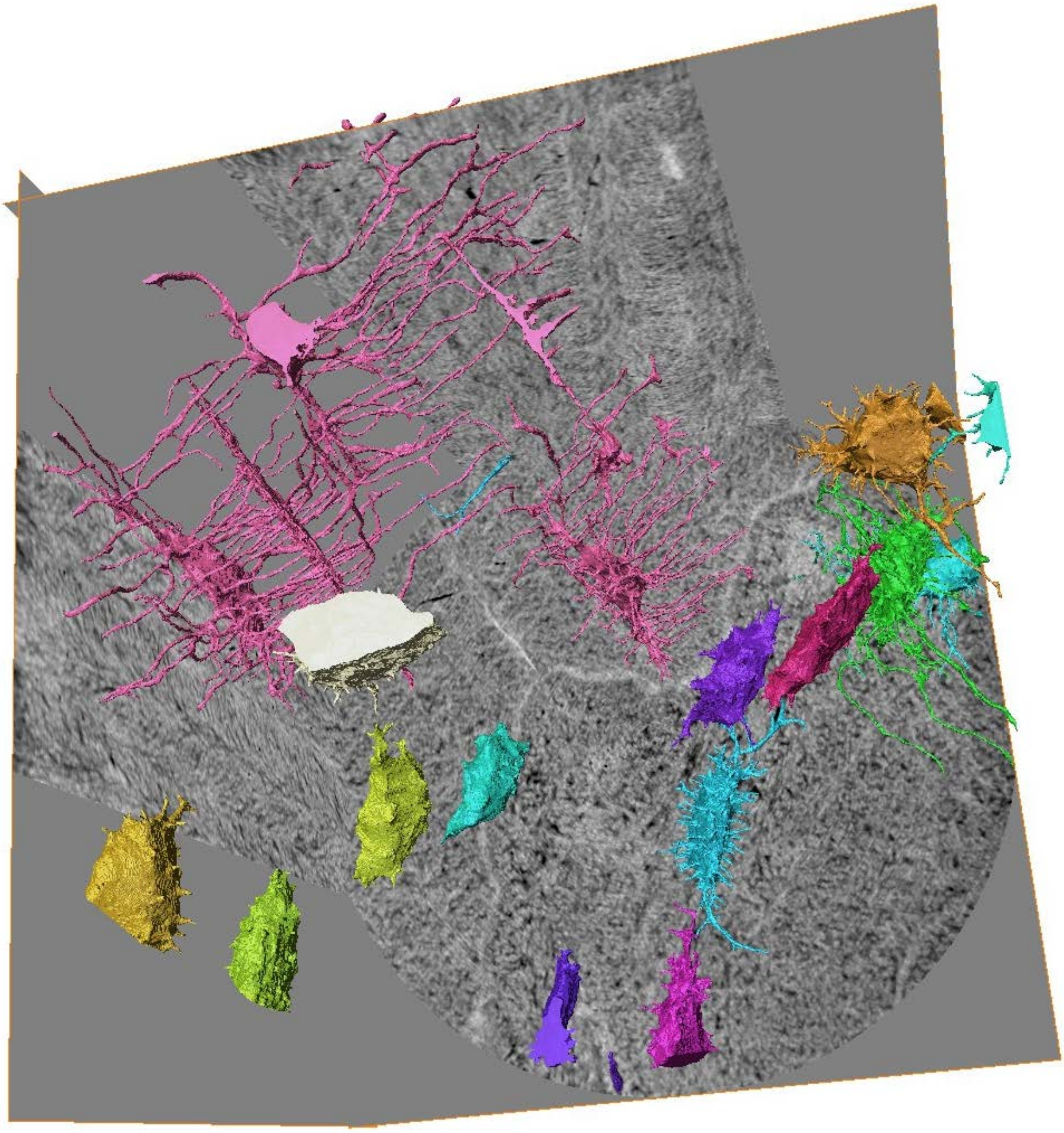

Figure 66 Three-dimensional rendering of the segmented osteocyte lacuno-canalicular network in a human bone specimen. The cell lacunae are distributed in both osteonal tissue and interstitial tissue. Inside the osteons the cell network is connected whilst in the interstitial tissue the network is disrupted. Pixel size was 60 nm.

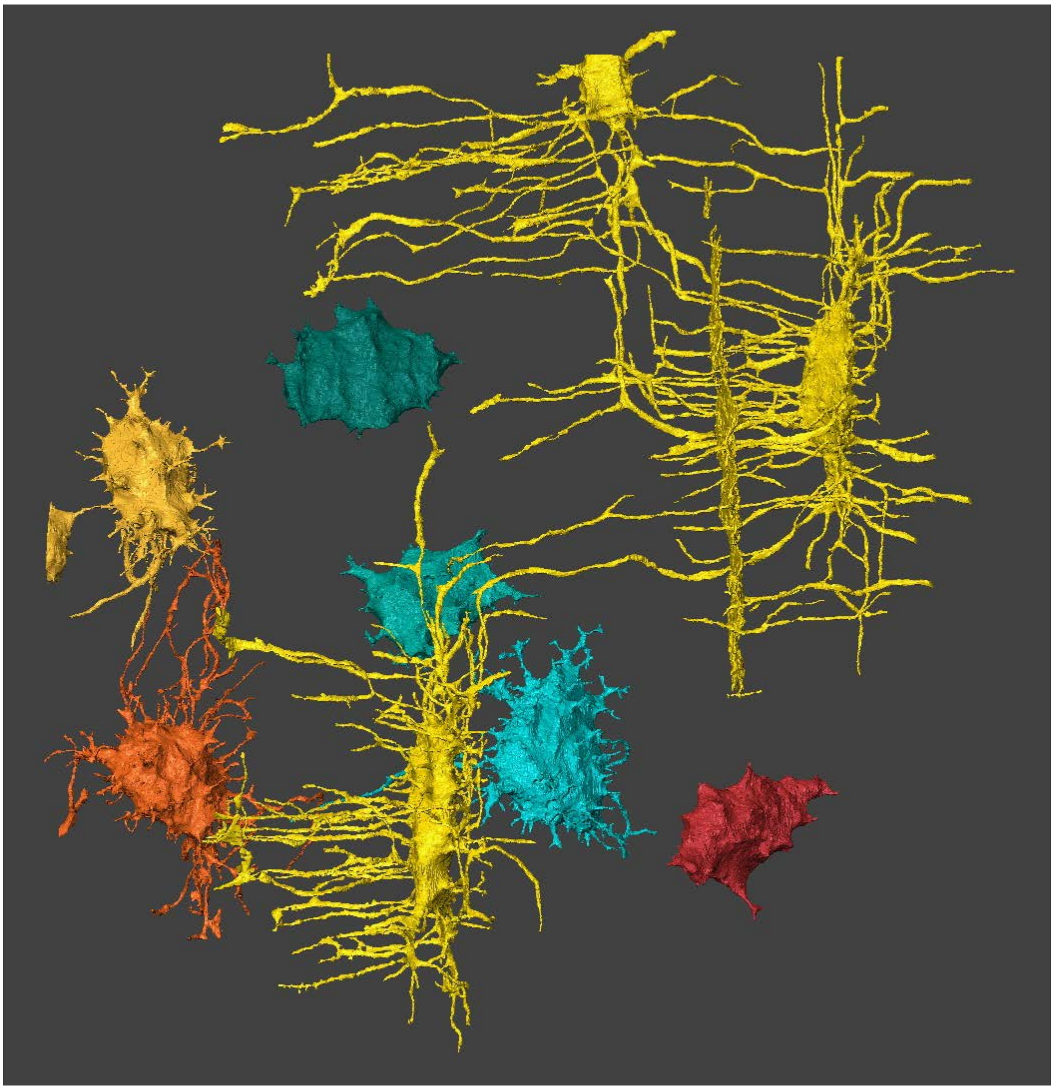

Figure 67 Supplementary image showing the labeled osteocyte lacunae and canaliculi. The colors indicate connected components. Pixel size was 60 nm.

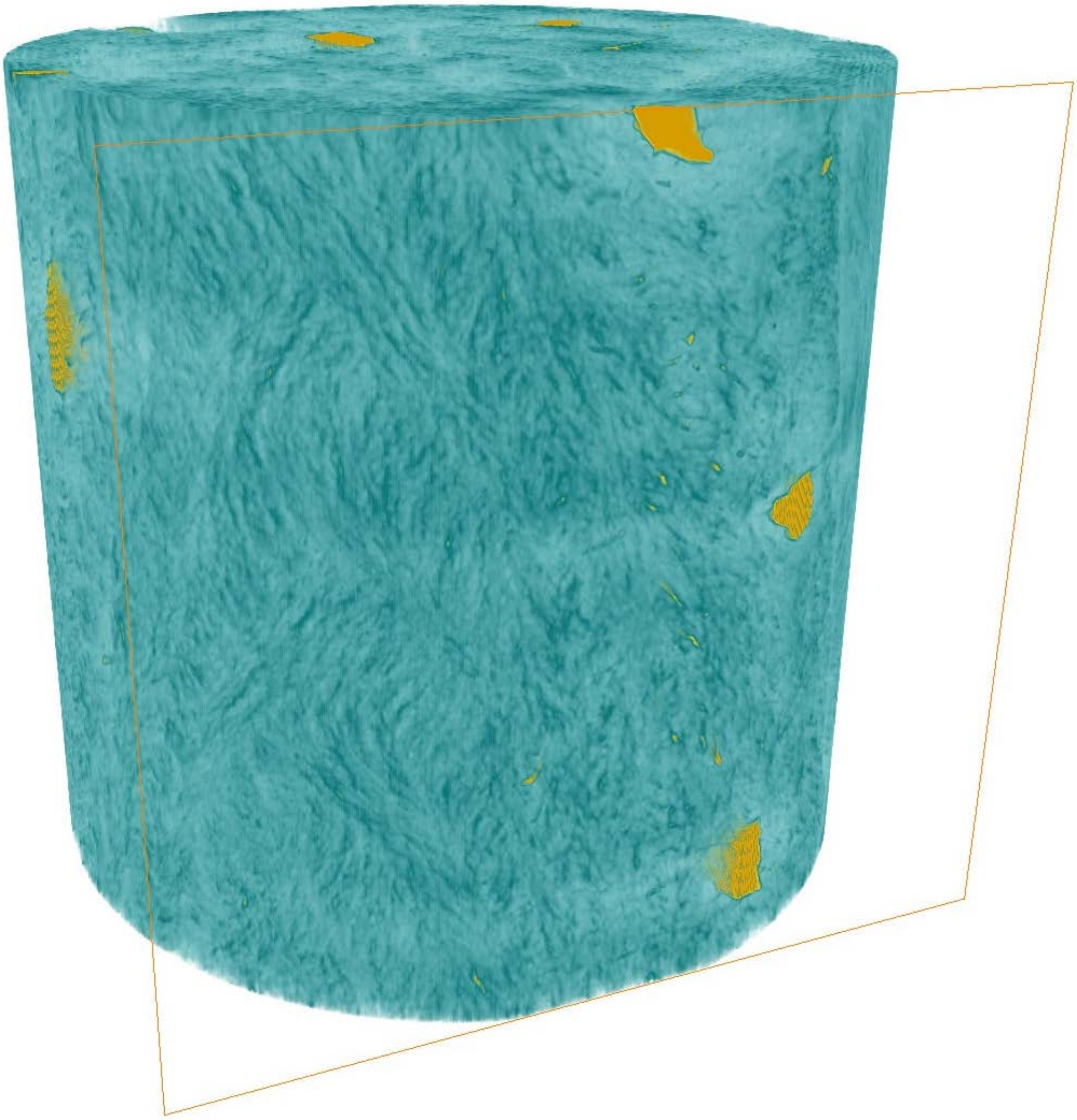

Figure 68 Three-dimensional rendering of the 3D complex refractive index distribution in a human cortical bone specimen. In orange is represented the osteocyte lacuno-canalicular porosity. The darker blue regions correspond to collagen fibres in the bone matrix. The lighter blue stands for the mineral part of the bone matrix, constituted of hydroxylapatite crystals. Pixel size was 60 nm.

Figure 69 Frontal section through the volume rendering. One can observe that around the cell lacunae the bone matrix appears denser, hence higher degree of mineralization. Pixel size was 60 nm.

Figure 70 The detector and the sample stage for high resolution tomography, in the experimental hutch of the beamline ID19 at ESRF.

References

ADACHI, T., AONUMA, Y., TANAKA, M., HOJO, M., TAKANO-YAMAMOTO, TERUKO & KAMIOKA, HIROSHI (2009). Calcium response in single osteocytes to locally applied mechanical stimulus: Differences in cell process and cell body. *Journal of Biomechanics* **42**, 1989-1995.

ALS-NIELSEN, J. & MCMORROW, D. (2011). *Elements of Modern X-ray Physics*. Hoboken, NJ, USA: John Wiley & Sons, Inc.

ANDREWS, J. C., ALMEIDA, E., VAN DER MEULEN, M. C. H., ALWOOD, J. S., LEE, C., LIU, Y., CHEN, J., MEIRER, F., FESER, M., GELB, J., RUDATI, J., TKACHUK, A., YUN, W. & PIANETTA, P. (2010). Nanoscale X-ray microscopic imaging of mammalian mineralized tissue. *Microscopy and Microanalysis: The Official Journal of Microscopy Society of America, Microbeam Analysis Society, Microscopical Society of Canada* **16**, 327-336.

ARDIZZONI, A. (2001). Osteocyte lacunar size-lamellar thickness relationships in human secondary osteons. *Bone* **28**, 215-219.

ARHATARI, B. D., COOPER, D. M. L., THOMAS, C. D. L., CLEMENT, J. G. & PEELE, A. G. (2011). Imaging the 3D structure of secondary osteons in human cortical bone using phase-retrieval tomography. *Physics in Medicine and Biology* **56**, 5265-5274.

ASCENZI, M. G., ASCENZI, A., BENVENUTI, A., BURGHAMMER, M., PANZAVOLTA, S. & BIGI, A. (2003). Structural differences between “dark” and “bright” isolated human osteonic lamellae. *Journal of Structural Biology* **141**, 22-33.

ATKINSON, P. J. & HALLSWORTH, A. S. (1982). The Spatial Structure of Bone. *Progress in Anatomy* **2**, 179-199.

ATTIX, F. H. (1986). *Introduction to Radiological Physics and Radiation Dosimetry*. Weinheim, Germany: Wiley-VCH Verlag GmbH .

BARTH, H. D., LAUNEY, M. E., MACDOWELL, A. A., AGER, J. W., 3RD & RITCHIE, R. O. (2010). On the effect of X-ray irradiation on the deformation and fracture behavior of human cortical bone. *Bone* **46**, 1475-1485.

BENMANSOUR, F. & COHEN, LAURENT D. (2010). Tubular Structure Segmentation Based on Minimal Path Method and Anisotropic Enhancement. *International Journal of Computer Vision* **92**, 192-210.

BENO, T., YOON, Y.-J., COWIN, S. C. & FRITTON, S. P. (2006). Estimation of bone permeability using accurate microstructural measurements. *Journal of Biomechanics* **39**, 2378-2387.

BILDERBACK, D. H., ELLEAUME, P. & WECKERT, E. (2005). Review of third and next generation synchrotron light sources. *Journal of Physics B: Atomic, Molecular and Optical Physics* **38**, S773-S797.

BILEZIKIAN, J. P., RAISZ, L. G. & RODAN, G. A. (2002). *Principles of bone biology*. Elsevier.

BLEUET, P., CLOETENS, PETER, GERGAUD, P., MARIOLLE, D., CHEVALIER, N., TUCOULOU, R., SUSINI, J. & CHABLI, A. (2009). A hard x-ray nanoprobe for scanning and projection nanotomography. *Review of Scientific Instruments* **80**, 056101.

BONEWALD, L. F. (2011). The amazing osteocyte. *Journal of Bone and Mineral Research* **26**, 229-238.

BONSE, U. & BUSCH, F. (1996). X-ray computed microtomography (microCT) using synchrotron radiation (SR). *Progress in Biophysics and Molecular Biology* **65**, 133-169.

BONSE, U. & HART, M. (1965). AN X-RAY INTERFEROMETER. *Applied Physics Letters* **6**, 155.

BOSSY, E., TALMANT, M., PEYRIN, FRANÇOISE, AKROUT, L., CLOETENS, PETER & LAUGIER, P. (2004). An In Vitro Study of the Ultrasonic Axial Transmission Technique at the Radius: 1 MHz Velocity Measurements Are Sensitive to Both Mineralization and Intracortical Porosity. *Journal of Bone and Mineral Research* **19**, 1548-1556.

BOUSSON, V., PEYRIN, FRANÇOISE, BERGOT, C., HAUSARD, M., SAUTET, A. & LAREDO, J.-D. (2004). Cortical Bone in the Human Femoral Neck: Three-Dimensional Appearance and Porosity Using Synchrotron Radiation. *Journal of Bone and Mineral Research* **19**, 794-801.

BOYDE, A., HENDEL, P., HENDEL, R., MACONNACHIE, E. & JONES, S. J. (1990). Human cranial bone structure and the healing of cranial bone grafts: a study using backscattered electron imaging and confocal microscopy. *Anatomy and Embryology* **181**.

BOYDE, ALAN (2003). The real response of bone to exercise. *Journal of Anatomy* **203**, 173-189.

BOYLE, W. J., SIMONET, W. S. & LACEY, D. L. (2003). Osteoclast differentiation and activation. *Nature* **423**, 337-342.

BRACEWELL, R. N. (1956). Strip Integration in Radio Astronomy. *Australian Journal of Physics* **9**, 198.

BROMAGE, T. G., GOLDMAN, H. M., MCFARLIN, S. C., WARSHAW, J., BOYDE, ALAN & RIGGS, C. M. (2003). Circularly polarized light standards for investigations of collagen fiber orientation in bone. *The Anatomical Record Part B: The New Anatomist* **274B**, 157-168.

BURGER, ELISABETH H. & KLEIN-NULEND, JENNEKE (1999). Mechanotransduction in bone - role of the lacuno-canalicular network. *FASEB J.* **13**, 101-112.

BURGER, ELISABETH H., KLEIN-NULEND, JENNEKE & SMIT, T. H. (2003). Strain-derived canalicular fluid flow regulates osteoclast activity in a remodelling osteon—a proposal. *Journal of Biomechanics* **36**, 1453-1459.

BURRA, S., NICOLELLA, D. P., FRANCIS, W. L., FREITAS, C. J., MUESCHKE, N. J., POOLE, K. & JIANG, J. X. (2010). Dendritic processes of osteocytes are mechanotransducers that induce the opening of hemichannels. *Proceedings of the National Academy of Sciences* **107**, 13648 -13653.

BUSSE, B., DJONIC, D., MILOVANOVIC, P., HAHN, M., PÜSCHEL, K., RITCHIE, R. O., DJURIC, M. & AMLING, M. (2010). Decrease in the osteocyte lacunar density accompanied by hypermineralized lacunar occlusion reveals failure and delay of remodeling in aged human bone. *Aging Cell* **9**, 1065-1075.

CASELLES, V., KIMMEL, R. & SAPIRO, G. (1995). Geodesic active contours. In *Computer Vision, IEEE International Conference on*vol. 0, p. 694. Los Alamitos, CA, USA: IEEE Computer Society.

CHAKRABORTY, A., STAIB, L. H. & DUNCAN, J. S. (1996). Deformable boundary finding in medical images by integrating gradient and region information. *IEEE Transactions on Medical Imaging* **15**, 859-870.

CHAN, T. F. & VESE, L. A. (2001). Active Contours without Edges. *IEEE Transactions on Image Processing,* **10**, 266-277.

CHAPMAN, D., THOMLINSON, W., JOHNSTON, R. E., WASHBURN, D., PISANO, E., GMÜR, N., ZHONG, Z., MENK, R., ARFELLI, F. & SAYERS, D. (1997). Diffraction enhanced x-ray imaging. *Physics in Medicine and Biology* **42**, 2015-2025.

CIANI, C., DOTY, S. B. & FRITTON, S. P. (2009). An effective histological staining process to visualize bone interstitial fluid space using confocal microscopy. *Bone* **44**, 1015-1017.

CLOETENS, P., LUDWIG, W., BARUCHEL, J., VAN DYCK, D., VAN LANDUYT, J., GUIGAY, J. P. & SCHLENKER, M. (1999). Holotomography: Quantitative phase tomography with micrometer resolution using hard synchrotron radiation x rays. *Applied Physics Letters* **75**, 2912.

CLOETENS, P., PATEYRON-SALOMÉ, M., BUFFIÈRE, J. Y., PEIX, G., BARUCHEL, J., PEYRIN, F. & SCHLENKER, M. (1997). Observation of microstructure and damage in materials by phase sensitive radiography and tomography. *Journal of Applied Physics* **81**, 5878.

CLOETENS, P. (1999). *Contribution to phase contrast imaging, reconstruction and tomography with hard synchrotron radition*. Vrije Universiteit Brussel & ESRF.

CORMACK, A. M. (1964). Representation of a Function by Its Line Integrals, with Some Radiological Applications. II. *Journal of Applied Physics* **35**, 2908-2913.

COSIER, J. & GLAZER, A. M. (1986). A nitrogen-gas-stream cryostat for general X-ray diffraction studies. *Journal of Applied Crystallography* **19**, 105-107.

CURREY, J. D. (2003). The many adaptations of bone. *Journal of Biomechanics* **36**, 1487-1495.

DAVID, C., NÖHAMMER, B., SOLAK, H. H. & ZIEGLER, E. (2002). Differential x-ray phase contrast imaging using a shearing interferometer. *Applied Physics Letters* **81**, 3287.

DIEROLF, M., MENZEL, A., THIBAULT, P., SCHNEIDER, P., KEWISH, C. M., WEPF, R., BUNK, O. & PFEIFFER, F. (2010). Ptychographic X-ray computed tomography at the nanoscale. *Nature* **467**, 436-439.

DIJKSTRA, E. W. (1959). A note on two problems in connexion with graphs. *Numerische Mathematik* **1**, 269-271.

DOUISSARD, P. A., CECILIA, ANGELICA, MARTIN, THIERRY, CHEVALIER, V., COUCHAUD, MAURICE, BAUMBACH, TILO, DUPRÉ, K., KÜHBACHER, M. & RACK, ALEXANDER (2010). A novel epitaxially grown LSO-based thin-film scintillator for micro-imaging using hard synchrotron radiation. *Journal of Synchrotron Radiation* **17**, 571-583.

ELDER, F. R., GUREWITSCH, A. M., LANGMUIR, R. V. & POLLOCK, H. C. (1947). Radiation from Electrons in a Synchrotron. *Physical Review* **71**, 829-830.

ELLIOTT, J. C. & DOVER, S. D. (1982). X-ray microtomography. *Journal of Microscopy* **126**, 211-213.

ERNI, R., ROSSELL, M. D., KISIELOWSKI, C. & DAHMEN, U. (2009). Atomic-Resolution Imaging with a Sub-50-pm Electron Probe. *Physical Review Letters* **102**, 096101.

FLANNERY, B. P., DECKMAN, H. W., ROBERGE, W. G. & D'AMICO, K. L. (1987). Three-Dimensional X-ray Microtomography. *Science* **237**, 1439 -1444.

FRANGI, A., NIESSEN, W., VINCKEN, K. & VIERGEVER, M. (1998). Multiscale Vessel Enhancement Filtering. In *Medical Image Computing and Computer-Assisted Interventation — MICCAI'98*, p. 130. .

FRANZ ODENDAAL, T. A., HALL, B. K. & WITTEN, P. E. (2006). Buried alive: How osteoblasts become osteocytes. *Developmental Dynamics* **235**, 176-190.

FROST, H. M. (1960). Micropetrosis. *The Journal of Bone and Joint Surgery. American Volume* **42-A**, 144-150.

FROST, H. M. (1987). Secondary osteon populations: An algorithm for determining mean bone tissue age. *American Journal of Physical Anthropology* **30**, 221-238.

GABOR, D. (1949). Microscopy by Reconstructed Wave-Fronts. *Proceedings of the Royal Society A: Mathematical, Physical and Engineering Sciences* **197**, 454-487.

GARCIA, M.-P., TOUMOULIN, C., HAIGRON, P., VELUT, J., GARREAU, M. & BOULMIER, D. (2010). CORONARY VEIN TRACKING FROM MSCT USING A MINIMUM COST PATH APPROACH. In *2010 7th Ieee International Symposium on Biomedical Imaging: From Nano*, pp. 17-20. New York: Ieee.

GIRAUD-GUILLE, M.-M., BESSEAU, L. & MARTIN, R. (2003). Liquid crystalline assemblies of collagen in bone and in vitro systems. *Journal of Biomechanics* **36**, 1571-1579.

GRANKE, M., GRIMAL, Q., SAÏED, A., NAULEAU, P., PEYRIN, FRANÇOISE & LAUGIER, P. (2011). Change in porosity is the major determinant of the variation of cortical bone elasticity at the millimeter scale in aged women. *Bone* **49**, 1020-1026.

GUIGAY, JEAN PIERRE, LANGER, MAX, BOISTEL, R. & CLOETENS, PETER (2007). Mixed transfer function and transport of intensity approach for phase retrieval in the Fresnel region. *Optics Letters* **32**, 1617-1619.

GUINIER, A. (1994). *X-ray diffraction in crystals, imperfect crystals, and amorphous bodies*. Courier Dover Publications.

HAN, Y., COWIN, S. C., SCHAFFLER, M. B. & WEINBAUM, S. (2004). Mechanotransduction and strain amplification in osteocyte cell processes. *Proceedings of the National Academy of Sciences of the United States of America* **101**, 16689 -16694.

HANNAH, K. M., THOMAS, C. D. L., CLEMENT, J. G., DE CARLO, F. & PEELE, A. G. (2010). Bimodal distribution of osteocyte lacunar size in the human femoral cortex as revealed by micro-CT. *Bone* **47**, 866-871.

HAZENBERG, J. G., FREELEY, M., FORAN, E., LEE, THOMAS C. & TAYLOR, D. (2006). Microdamage: A cell transducing mechanism based on ruptured osteocyte processes. *Journal of Biomechanics* **39**, 2096-2103.

HERNANDEZ, M. & FRANGI, A. F. (2007). Non-parametric geodesic active regions: Method and evaluation for cerebral aneurysms segmentation in 3DRA and CTA. *Medical Image Analysis* **11**, 224-241.

HILLER, L. P., STOVER, S. M., GIBSON, V. A., GIBELING, J. C., PRATER, C. S., HAZELWOOD, S. J., YEH, O. C. & MARTIN, R. B. (2003). Osteon pullout in the equine third metacarpal bone: Effects of ex vivo fatigue. *Journal of Orthopaedic Research* **21**, 481-488.

HOFMANN, T., HEYROTH, F., MEINHARD, H., FRÄNZEL, W. & RAUM, K. (2006). Assessment of composition and anisotropic elastic properties of secondary osteon lamellae. *Journal of Biomechanics* **39**, 2282-2294.

HOPPE (1974). Towards three-dimensional "electron microscopy" at atomic resolution. *Die Naturwissenschaften* **61**, 239-249.

HOPPE, W. (1982). Trace structure analysis, ptychography, phase tomography. *Ultramicroscopy* **10**, 187-198.

HOSHEN, J. & KOPELMAN, R. (1976). Percolation and cluster distribution. I. Cluster multiple labeling technique and critical concentration algorithm. *Physical Review B* **14**, 3438.

HOUNSFIELD, G. N. (1973). Computerized transverse axial scanning (tomography). 1. Description of system. *The British Journal of Radiology* **46**, 1016-1022.

VAN HOVE, R. P., NOLTE, P. A., VATSA, A., SEMEINS, C. M., SALMON, P. L., SMIT, T. H. & KLEIN-NULEND, JENNEKE (2009). Osteocyte morphology in human tibiae of different bone pathologies with different bone mineral density--is there a role for mechanosensing? *Bone* **45**, 321-329.

HUA LI & YEZZI, A. (2007). Vessels as 4-D Curves: Global Minimal 4-D Paths to Extract 3-D Tubular Surfaces and Centerlines. *IEEE Transactions on Medical Imaging* **26**, 1213-1223.

HUISKES, R. (2000). If bone is the answer, then what is the question? *Journal of Anatomy* **197**, 145-156.

HUISKES, RIK, RUIMERMAN, R., VAN LENTHE, G. H. & JANSSEN, J. D. (2000). Effects of mechanical forces on maintenance and adaptation of form in trabecular bone. *Nature* **405**, 704-706.

INGAL, V. N. & BELIAEVSKAYA, E. A. (1995). X-ray plane-wave topography observation of the phase contrast from a non-crystalline object. *Journal of Physics D: Applied Physics* **28**, 2314-2317.

JEHAN-BESSON, S., BARLAUD, M. & AUBERT, G. (2002). DREAM^{2}S: Deformable Regions Driven by an Eulerian Accurate Minimization Method for Image and Video Segmentation. *IN ECCV* **53**, 365--380.

KIRKPATRICK, P. & BAEZ, A. V. (1948). Formation of Optical Images by X-Rays. *Journal of the Optical Society of America* **38**, 766-773.

KAK, A. C. & SLANEY, M. (1988). *Principles of computerized tomographic imaging*. IEEE Press.

Kamioka, H., Honjo, T. & Takano-Yamamoto, T. (2001). A three-dimensional distribution of osteocyte processes revealed by the combination of confocal laser scanning microscopy and differential interference contrast microscopy. *Bone* **28**, 145-149.

Kamioka, Hiroshi, Murshid, S. A., Ishihara, Y., Kajimura, N., Hasegawa, T., Ando, R., Sugawara, Y., Yamashiro, T., Takaoka, A. & Takano-Yamamoto, Teruko (2009). A method for observing silver-stained osteocytes in situ in 3-microm sections using ultra-high voltage electron microscopy tomography. *Microscopy and Microanalysis: The Official Journal of Microscopy Society of America, Microbeam Analysis Society, Microscopical Society of Canada* **15**, 377-383.

Kass, M., Witkin, A. & Terzopoulos, D. (1988). Snakes: Active contour models. *INTERNATIONAL JOURNAL OF COMPUTER VISION* **1**, 321--331.

Kazanci, M., Roschger, P., Paschalis, E. P., Klaushofer, K. & Fratzl, P. (2006). Bone osteonal tissues by Raman spectral mapping: Orientation-composition. *Journal of Structural Biology* **156**, 489-496.

Kerschnitzki, M., Wagermaier, W., Roschger, Paul, Seto, J., Shahar, R., Duda, G. N., Mundlos, S. & Fratzl, Peter (2011). The organization of the osteocyte network mirrors the extracellular matrix orientation in bone. *Journal of Structural Biology* **173**, 303-311.

Kingsmill, V. J. & Boyde, A. (1998). Mineralisation density of human mandibular bone: quantitative backscattered electron image analysis. *Journal of Anatomy* **192**, 245-256.

Klein-Nulend, J., Bacabac, R. G., Veldhuijzen, J. P. & Van Loon, J. J. W. A. (2003). Microgravity and bone cell mechanosensitivity. *Advances in Space Research* **32**, 1551-1559.

Klein-Nulend, J, van der Plas, A., Semeins, C., Ajubi, N., Frangos, J., Nijweide, P. & Burger, E. (1995). Sensitivity of osteocytes to biomechanical stress in vitro. *The FASEB Journal* **9**, 441 -445.

Knothe Tate, Melissa L. (2003). “Whither flows the fluid in bone?” An osteocyte’s perspective. *Journal of Biomechanics* **36**, 1409-1424.

Knothe Tate, Melissa L., Adamson, J. R., Tami, A. E. & Bauer, Thomas W. (2004). The osteocyte. *The International Journal of Biochemistry & Cell Biology* **36**, 1-8.

Knothe Tate, M. L., Bauer, T. W., Tami, A. E. G. & Knothe, U. (2002). Micropathoanatomy of osteoporosis:indications for a cellular basis of bone disease. *Advances in Osteoporotic Fracture Management* **2**, 10,11.

Kubek, D. J., Gattone, V. H., 2nd & Allen, M. R. (2010). Methodological assessment of acid-etching for visualizing the osteocyte lacunar-canalicular networks using scanning electron microscopy. *Microscopy Research and Technique* **73**, 182-186.

KUSUZAKI, K., KAGEYAMA, N., SHINJO, H., TAKESHITA, H., MURATA, H., HASHIGUCHI, S., ASHIHARA, T. & HIRASAWA, Y. (2000). Development of bone canaliculi during bone repair. *Bone* **27**, 655-659.

LABICHE, J.-C., MATHON, O., PASCARELLI, S., NEWTON, M. A., FERRE, G. G., CURFS, C., VAUGHAN, G., HOMS, A. & CARREIRAS, D. F. (2007). Invited article: The fast readout low noise camera as a versatile x-ray detector for time resolved dispersive extended x-ray absorption fine structure and diffraction studies of dynamic problems in materials science, chemistry, and catalysis. *Review of Scientific Instruments* **78**, 091301.

LANE, N. E., YAO, W., BALOOCH, M., NALLA, R. K., BALOOCH, G., HABELITZ, S., KINNEY, J. H. & BONEWALD, L. F. (2005). Glucocorticoid-Treated Mice Have Localized Changes in Trabecular Bone Material Properties and Osteocyte Lacunar Size That Are Not Observed in Placebo-Treated or Estrogen-Deficient Mice. *Journal of Bone and Mineral Research* **21**, 466-476.

LANGER, M., CLOETENS, P. & PEYRIN, F. (2010). Regularization of Phase Retrieval With Phase-Attenuation Duality Prior for 3-D Holotomography. *IEEE Transactions on Image Processing* **19**, 2428-2436.

LARRUE, A., RATTNER, A., PETER, Z.-A., OLIVIER, C., LAROCHE, N., VICO, L. & PEYRIN, FRANÇOISE (2011). Synchrotron Radiation Micro-CT at the Micrometer Scale for the Analysis of the Three-Dimensional Morphology of Microcracks in Human Trabecular Bone. *PLoS ONE* **6**, e21297.

LESAGE, D., ANGELINI, E. D., BLOCH, I. & FUNKA-LEA, G. (2009). A review of 3D vessel lumen segmentation techniques: Models, features and extraction schemes. *Medical Image Analysis* **13**, 819-845.

LIN, Y. & XU, S. (2010). AFM analysis of the lacunar-canalicular network in demineralized compact bone. *Journal of Microscopy* no-no.

LORENZ, C., CARLSEN, I.-C., BUZUG, T. M., FASSNACHT, C. & WEESE, J. (1997). Multi-scale line segmentation with automatic estimation of width, contrast and tangential direction in 2D and 3D medical images. In *CVRMed-MRCAS'97*vol. 1205, Troccaz, J., Grimson, E. & Mösges, R. (Eds.), pp. 233-242.

MAIRE, E., BUFFIÈRE, J. Y., SALVO, L., BLANDIN, J. J., LUDWIG, W. & LÉTANG, J. M. (2001). On the Application of X-ray Microtomography in the Field of Materials Science. *Advanced Engineering Materials* **3**, 539-546.

MALLADI, R., SETHIAN, JAMES A & VEMURI, B. C. (1995). Shape modeling with front propagation: A level set approach. *IEEE TRANSACTIONS ON PATTERN ANALYSIS AND MACHINE INTELLIGENCE* **17**, 158--175.

MAROTTI, G. (1977). Decrement in volume of osteoblasts during osteon formation and its effect on the size of the corresponding osteocytes. *Meunier, P. J., Ed. Bone Histomorphometry* 385-397.

MAROTTI, G. (1979). Osteocyte orientation in human lamellar bone and its relevance to the morphometry of periosteocytic lacunae. *Metab Bone Dis Rel Res* 325–333.

MAROTTI, G. (1993). A new theory of bone lamellation. *Calcified Tissue International* **53 Suppl 1**, S47-55; discussion S56.

MAROTTI, G., FERRETTI, M., REMAGGI, F. & PALUMBO, C. (1995). Quantitative evaluation on osteocyte canalicular density in human secondary osteons. *Bone* **16**, 125-128.

MARTIN, THIERRY & KOCH, A. (2006). Recent developments in X-ray imaging with micrometer spatial resolution. *Journal of Synchrotron Radiation* **13**, 180-194.

MARTIN, T., DOUISSARD, P.-A., COUCHAUD, M., CECILIA, A., BAUMBACH, T., DUPRE, K. & RACK, A. (2009). LSO-Based Single Crystal Film Scintillator for Synchrotron-Based Hard X-Ray Micro-Imaging. *Nuclear Science, IEEE Transactions on* **56**, 1412-1418.

MISHRA, S. & KNOTHE TATE, MELISSA L (2003). Effect of lacunocanalicular architecture on hydraulic conductance in bone tissue: implications for bone health and evolution. *The Anatomical Record. Part A, Discoveries in Molecular, Cellular, and Evolutionary Biology* **273**, 752-62.

MOMOSE, A. (2003). Phase-sensitive imaging and phase tomography using X-ray interferometers. *Optics Express* **11**, 2303-2314.

MOREY, E. & BAYLINK, D. (1978). Inhibition of bone formation during space flight. *Science* **201**, 1138 -1141.

MULLENDER, M. G., VAN DER MEER, D. D., HUISKES, R & LIPS, P. (1996). Osteocyte density changes in aging and osteoporosis. *Bone* **18**, 109-113.

MULLER, R. (2009). Hierarchical microimaging of bone structure and function. *Nat Rev Rheumatol* **5**, 373-381.

NIJWEIDE, P. J., BURGER, E.H. & KLEIN NULEND, J. (2002). The Osteocyte. http://dare.uva.nl/record/103838 (Accessed March 31, 2009).

NUZZO, S., LAFAGE-PROUST, M. H., MARTIN-BADOSA, E., BOIVIN, G., THOMAS, T., ALEXANDRE, C. & PEYRIN, F. (2002). Synchrotron Radiation Microtomography Allows the Analysis of Three-Dimensional Microarchitecture and Degree of Mineralization of Human Iliac Crest Biopsy Specimens: Effects of Etidronate Treatment. *Journal of Bone and Mineral Research* **17**, 1372-1382.

OLABARRIAGA S.D., BREEUWER M. & NIESSEN W.J. (2003). Evaluation of Hessian-based filters to enhance the axis of coronary arteries in CT images. *International Congress Series* **1256**, 1191-1196.

OSHER, S. & SETHIAN, JAMES A. (1988). Fronts propagating with curvature-dependent speed: algorithms based on Hamilton-Jacobi formulations. *J. Comput. Phys.* **79**, 12–49.

PAGANIN, D., MAYO, S., GUREYEV, T., MILLER, P. & WILKINS, S. (2002). Simultaneous phase and amplitude extraction from a single defocused image of a homogeneous object RID B-9717-2009 RID A-4952-2010 RID A-9209-2011. *Journal of Microscopy-Oxford* **206**, 33-40.

PANNARALE, L., BRAIDOTTI, P., D' ALBA, L. & GAUDIO, E. (1994). Scanning electron microscopy of collagen fiber orientation in the bone lamellar system in non-decalcified human samples. *Acta Anatomica* **151**, 36-42.

PARAGIOS, N., DERICHE, R. & CEDEX, S. A. (1999). Geodesic Active Regions for Supervised Texture Segmentation. **2**, 926--932.

PAZZAGLIA, U. E., CONGIU, T., RASPANTI, M., RANCHETTI, F. & QUACCI, D. (2009). Anatomy of the intracortical canal system: scanning electron microscopy study in rabbit femur. *Clinical Orthopaedics and Related Research* **467**, 2446-2456.

PEYRIN, F (2009). Investigation of bone with synchrotron radiation imaging: from micro to nano. *Osteoporosis International: A Journal Established as Result of Cooperation Between the European Foundation for Osteoporosis and the National Osteoporosis Foundation of the USA* **20**, 1057-1063.

PFEIFFER, F., WEITKAMP, T., BUNK, O. & DAVID, CHRISTIAN (2006). Phase retrieval and differential phase-contrast imaging with low-brilliance X-ray sources. *Nat Phys* **2**, 258-261.

PLAMANN, T. & RODENBURG, J. M. (1998). Electron Ptychography. II. Theory of Three-Dimensional Propagation Effects. *Acta Crystallographica Section A Foundations of Crystallography* **54**, 61-73.

RAMACHANDRAN, G. N. & LAKSHMINARAYANAN, A. V. (1971). Three-dimensional Reconstruction from Radiographs and Electron Micrographs: Application of Convolutions instead of Fourier Transforms. *Proceedings of the National Academy of Sciences* **68**, 2236 -2240.

RAUM, K., CLEVELAND, R. O., PEYRIN, FRANÇOISE & LAUGIER, P. (2006). Derivation of elastic stiffness from site-matched mineral density and acoustic impedance maps. *Physics in Medicine and Biology* **51**, 747-758.

REILLY, G. C., KNAPP, H. F., STEMMER, A., NIEDERER, P. & KNOTHE TATE, MELISSA L. (2001). Investigation of the Morphology of the Lacunocanalicular System of Cortical Bone Using Atomic Force Microscopy. *Annals of Biomedical Engineering* **29**, 1074-1081.

RODENBURG, J. M. (2008). Ptychography and Related Diffractive Imaging Methods. vol. Volume 150, pp. 87-184. Elsevier .

ROSE, J.-L., REVOL-MULLER, C., ODET, CHRISTOPHE & REICHERT, C. (2010). Variational region growing. *VISAPP* **2**.

DE ROSIER, D. J. & KLUG, A. (1968). Reconstruction of Three Dimensional Structures from Electron Micrographs. *Nature* **217**, 130-134.

ROUCHDY, Y. & COHEN, L. D (2008). Image segmentation by geodesic voting. Application to the extraction of tree structures from confocal microscope images. In *19th International Conference on Pattern Recognition, 2008. ICPR 2008*, pp. 1-5. IEEE.

SAHOO, P. K., SOLTANI, S. & WONG, A. K. C. (1988). A survey of thresholding techniques. *Computer Vision, Graphics, and Image Processing* **41**, 233-260.

SALOME, M., PEYRIN, F, CLOETENS, P, ODET, C, LAVAL-JEANTET, A., BARUCHEL, J & SPANNE, P. (1999). A synchrotron radiation microtomography system for the analysis of trabecular bone samples. *Medical Physics* **26**, 2194-2204.

SALOMÉ, M., PEYRIN, F, CLOETENS, P, ODET, C, LAVAL-JEANTET, A. M., BARUCHEL, J & SPANNE, P. (1999). A synchrotron radiation microtomography system for the analysis of trabecular bone samples. *Medical Physics* **26**, 2194-2204.

SANCHEZ DEL RIO, M (2004). XOP 2.1: A new version of the X-ray optics software toolkit. *Synchrotron Radiation Instrumentation: Eighth International Conference* 784-787.

SATO, Y., NAKAJIMA, S., SHIRAGA, N., ATSUMI, H., YOSHIDA, S., KOLLER, T., GERIG, G. & KIKINIS, R. (1998). Three-dimensional multi-scale line filter for segmentation and visualization of curvilinear structures in medical images. *Medical Image Analysis* **2**, 143-168.

SCHAFFLER, M. B., BURR, D. B. & FREDERICKSON, R. G. (1987). Morphology of the osteonal cement line in human bone. *The Anatomical Record* **217**, 223-228.

SCHNEIDER, P., MEIER, M., WEPF, R. & MÜLLER, R. (2010). Towards quantitative 3D imaging of the osteocyte lacuno-canalicular network. *Bone* **47**, 848-858.

SCHNEIDER, P., MEIER, M., WEPF, R. & MÜLLER, R. (2011). Serial FIB/SEM imaging for quantitative 3D assessment of the osteocyte lacuno-canalicular network. *Bone* **49**, 304-311.

SCHNEIDER, P., STAUBER, M., VOIDE, R., STAMPANONI, M., DONAHUE, L. R. & MÜLLER, R. (2007). Ultrastructural Properties in Cortical Bone Vary Greatly in Two Inbred Strains of Mice as Assessed by Synchrotron Light Based Micro- and Nano-CT. *Journal of Bone and Mineral Research* **22**, 1557-1570.

SETHIAN, J. A (1995). A Fast Marching Level Set Method for Monotonically Advancing Fronts. *PROC. NAT. ACAD. SCI* **93**, 1591--1595.

SETHIAN, JAMES A. (2000). *Level set methods and fast marching methods: evolving interfaces in computational geometry, fluid mechanics, computer vision, and materials science*. Cambridge University Press.

SHAPIRO, F. (1988). Cortical bone repair. The relationship of the lacunar-canalicular system and intercellular gap junctions to the repair process. *J Bone Joint Surg Am* **70**, 1067-1081.

SKEDROS, J. G., HOLMES, J. L., VAJDA, E. G. & BLOEBAUM, R. D. (2005). Cement lines of secondary osteons in human bone are not mineral deficient: New data in a historical perspective. *The Anatomical Record Part A: Discoveries in Molecular, Cellular, and Evolutionary Biology* **286A**, 781-803.

SNIGIREV, A., SNIGIREVA, I., KOHN, V., KUZNETSOV, S. & SCHELOKOV, I. (1995). On the possibilities of x-ray phase contrast microimaging by coherent high-energy synchrotron radiation. *Review of Scientific Instruments* **66**, 5486.

STOKES, D. J., TONG, J. R., JUHASZ, J., MIDGLEY, P. A. & BEST, S. M. (2005). Characterisation and 3D Visualisation of Biomaterials and Tissues Using Focused Ion Beam (E)SEM. *Microscopy and Microanalysis* **11**, 1260-1261.

SUGAWARA, Y., KAMIOKA, HIROSHI, HONJO, TADASHI, TEZUKA, K.-ICHI & TAKANO-YAMAMOTO, TERUKO (2005). Three-dimensional reconstruction of chick calvarial osteocytes and their cell processes using confocal microscopy. *Bone* **36**, 877-83.

TANAKA-KAMIOKA, K., KAMIOKA, H, RIS, H. & LIM, S. (1998). Osteocyte shape is dependent on actin filaments and osteocyte processes are unique actin-rich projections. *Journal of Bone and Mineral Research* **13**, 1555-1568.

TAYLOR, D., HAZENBERG, J. G. & LEE, T. CLIVE (2007). Living with cracks: Damage and repair in human bone. *Nat Mater* **6**, 263-268.

TOMASI, C. & MANDUCHI, R. (1998). Bilateral filtering for gray and color images. In *Sixth International Conference on Computer Vision, 1998*, pp. 839-846. IEEE.

TOMKINSON, A., GEVERS, E. F., WIT, J. M., REEVE, J. & NOBLE, B. S. (1998). The Role of Estrogen in the Control of Rat Osteocyte Apoptosis. *Journal of Bone and Mineral Research* **13**, 1243-1250.

TURNER, C. H. (1998). Three rules for bone adaptation to mechanical stimuli. *Bone* **23**, 399-407.

VATSA, A., BREULS, R. G., SEMEINS, C. M., SALMON, P. L., SMIT, T. H. & KLEIN-NULEND, JENNEKE (2008). Osteocyte morphology in fibula and calvaria — Is there a role for mechanosensing? *Bone* **43**, 452-458.

WANG, L., WANG, Y., HAN, Y., HENDERSON, S. C., MAJESKA, R. J., WEINBAUM, S. & SCHAFFLER, M. B. (2005). In situ measurement of solute transport in the bone lacunar-canalicular system. *Proceedings of the National Academy of Sciences of the United States of America* **102**, 11911-6.

WEINSTEIN, R. S., JILKA, R. L., PARFITT, A. M. & MANOLAGAS, S. C. (1998). Inhibition of osteoblastogenesis and promotion of apoptosis of osteoblasts and osteocytes by glucocorticoids. Potential mechanisms of their deleterious effects on bone. *Journal of Clinical Investigation* **102**, 274-282.

WEITKAMP, T., DIAZ, A., DAVID, CHRISTIAN, PFEIFFER, F., STAMPANONI, M., CLOETENS, PETER & ZIEGLER, ERIC (2005). X-ray phase imaging with a grating interferometer. *Optics Express* **13**, 6296-6304.

WEITKAMP, T., TAFFOREAU, P., BOLLER, E., CLOETENS, PETER, VALADE, J.-P., BERNARD, P., PEYRIN, FRANCOISE, LUDWIG, WOLFGANG, HELFEN, L. & BARUCHEL, JOSE (2010). Status and evolution of the ESRF beamline ID19 Denecke, M. & Walker, C. T. (Eds.). *AIP Conference Proceedings* **1221**, 33-38.

WILKINS, S. W., GUREYEV, T. E., GAO, D., POGANY, A. & STEVENSON, A. W. (1996). Phase-contrast imaging using polychromatic hard X-rays. *Nature* **384**, 335-338.

YAJIMA, A., INABA, M., TOMINAGA, Y., NISHIZAWA, Y., IKEDA, K. & ITO, A. (2010). Increased osteocyte death and mineralization inside bone after parathyroidectomy in patients with secondary hyperparathyroidism. *Journal of Bone and Mineral Research* **25**, 2374-2381.

YEZZI, ANTHONY, TSAI, A. & WILLSKY, A. (2002). A Fully Global Approach to Image Segmentation via Coupled Curve Evolution Equations. *JOURNAL OF VISUAL COMMUNICATION AND IMAGE REPRESENTATION* **13**, 195--216.

ZHOU, X., NOVOTNY, J. E. & WANG, L. (2009). Anatomic Variations of the Lacunar-Canalicular System Influence Solute Transport in Bone. *Bone* **45**, 704-710.

ZHU, S. C. & YUILLE, A. (1996). Region Competition: Unifying Snakes, Region Growing, and Bayes/MDL for Multi-band Image Segmentation. *IEEE TRANSACTIONS ON PATTERN ANALYSIS AND MACHINE INTELLIGENCE* **18**, 884--900.

Publication list

Manuscripts submitted to peer-reviewed journals

1. Pacureanu, A., Langer, M, Boller, E., Tafforeau, P.& Peyrin, F. Nanoscale imaging of the bone cell network with synchrotron X-ray tomography: optimization of acquisition setup. Submitted to *Medical Physics*, (2011).

2. Pacureanu, A., Langer., M., Olivier, C., Grimal, Q. & Peyrin, F. Quantitative 3D imaging of the human bone lacuno-canalicular network with synchrotron radiation computed tomography. Submitted to *Bone*, (2011).

3. Langer, M., Pacureanu, A., Cloetens, P., Grimal, Q. & Peyrin, F. X-ray phase nanotomography resolves the 3D human bone ultrastructure. Submitted to *PlosOne*, (2011).

Manuscripts to be submitted to peer-reviewed journals

4. Pacureanu, A., Rose, J.L., Revol-Muller, C. & Peyrin, F. A variational region growing approach for segmentation of the 3D bone cell network from nanoscale CT images. Manuscript to be submitted to *Medical Image Analysis*, (2011).

5. Pacureanu, A., Larrue, A., Peter, Z., Buzuloiu, V. & Peyrin, F. Shape-based adaptive filtering for tubular structures in nanoscale synchrotron tomography images. Manuscript to be submitted to *Pattern Recognition Letters*, (2011).

Peer-reviewed conference articles

1. Pacureanu, A., Rollet, J., Revol-Muller, C., Buzuloiu, V., Langer, M. & Peyrin, F. Segmentation of 3D cellular networks from SR-micro-CT images. *Biomedical Imaging: From Nano to Macro, 2011. ISBI'11. IEEE International Symposium on*, pp 1970-1973, *Chicago, April* (2011).

2. Pacureanu, A., Langer, M., Dong P., Revol-Muller, C., Buzuloiu, V. & Peyrin, F. Imagerie microscopique 3D du réseau lacuno-canaliculaire dans l'os humain. *XXIIIe Colloque GRETSI - Traitement du Signal et des Images GRETSI'11*, 4 pages, *Bordeaux, September* (2011).

3 Peyrin, F., Pacureanu, A. & Langer, M. 3D microscopic imaging by synchrotron radiation micro & nano-CT. *IEEE International Conference on Image Processing, ICIP'11*, special session, 4 pages, in press, *Brussels, September* (2011).

4 Zuluaga, M., Pacureanu, A., Dong, P., Orkisz, M. & Peyrin, F. A minimum cost path approach for the segmentation of bone canalicular network from nano-CT. images. *IEEE Medical Imaging Conference, MIC'11*, 2 pages, in press, *Valencia, October* (2011).

5. Pacureanu, A., Revol-Muller, C., Rose, J. L., Sanchez-Ruiz, M., & Peyrin, F. A vesselness-guided variational segmentation of cellular networks from 3D micro-CT. *Biomedical Imaging: From Nano to Macro, 2010. ISBI'10. IEEE International Symposium on*, pp 912-915, *Rotterdam, April* (2010).

6. Pacureanu, A., Larrue, A., Peter, Z. & Peyrin, F. 3D non-linear enhancement of tubular microscopic bone porosities. *Biomedical Imaging: From Nano to Macro, 2009. ISBI'09. IEEE International Symposium on*, pp 602-605, *Boston, June* (2009).

7. Ionescu, B., Pacureanu, A., Lambert, P. & Vertan, C. Highlighting action content in animated movies. *Signals, Circuits and Systems, 2009. ISSCS'09. IEEE International Symposium on*, pp 37-40, *Iasi, July* (2009).

8. Pacureanu, A., Larrue, A., Peter, Z. & Peyrin, F. Filtrage 3D non-linéaire pour la détection de microstructures biologiques à l'échelle nanométrique. *XXIIe Colloque GRETSI - Traitement du Signal et des Images GRETSI'09*, 4 pages, *Dijon, September* (2009).

Invited oral communication

1. Peyrin, F., Pacureanu, A. & Langer, M., Investigation of the bone osteocyte network from synchrotron nano-CT, *Biology and medicine: from fundamental research to diagnosis Workshop SOLEIL, Paris, January* (2012).

2. Peyrin, F., Pacureanu, A. & Langer, M., Quantitative investigation of bone microvascularization and the osteocyte network from 3D synchrotron micro-computed tomography, *Osteocyte Imaging Workshop, Le Studium, Orléans, January* (2011).

3. Pacureanu, A., Langer, M., Zuluaga, M., Dong P., Boller, E., Cloetens, P. & Peyrin, F. Nanoscale three-dimensional imaging of the bone cell network, *Science Days of ESRF, Val Cenis, October* (2011).

4. Peyrin, F., Langer, M., Pacureanu, A. & Larrue, A. 3D X-ray CT imaging of bone at different scales as input to computational biomechanics. *European Conference on Computational Mechanics, Paris, May* (2010).

Peer-reviewed journal article

Ionescu, B., Ott, L., Lambert, P., Coquin, D., Pacureanu, A. & Buzuloiu, V. Tackling action-based video abstraction of animated movies for video browsing. *J. Electron. Imaging* **19**, 14 pages (2010).